

SOLID STATE NMR OF GRAPHITIC MATERIALS

**SOLID STATE NUCLEAR MAGNETIC RESONANCE
SPECTROSCOPY OF CHEMICALLY MODIFIED GRAPHITIC
MATERIALS FOR THE PERFORMANCE ENHANCEMENT OF
HYDROGEN FUEL CELLS**

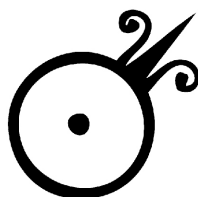
By ADAM ROBERT MACINTOSH, B.Sc., M.Sc.

A Thesis Submitted to the School of Graduate Studies in Partial Fulfilment of
the Requirements for the Degree DOCTOR OF PHILOSOPHY

McMaster University
© Copyright by A.R. MacIntosh, March 2018

McMaster University, Hamilton, Ontario
DOCTOR OF PHILOSOPHY (2018) Chemistry and Chemical Biology

TITLE: Solid State Nuclear Magnetic Resonance Spectroscopy of Chemically Modified Graphitic Materials for the Performance Enhancement of Hydrogen Fuel Cells
AUTHOR: Adam R. MacIntosh, B.Sc., M.Sc., (McMaster University)
SUPERVISOR: Professor Gillian R. Goward
NUMBER OF PAGES: (xxi, 181)



*“Rise up nimbly and go on your strange journey to the ocean of meaning...
Leave and don’t look away from the sun as you go.”*

- Rumi

*Dedicated, as always, to my heroes: who built my heart,
who believed in me, and showed me how to believe in myself.*

Lay Abstract

Solid-state nuclear magnetic resonance (ssNMR) spectroscopy was used to analyse numerous graphene-sheet based materials in an attempt to study their effects on the performance of polymer electrolyte membrane fuel cell (PEM-FC) materials. It has been noted in the literature that fuel cells which incorporated these materials (e.g. functionalized graphene / graphite, doped carbon nanotubes (CNTs), etc.) displayed increased performance over a wider range of environmental conditions, chiefly temperature and relative humidity. The inter-material interactions behind this phenomenon are poorly described at best. Due to its extreme site specificity and sensitivity to minute differences in nuclear electromagnetic environments, ssNMR is an ideal tool for investigating the complicated interactions at work in these systems. While the electronically conductive, amorphous, non-stoichiometric, and low spin-density nature of these materials presented challenges to the collection of NMR spectra, the results presented here display the remarkable utility of this method in the study of analogues and derivatives of graphene.

Covalently functionalized graphene / graphite was synthesized, and the structures of several derivatives were recorded with remarkable resolution, such that functional group carbons were resolvable. The proton dynamics of this material were remarkably slow, and so improvements in composite PEM ion conductivity were proposed to be caused by surface interactions between dopant and polymer. The proton dynamics of ionomer-graphene composites were also investigated through ssNMR. A number of graphene and CNT samples doped with phosphorus and ^{15}N -labelled nitrogen were also analysed, and the synthesis methods employed were found to produce chemically homogeneous dopant sites with few by-products. Absent isotopic labelling, nitrogen dopant sites in carbon black samples were found to affect the relaxation properties of protons within nitrogen doped carbon black.

Abstract

Solid-state nuclear magnetic resonance (ssNMR) spectroscopy was used to analyse numerous graphene-sheet based materials in an attempt to study their effects on the performance of polymer electrolyte membrane fuel cell (PEM-FC) materials. It has been noted in the literature that fuel cells which incorporated these materials (e.g. functionalized graphene, doped carbon nanotubes (CNTs), etc.) displayed increased performance over a wider range of environmental conditions, chiefly temperature and relative humidity. The inter-material interactions behind this phenomenon are poorly described at best. Due to its extreme site specificity and sensitivity to minute differences in nuclear electromagnetic environments, ssNMR is an ideal tool for investigating the complicated interactions at work in these systems. While the electronically conductive, amorphous, non-stoichiometric, and low spin-density nature of these materials presented challenges to the collection of NMR spectra, the results presented here display the remarkable utility of this method in the study of analogues and derivatives of graphene.

Graphene Oxide (GO), a derivative of graphene, has intrinsic proton conductivity which is similar to NafionTM, the most popular proton exchange membrane material currently used in fuel cells. Research into acid-functionalized graphene oxides and determining the role of acidic groups in increasing proton conductivity will help to improve polymer electrolyte membrane performance in fuel cell systems. Multinuclear solid-state NMR (ssNMR) spectroscopy was used to analyse the structure and dynamics of GO and a number of sulfonic acid derivatives of GO, both novel and previously reported. ¹³C spectra showed the disappearance of surface-based oxygen groups upon GO functionalization, and can be used to identify linker group carbon sites in previously synthesized and novel functionalized GO samples with high specificity. Dehydration of these samples allows the collection of ¹H spectra with resolved acidic proton and water peaks. The effect

of dehydration on the proton spectrum is partially reversible through rehydration. Deuteration of the acidic groups in high temperature and acidic conditions was virtually unsuccessful, indicating that only the surface and not the intercalated functional groups play a role in the enhanced proton conductivity of ionomer / functionalized GO composites. Increased surface area and increased delamination of functionalized GO is suggested to be important to improved PEM-FC performance. This synthesis and method of analysis proves the utility of ssNMR in the study of structure and dynamics in industrially relevant amorphous carbon materials, despite the obvious difficulties caused by naturally broad signals and low sensitivity.

Graphene and carbon nanotubes (CNTs) have been investigated closely in recent years due to their apparent positive effect on the electrochemical performance of new fuel cell and battery systems as catalyst stabilizers, supports, or as metal-free catalysts. This is particularly true for doped graphene and CNTs, where only a small amount of doping with nitrogen and/or phosphorus can have a remarkable effect on materials performance. A direct link between structure and function in these materials is, as of yet, unclear. Doped graphene and CNTs were synthesized using varied chemical vapour deposition (CVD)-based methods, and ssNMR was used to unambiguously identify dopant atom sites, revealing that these particular synthesis methods result in highly homogeneous populations of installed phosphorus and nitrogen atoms. We present the first experimental ^{15}N spectrum for graphitic nitrogen in N-doped graphene. ^{15}N -labeled nitrogen doped graphene synthesized as reported here produces mainly graphitic nitrogen sites located on the edges of sheets and around defect sites. ^1H - ^1H and ^1H - ^{15}N correlations were also used to probe dopant nitrogen sites in labelled and unlabelled N-doped graphene. A nearly homogeneous population of phosphorus in P-doped graphene is found, with an overwhelming majority of graphitic phosphorus and a small amount of phosphate oligomer. Similar findings are noted for the phosphorus sites in phosphorus and nitrogen co-doped CNTs with a minor change in chemical shift, as would be expected from two chemically similar phosphorus sites

in carbon allotropes (CNTs versus graphene sheets) with significantly different electronic structures.

Ionomeric sulfonated polyether ether ketone (SPEEK) membranes were doped with functionalized graphenes, and the proton conductivities of these composite membranes was measured at fuel cell operational temperatures and percent relative humidities (%RH). The differences in proton conductivity between pure SPEEK membranes and composites with different dopants and doping levels at varied conditions were investigated through high-field ^1H ssNMR. It was found that high-speed MAS was able to dehydrate membranes under water-saturated conditions, and so lower %RH conditions were better able to produce reliable ssNMR results. The addition of graphitic dopants appeared to have an overall detrimental effect on the bulk proton conductivity of membranes, while concurrently these doped membranes had a broadened operational temperature window.

In an attempt to explore the positive influence of nitrogen doping on the effective lifetime of carbon-supported platinum catalysts used in automotive hydrogen fuel cell systems, solid-state NMR was employed to probe the difference (if any) between doped catalyst supports made from different carbon and nitrogen sources. ^1H spectroscopy showed a variety of sites present in the doped samples; some likely from residual starting material but others from novel sites within the doped catalyst supports. Double-quantum and 2D ^1H experiments were used to examine the structure of these catalysts, while ^{13}C CPMG experiments (see **Chapter 2**) revealed subtle differences in the nuclear relaxation rates of these materials, potentially related to their electronic conductivity. The results of the ssNMR analysis were insufficient to provide an unambiguous picture of the dopant sites within these carbon black samples; this was due in equal parts to the lack of isotopically labelled dopants, the effects of electronic induction and ring current shifts on data acquisition and analysis, and the broad array of different ^{13}C chemical shift environments present in the carbon black itself. While the data is still interesting spectroscopically, suggestions are made at the end of this chapter to expand upon the lessons learned through this study to produce more useful results from similar samples in the future.

Acknowledgements

My first and foremost thanks must go to my supervisor, Dr. Gillian Goward. She is responsible for leading me towards and through some of the most challenging and meaningful days of my life. Her patience and wisdom have been completely indispensable, and (for once) I don't have the words to express my gratitude.

The Goward lab has featured some of the most interesting, intelligent, warm, and understanding people I have ever had the pleasure to call my friends. My heartfelt thanks go out to Dr. Sergey Krachkovskiy, Dr. Leigh Spencer-Noakes, Dr. Nicole De Almeida, Dr. Allen Pauric, Dr. Zoe Reeve, Dr. Danielle Smiley, Matteo Tessaro, Mark Dunham, Gabrielle Foran, David Bazak, Chris Franko, Annica Freytag, and Chelsey Hurst. Special thanks are due to Dr. Kris Harris, who is probably at least half-responsible for any good idea I took full credit for over the past years, and Maria Maqsood, who renewed my faith in the kids these days, and whom I know has nothing but success and happiness ahead of her. I truthfully hope that this is not goodbye for us.

Thanks are also due to my graduate committee; to Dr. Alex Adronov and Dr. Guiseppe Melacini, and also to the incomparable Dr. Alex Bain, who left us at the end of 2016 after a lifetime of ground-breaking achievements in NMR. Without their instruction and helpful conversations I would be a poorer scientist and a less useful person. For their interesting and valuable lecture series, thank you to Dr. Adam Hitchcock and again to Dr. Guiseppe Melacini. Thank you to Dr. Steve Kornic, Dr. Bob Berno, Dr. Hilary Jenkins, Megan Fair, Vicky Jarvis, and Tadek Olech; any success that found its way to me did so by their tireless efforts. Thank you to my TA supervisors Dr. Linda Davis, whose experience and leadership I tried to shoddily pass off as my own in front of the undergrads, and Greg Bahun, whose affable nature and calm collectedness I hope to achieve one day, and whose presence will always be sorely missed.

I also extend my thanks to McMaster University, the provincial government of Ontario, and the CaRPE-FC research network (funded by the Natural Sciences and Engineering Research Council of Canada) for financial support.

For their unwavering confidence and patient love, thank you so much to my parents Tony and Maria, my sister Amanda, my brother Alex, and my closest friends Josh and Neil. I don't know what's going to happen to me next, but I know you'll be there to see it too.

Lastly, but closest to my heart, my thanks go out to my lab-mate and home-mate, my beautiful Blossom. Thank you for taking such good care of me. I know how difficult I can be, but against my constant efforts you make my life warm, loving, and purposeful.

Table of Contents

Introduction	1
Fuel Cells	
Fundamentals	3
Common Classes of Fuel Cells	5
Proton Exchange Membranes (PEMs) and Composites	
Nafion TM	8
Hydrocarbon PEMs	12
PEM Composites	15
Oxides and Polyacids	16
Graphitic Additives	17
Carbon Allotropes	
Carbon Black	20
Graphene & Graphene Oxide	21
Carbon Nanotubes	24
Motivation and Targets	
References	28
Experimental Methods	35
Solid-State Nuclear Magnetic Resonance (ssNMR)	
Signal Origin & The Zeeman Effect	35
Pulses, Relaxation & Signal Acquisition	38
Relevant Nuclear Interactions	40
Magnetic Shielding & Chemical Shift	41
Dipolar Coupling	44

Solids & Magic Angle Spinning	46
Pulse Sequences	
The Bloch Decay & Spin Echo: Standard ssNMR Pulse Sequences .	49
The Carr-Purcell-Meiboom-Gill (CPMG) Sequence: Single-channel Signal Enhancement	50
Cross Polarization	51
2D NMR Experiments	53
Sample-Specific Considerations	
Sample Conductivity	56
Ring Current Shifts	57
Paramagnetic Relaxation	58
Additional Challenges	59
Electrochemical Impedance Spectroscopy (EIS)	
References	63
Structure and Dynamics in Functionalized	
Graphene Oxides through Solid-State NMR	65
Introduction	
Experimental	
Results & Discussion	
Impacts of Functionalization on Sheet Spacing via Powder XRD . .	72
Evidence of Functional Group Structure by ^1H - ^{13}C NMR	74
Thermal Analysis of Functionalized SGO Stability	78
Evaluation of Local Mobility and Exchange by ^1H & ^2H ssNMR . .	80
Conclusions	
References	85
Phosphorus and Nitrogen Centers in Doped	
Graphene and CNTs Analyzed Through	
Solid-State NMR	88

Introduction	
Experimental	
Synthesis: Doped Graphenes (PG, PG-O, NG)	92
Synthesis: Doped Carbon Nanotubes (PNCNTs)	94
Characterization	94
Results & Discussion	
Phosphorus-doped Graphene (PG and PG-O)	95
Phosphorus and Nitrogen-doped Carbon Nanotubes	100
Nitrogen-doped Graphene (NG)	103
Conclusions	
References	110
The Effects of Temperature and Relative Humidity on Proton Conductivity in Composite SPEEK - Functionalized Graphite Polymer Electrolyte Membranes	113
Introduction	
Experimental	
Membrane & Dopant Synthesis	117
Membrane Casting & Treatment	118
Characterization	119
Results & Discussion	
SPEEK Degree of Sulfonation	120
Low Temperature, High %RH Conditions	122
EIS at Operational Conditions	123
¹ H ssNMR at Operational Conditions	124
High Temperature, Low %RH Conditions	129
EIS at Operational Conditions	130
¹ H ssNMR at Operational Conditions	132
Low MAS rate ¹ H ssNMR	137

WU%	139
Conclusion	
References	142
Natural Abundance NMR Spectroscopy of	
Nitrogen-Doped Carbon Black	144
Introduction	
Experimental	
Nitrogen Doping of Carbon Black Samples	149
Analysis	150
Results & Discussion	
¹ H ssNMR Analysis	152
¹³ C ssNMR Analysis	159
Conclusions	
Suggestions for Future Work	
Isotopic Labelling	164
Variable Temperature Studies	165
Alternative Nuclei, Experiments, Targets	165
Appendix	
References	168
Conclusion	171
Summary	
Outlook & Future Work	
A Library of Functionalized Graphenes	177
ssNMR and 2D Materials	178
Proton Dynamics in Ionomer Membranes	179
References	181

List of Figures

1.1 - A schematic drawing of a PEM-FC	3
1.2 - Three phases in the MEA	7
1.3 - Grotthuss vs. vehicular proton transport	8
1.4 - Structure of Nafion TM	10
1.5 - Structure of SPEEK and sample NMR spectrum	13
1.6 - Previous composite PEM results	19
1.7 - Graphene oxide structure and NMR spectroscopy	23
2.1 - The Zeeman effect and bulk magnetization vector	37
2.2 - An illustration of the chemical shift interaction	43
2.3 - An illustration of the dipolar interaction and effects of magic angle spinning	47
2.4 - Relevant pulse sequences	51
2.5 - Impedance spectroscopy sample Nyquist plot	61
3.1 - Sulfonated graphene structures and powder XRD	69
3.2 - ¹ H- ¹³ C CPMAS spectra of GO and SGOs	76
3.3 - GO functionalization diagram	78
3.4 - TGA of GO and SGOs	79
3.5 - ¹ H and ² H spectra of propyl SGO	81
3.6 - ¹ H VT spectra of GO and propyl SGO	83
4.1 - SEM of PG and PG-O	96
4.2 - P 2p-edge XPS spectra of PG and PG-O	97
4.3 - ³¹ P NMR spectroscopy of PG and PG-O	98

4.4 - SEM and TEM of PNCNTs	100
4.5 - N 1s, P 2p edge XPS of PNCNTs	101
4.6 - ^{31}P and ^1H NMR spectra of PNCNTs	102
4.7 - ^{31}P NMR comparison of PG-O and PNCNTs	103
4.8 - SEM of NG	104
4.9 - N 1s-edge XPS spectra of NG	105
4.10 - ^{15}N and ^1H NMR spectra of NG	106
4.11 - ^1H - ^{15}N 2D NMR spectra of NG	107
4.12 - Nitrogen centers in NG	108
5.1 - SPEEK solution NMR and degree of sulfonation	122
5.2 - SPEEK and composite proton conductivity vs. temperature	124
5.3 - ^1H NMR spectra of SPEEK	125
5.4 - VT ^1H NMR spectra of SPEEK composites	126
5.5 - VT ^1H NMR spectra and line widths of SPEEK and composites	129
5.6 - SPEEK and composite proton conductivities	131
5.7 - VT ^1H NMR spectra of SPEEK and composites	133
5.8 - VT ^1H NMR hysteresis	136
5.9 - Low MAS rate ^1H NMR spectra of SPEEK and composites	138
5.10 - SPEEK and composite water uptake	139
6.1 - TGA of carbon black and N-doped samples	151
6.2 - ^1H NMR spectra of carbon black	153
6.3 - ^1H NMR spectra of N-doped samples	154
6.4 - ^1H BaBa and EXSY NMR spectra of carbon black and N-doped samples	157
6.5 - Potential N-dopant sites	158
6.6 - ^{13}C CPMG spectra of carbon black and N-doped samples	160
A6.1 - BaBa peak intensities	167
A6.2 - CPMG pulse timings and relevant measurables	167
A6.3 - Carbon black and N-doped sample T_2 fits	168

List of Tables

1.1 - Fuel cell types	6
3.1 - Sulfonated graphene elemental analysis	72
4.1 - Doped graphene/ CNT elemental analyses via XPS	95
6.1 - Carbon black, doped sample T _{2s}	161

Symbols and Abbreviations

%RH	Percent relative humidity
(SW, MW)CNTs	single-walled, multi-walled carbon nanotubes
APS	Ammonium peroxydisulfate
B ₀	Permanent magnetic field
B ₁	Applied magnetic field
BaBa	Back-to-back, an NMR pulse sequence
BPC	Black pearl carbon
CB	Carbon black
CCM	Catalyst coated membrane
EA	Elemental analysis
CO	Carbon monoxide
CP	Cross polarization
CPMG	Carr, Purcell, Meiboom, Gill
CSA	Chemical shift anisotropy
CVD	Chemical vapour deposition
D-carbon	Denka carbon
DDI	Distilled, deionised
ΔE	Difference in energy
ΔH	Change in enthalpy
δ	Chemical shift
DMAc	Dimethyl acetamide
DMF	Dimethyl formamide
DMSO	Dimethyl sulfoxide
DNP	Dynamic nuclear polarization

DoS	Degree of sulfonation
EDX	Energy dispersive X-ray
EIS	Electrochemical impedance spectroscopy
EMIM-DCA	Ethyl methyl imidazolium dicyanamide
EPR	Electron paramagnetic resonance
eq/g	Equivalentents per gram
η	Skew
EW	Equivalent weight
EXSY	Exchange spectroscopy
FGO	Functionalized graphene oxide
FID	Free induction decay
γ	Gyromagnetic ratio
GDL	Gas diffusion layer
h	Planck's constant
H_D	Dipolar coupling Hamiltonian
HMQC	Heteronuclear multiple quantum coherence
HOR	Hydrogen oxidation reaction
I	Current
I	Nuclear spin
IEC	Ion exchange capacity
IL	Ionic liquid
IPA	Isopropyl alcohol
λ	Wetness
M	Magnetization vector
MAS	Magic angle spinning
MEA	Membrane electrode assembly
MOF	Metal-organic framework
μ_0	Permeability of free space
NG	Nitrogen doped graphene

ν	Frequency
ν_R	Rotor frequency
Ω	Span
ω_L	Larmor frequency
ORR	Oxygen reduction reaction
OSAB	Oxidized small acetylene black
PEEK	Polyether ether ketone
PEM-FC	Polymer electrolyte membrane fuel cell
PFSA	Perfluorosulfonic acid
PG	Phosphorus doped graphene
PGO	Propylsulfonic graphene oxide
PNCNT	Phosphorus & nitrogen doped carbon nanotube
PPh ₃	Triphenyl phosphine
PSS	Polystyrene sulfonate
PTFE	Polytetrafluoroethylene
p-XRD	powder X-ray diffraction
r, θ	Internuclear distance, azimuth
RF	Radiofrequency
SEM	Scanning electron microscopy
SGO	Sulfonated graphene oxide
σ	Ionic conductivity
σ	Chemical shielding
SNR	Signal to noise ratio
SPEEK	Sulfonated polyether ether ketone
sPPP	Sulfonated polyphenyl phenylene
ssNMR	Solid-state nuclear magnetic resonance
T ₁	Spin-lattice relaxation
T _{1ρ}	Spin-lock relaxation
T ₂	Spin-spin relaxation
T ₂ [*]	Effective spin-spin relaxation

τ	Pulse timing block
TEM	Transmission electron microscopy
TGA	Thermogravimetric analysis
TMS	Trimethyl silane
TPP	Triphenyl phosphine
V	Voltage
VT	Variable temperature
WU	Water uptake
Z	Impedance

Declaration of Academic Achievement

Dr. Kristopher J. Harris, a research associate in the Goward group, was responsible for some of the initial experimental setup and data interpretation regarding the analyses of graphene oxide and its functionalized analogues. Adam Riese, Zhongxin Song (from the Sun group at Western University), Pouyan Zamani, and Gaopeng Jiang (from the Chen group at the University of Waterloo) were responsible for the synthesis of doped graphene and carbon nanotube samples. Dr. Darija Susac and Tyler Trefz, researchers at AFCC, were responsible for the synthesis and XPS characterization of N-doped carbon black samples. Maria Maqsood, an undergraduate research associate in the Goward group, was responsible for synthesis and casting of SPEEK composite membranes. All other synthesis, data acquisition, and interpretation were performed by A.R. MacIntosh.

1 — Introduction

Over the next several decades, the most pressing challenge to the continuation of familiar society will be resource management: specifically the management of energy, and more specifically, the implementation of clean, renewable, and plentiful energy systems across the globe. Energy systems involve the harvesting, storage, and usage of energy. These concepts affect every stage of production and commerce, and are involved in basically every modern human action in some way. The current most popular energy system is based on fossil fuels, which are dragged from deep beneath the ground and processed at enormous (sometimes disastrous) material and environmental cost. Storage is where fossil fuels shine: coal, gasoline, and natural gas have very high energy density (unit energy per unit mass) and are costly but trivial to transport and handle. The usage of fossil fuels, especially for transportation and electrical power, is extremely problematic. The negative climatological effects of anthropogenic greenhouse gasses, particularly CO₂, have been very well documented.¹⁻⁵ There are a number of researchers who deduce that the environment is very close to a breaking point, and with an increase of a few more degrees in the annual average temperature the world's ecosystem would be beyond repair within a few decades.⁶⁻¹⁰ A changing climate of this kind is expected

to have enormous negative effects on civilization with respect to economics and global stability and conflict in addition to ecological preservation^{6, 11, 12}

In order to avoid this, a shift away from the fossil fuel energy system towards a renewable, economically competitive, environmentally neutral system is necessary. Significant progress has been made in harvesting energy from renewable wind, tidal, and solar sources.¹³⁻¹⁹ Automobiles, aircraft, and other transport systems are being designed with energy efficiency increasingly in mind.²⁰⁻²² Concurrently, new methods of energy storage and usage have been developed. One of the most popular and promising of these technologies is the fuel cell. As global energy usage climbs to worrying heights year-by-year, alongside record high temperatures, glacier recession and severe weather incidents, fuel cell and other green technologies become increasingly vital.

1.1 Fuel Cells

Though they enjoy a current renaissance of popularity, the concept of fuel cells, which produce electrical current by expending a fuel source as a reagent in an electrochemical reaction, has been well described for over 150 years, placing them among the oldest electrochemical devices invented.²³ Until the environmental damage caused by the burning of fossil fuels became apparent, however, fuel cell technology was passed over in favour of cheap and plentiful oil. The following section details the fundamentals behind fuel cells, paying special attention to the polymeric and organic additive materials which make up the devices themselves.

1.1.1 Fundamentals

Like the Galvanic cell, a fuel cell is a device which isolates the two halves of a thermodynamically spontaneous reduction-oxidation (redox) reaction, the main difference being that the reactants in a fuel cell reaction are freely moving and replenished during usage from outside the cell. The most successful and highly optimized fuel cells employ the reduction of hydrogen to water in the presence of oxygen, as seen in **Figure 1.1** in a schematic of a polymer electrolyte membrane fuel cell (PEM-FC). The reaction produces 1.23 V of electromotive force per mole of electrons, is driven enthalpically ($\Delta H = -286 \text{ kJ/mol}$), and is generally catalyzed on platinum.²⁴⁻²⁶

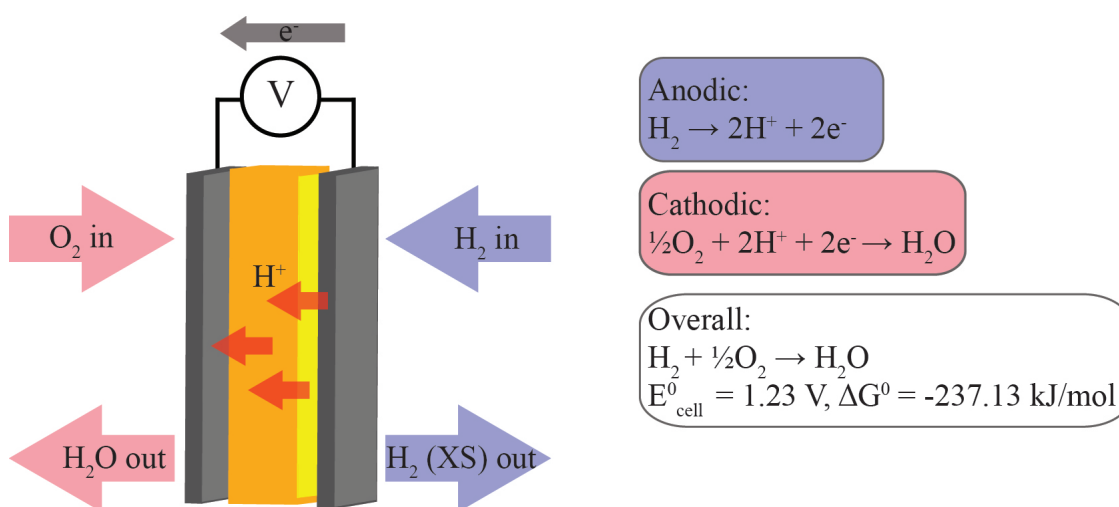


Figure 1.1: A schematic drawing of a PEM-FC. Hydrogen gas is fed through a gas diffusion layer to the catalyst film (yellow), where protons are generated and travel through the PEM (orange) to the cathode layer where they combine with atmospheric oxygen to produce water.²⁶

When a fuel cell is producing current, hydrogen gas is fed through a gas diffusion layer (GDL) to the catalyst coated membrane (CCM): a layer consisting of catalytic platinum on current collecting carbon black mixed with an ionomeric binder.

This layer is effectively the cathode of the cell. As the hydrogen gas molecules are reduced into pairs of protons, the electrons pass through metallic current collectors and travel through the external circuit to do useful work. The protons are driven toward the anodic layer of the fuel cell through an ionomeric membrane layer which acts as the electrolyte of the cell and isolates the two half-reactions. The ionic conductivity, σ , across this membrane is one of many important cell parameters. In the anode layer (which is structurally similar to the cathode but usually ca. 3 times thicker to accommodate for differing rates of reaction) the protons are oxidized by oxygen gas from the air. Locally, the only by-product is water, and if the hydrogen fuel is obtained from environmentally friendly sources, e.g. a solar-powered hydrolyzer (essentially a fuel cell run in reverse) the entire energy system can be nearly carbon neutral. Fuel cells enjoy a comparatively high power-mass ratio, making them ideal for applications where total product mass is an engineering concern i.e. for trucks, buses, aircraft, spacecraft, etc.^{21, 22, 27}

There are three interconnected principle issues with fuel cell designs as they exist today. The first is that the devices rely too heavily on catalytic platinum to perform adequately. Platinum is expensive and rare, and so steps are constantly being taken to extend the lifetime of the CCM or to find new non-precious catalysts.²⁸⁻³⁰ The second is that many of the most common electrolyte materials only perform at their optimal proton conductivities under high atmospheric relative humidity and over a narrow temperature range, typically between 60 and 90 °C. These conditions would only be an interesting challenge for automotive engineers, however they are also highly conducive to platinum catalyst poisoning by carbon

monoxide (CO).³¹⁻³³ CO is introduced to the system in part due to the third issue: the vast majority of H₂(g) fuel is produced as a by-product of the steam cracking of natural gas into syngas, a mixture of mainly hydrogen and carbon monoxide gasses.³⁴ Purification of H₂(g) to acceptably low levels of CO drives up the costs of fuel, and the use of gas cracking as a fuel source defeats the fuel cell's purpose as a 'green' replacement for the fossil fuel-driven energy systems in place today. An ideal fuel cell would have a chemically resistant, inexpensive electrolyte layer whose proton conductivity was acceptable at low humidity and high temperature, with a long-lived non-precious metal catalyst being fuelled by H₂(g) from a renewable, environmentally sound source.

1.1.2 Common Classes of Fuel Cells

The PEM fuel cell is certainly not the only form of this device. Generally, these alternatives are named after either their fuel source or the electrolyte employed in the redox chemistry that drives the produced voltage. Certain fuel cell types, particularly the solid oxide and molten carbonate family of cells, operate at extremely high temperature (800 - 1000 °C) and so are limited in their applications. Others, like the direct methanol fuel cell, use a hydrocarbon fuel and produce CO₂ and other greenhouse gasses.

Fuel storage is not an in-built feature of any of these cell models, and so each has its own challenges specific to the fuel type (e.g. pressurized H₂ tank or charged zeolite / MOF, methanol tank, etc.). **Table 1.1** contains relevant information for some of the more popular alternatives to PEM-FCs.³⁵ Considering their robust

Table 1.1: Fuel cell types.³⁵

Cell Type	Fuel	Ionic Species	Anodic	Cathodic	Usage
Polymer Electrolyte	H ₂ gas	H ⁺	H ₂ → 2H ⁺ + 2e ⁻	1/2 O ₂ + 2H ⁺ + 2e ⁻ → H ₂ O	Broad usage in transport and stationary power
Molten Carbonate	H ₂ gas	CO ₃ ²⁻	H ₂ + CO ₃ ²⁻ → H ₂ O + CO ₂ + 2e ⁻	1/2 O ₂ + CO ₂ + 2e ⁻ → CO ₃ ²⁻	High temperature power
Solid Oxide	H ₂ gas, H ₂ O	O ²⁻	H ₂ + O ²⁻ → H ₂ O + 2e ⁻	1/2 O ₂ + 2e ⁻ → O ²⁻	High temperature power
Direct Methanol	MeOH	H ⁺	CH ₃ OH + H ₂ O → CO ₂ + 6H ⁺ + 6e ⁻	3/2 O ₂ + 6H ⁺ + 6e ⁻ → 3H ₂ O	Small-scale energy storage
Phosphoric Acid	H ₂ gas	H ⁺	H ₂ → 2H ⁺ + 2e ⁻	1/2 O ₂ + 2H ⁺ + 2e ⁻ → H ₂ O	Stationary heat & power

working range, light weight and relative ubiquity, the rest of this work will focus exclusively on PEM-FCs.

1.2 Proton Exchange Membranes (PEMs) and Composites

The PEM layer serves two purposes in the fuel cell: to shuttle ions from anode to cathode and to isolate these electrode layers to prevent a short circuit. This layer is the center of the membrane-electrode assembly (MEA), sandwiched between the CCMs (illustrated in **Figure 1.2**) and GDLs. An analogy to sandwiches is not entirely accurate, however: the outside layers of the PEMs are coated with a slurry containing carbon-supported precious metal catalysts, conductive carbon black and an ionomer support, usually the same material being used in the PEM. This allows for a smooth transport of ions to and from the CCMs and PEM.³⁶ One

MEA is the singular unit of a fuel cell stack, which may connect tens of MEAs to produce a fuel cell outputting a certain desired power.³¹ Typically the PEM has a thickness in the tens of microns, and mass transport efficiency and charge transfer kinetics this membrane are major contributors to power output. As a result, the ideal PEM (in addition to being easy to make, inexpensive, and chemically and thermally resistant) has high proton conductivity. PEM materials are chosen and optimized based on these parameters, and many additives have been investigated based on their ability to raise σ or increase the temperature or humidity range where σ can produce a useful current.

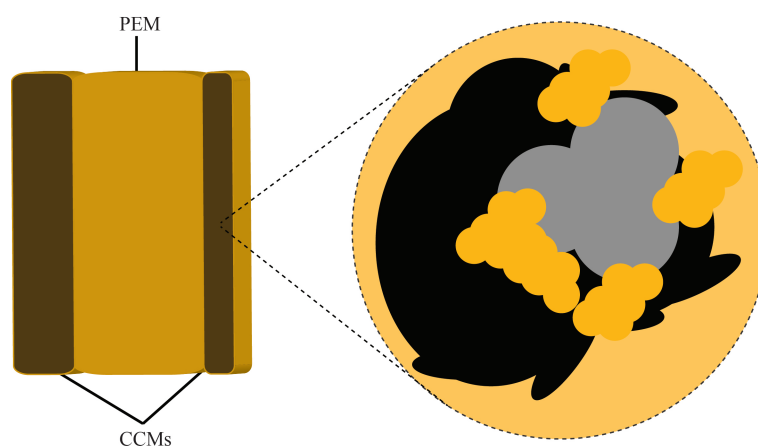


Figure 1.2: A close-up of the three-phase system within the fuel cell MEA. Pt nanoparticles (grey), carbon support (black) and ionomer (yellow).

Protons are conducted through the PEM via either a vehicular or a so-called Grotthus mechanism, illustrated in **Figure 1.3**.^{37–39} In the vehicular mechanism, an acidic proton attached to the polymer backbone donates its proton to a nearby water molecule, which then diffuses over some distance and acidifies a second deprotonated acid site and so on. The Grotthus mechanism is similar, but the acid sites directly protonate and deprotonate each other (or one acid site protonates

an essentially stationary water molecule, which then protonates a nearby deprotonated acid site) without the need for diffusion. Many PEM materials have been found to cast into discrete hydrophilic micro-channels, where acidic sites congregate together similar to a phospholipid micelle, walled by the hydrophobic polymer backbone. Even in the Grotthuss mechanism, water is necessary to keep these channels expanded and allow acidic sites the mobility to exchange protons.

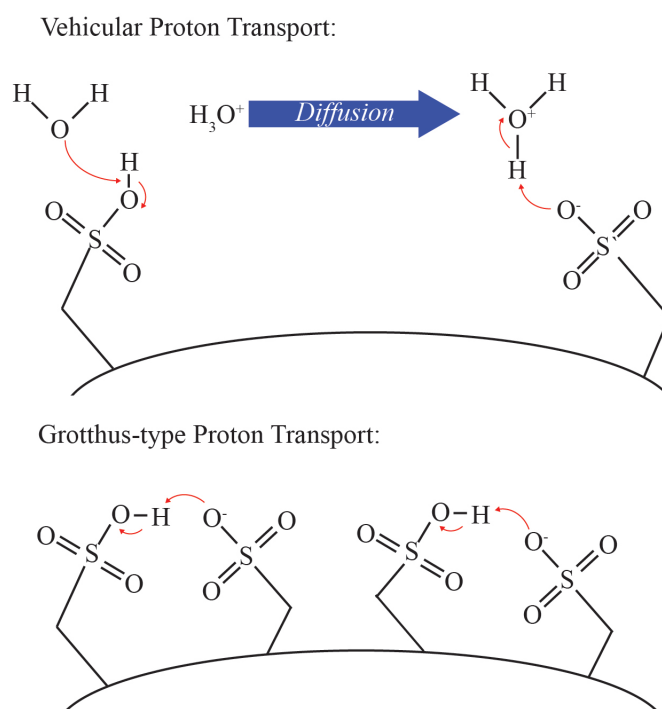


Figure 1.3: An illustrated comparison of the Grotthuss and vehicular mechanisms of proton transport in PEMs. In the Grotthuss mechanism, an intermediate, stationary water molecule which does not diffuse may be involved.

1.2.1 NafionTM

Figure 1.4 shows the monomeric structure and an illustrated membrane of NafionTM, a proprietary, nearly perfluorinated ionomer.⁴⁰ It is a co-polymer of

polytetrafluoroethylene (PTFE) and a similar monomer unit containing a pendant chain terminated with a sulfonic acid group. Its proton conductivity is thought to be the result of a micro-phase separation of the backbone and pendant groups, forming long hydrophilic channels, only a few nanometers in diameter, throughout the membrane. Under optimal conditions a NafionTM membrane has a proton conductivity on the order of 10^{-1} to 10^0 S/cm, which currently stands as the industry benchmark. The equivalent weight (EW) of NafionTM, a useful metric defined as the number of acidic sites per unit mass of polymer, in equivalents per gram (eq/g), can be varied depending on the monomer ratio. This value has a marked effect on wettability, λ , the number of water molecules per acidic group, at a given set of environmental conditions, which is strongly correlated with proton conductivity and cell performance. The proton attached to the sulfonate group has a pKa of ca. -6, thanks largely to the electron-withdrawing fluorine groups on the pendant chain, further facilitating protonation / deprotonation. NafionTM has been studied extensively since its introduction in the 1960s. In addition to its high proton conductivity, NafionTM is chemically resistant to the redox-active environment of a fuel cell, and shows thermal resistance well above any PEM-FC maximum operational temperature.^{33, 41, 42} NafionTM membranes are cast from solutions in a number of different solvents, having a marked effect on membrane proton conductivity. Ramya et al., for example, showed that choosing a casting solvent with a solubility parameter close to that of the PTFE backbone in NafionTM reduced charge transfer resistance in the membrane, while a solvent with a solubility parameter closest to the acidic side chains had greater ionic conductivity.^{43, 44}

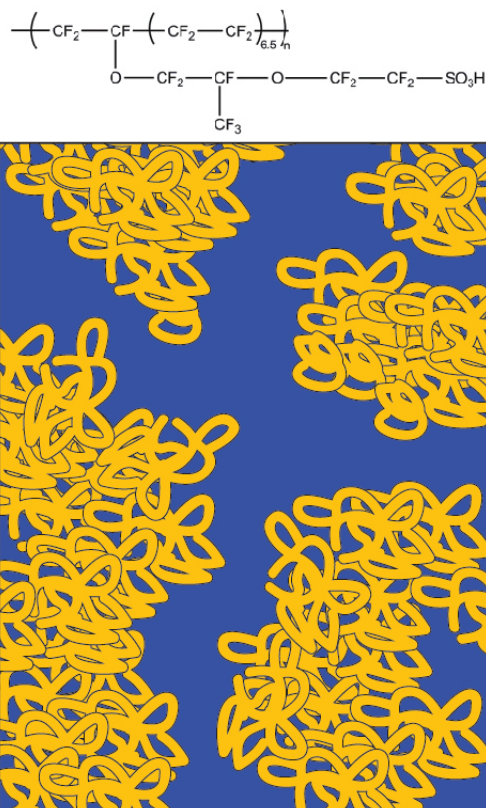


Figure 1.4: The monomeric formula for NafionTM, and an illustration of its macroscopic structure. Bundles of ionomer (yellow) aggregate with their hydrophobic backbones oriented inward, forming hydrophilic channels.

NafionTM is an excellent PEM material, but the needs of most fuel cell applications have proven that there is progress to be made. The material only displays its high proton conductivity over a narrow range of environmental conditions: an atmosphere with 100% relative humidity and at a temperature of ca. 80 °C. Engineering engine blocks and power supply enclosures becomes even less trivial when these needs are considered and, as mentioned above, these conditions are also conducive to a reduction in the efficiency of the precious metal catalyst particles from carbon monoxide poisoning. NafionTM is thermally stable up to nearly 200 °C, however at higher temperatures the membrane dries out and loses nearly all

of its electrolytic activity.⁴⁵⁻⁴⁷ The ether bond on the NafionTM pendant chain is susceptible to peroxide attack: a careful solid-state NMR-based study of fuel cell run-off gas showed pendant chain fragments severed from the backbone by peroxide side-products of the oxygen reduction reaction in the anode layer.⁴⁸ These deficiencies in operational range and chemical stability together with the steep manufacturing costs of NafionTM, highlight the need for cost-effective and resistant alternative PEM materials. Post-processing of NafionTM has been found to affect performance of membranes as well. Film thickness is a parameter set during the casting process, and can have a significant effect on proton conductivity. In solution, NafionTM is believed to form rod-like agglomerates with the acidic pendant chains pointed outward. As these rods settle during casting, they form the walls of the proton-conducting hydrophilic channels. An ultrathin film (e.g. μm to nm) would be ideal for the fuel cell so as to reduce the contribution of mass transport limitations to produced currents, however the proton transfer processes appear to be different in thin films (ca. 100 nm) than in a normal membrane.⁴⁹ Their proton conductivity can be an order of magnitude lower than the bulk material, and this is thought to be due to incomplete channel formation. The reduced observed proton conductivity likely comes from ion hopping from one hydrophilic pore to the next; a significantly less effective transport mechanism.⁵⁰ Extrusion or annealing of the membranes during the casting process improves proton conductivity as well, due to a reduction in microchannel tortuosity.^{51, 52}

Other perfluorinated ionomers have been studied in order to compare and contrast their performance or cost with that of NafionTM. In most cases, these materi-

als are analogous to NafionTM, modified either by changing the length or branching of the pendant chain or the relative amounts of monomer types.⁵³⁻⁵⁵ Considering their molecular similarity, it is not surprising that these share the same high acidity and roughly the same morphology in solution or as cast membranes. While mild performance increases under particular conditions have been noted, all of the same issues of pendant chain degradation and the high cost of processing persist. A concerted effort has been in place to find a replacement for NafionTM which matches its performance while reducing or removing these concerns.

1.2.2 Hydrocarbon PEMs

Another family of NafionTM competitors come in the form of hydrocarbon-based ionomers. Moving away from perfluorination subverts the problem of high temperature dehydration, and in many cases reduces production costs as well; however the chemical stability of the membrane must still be adequate for long-term fuel cell performance. To meet this necessity, most hydrocarbon PEMs feature repeating aromatic units (e.g. sulfonated polysulfones, polyether ketones, polyimides, etc.) to impart chemical resistance. In ideal cases, new hydrocarbon PEM materials will take this concept a step further and increase resistance to radical attack, for example by moving away from vulnerable ether linkages where possible.

Hydrocarbon ionomers were the first to be used commercially: electronic components on NASA spacecraft generally used fuel cells equipped with polystyrene sulfonate (PSS) exchange membranes.^{56, 57} Perfluorinated sulfonic acid (PFSA) membranes, like NafionTM were developed in response to the damage these mem-

branes incurred due to peroxide radical attack. After a surge in PFSA popularity (and price), hydrocarbon membranes were re-explored as an inexpensive and accessible alternative to perfluorinated ionomers. Many early hydrocarbon ionomers were actually co-polymers of a chemically inert and stable backbone monomer (e.g. styrene, methylmethacrylate etc.) along with an ion-exchanging acidic monomer (methacrylic acid, alkylsulfonic acid).⁵⁸ Small-angle X-ray scattering and water sorption studies showed that, at specific temperatures and with sufficient hydration, a two- or many-phase system forms in these polymers which changes them from insulators to ion conductors. Under these particular conditions, hydrophilic microchannels were believed to be formed by the aggregation of ionic pendant groups, similar to the channel formation seen in PFSA.

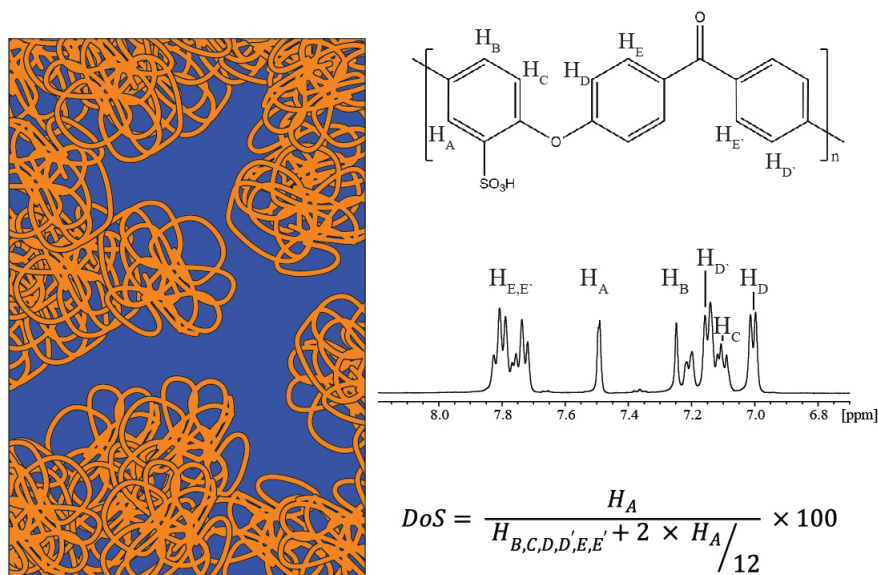


Figure 1.5: The monomeric formula for SPEEK, and an illustration of its macroscopic structure, displaying narrower, more tortuous hydrophilic channels than NafionTM. In addition, a sample solution-state ¹H NMR spectrum and formula for the determination of degree of sulfonation.

Sulfonated polyether ether ketone (SPEEK), seen in **Figure 1.5** is a particularly popular hydrocarbon ionomer among the research community. The parent material, polyether ether ketone (PEEK) is inexpensive, easy to process and extremely resistant, showing very low solubility in anything except strong acids. Dissolution in concentrated sulfuric acid and precipitation in cold water produces SPEEK, and the degree of sulfonation (DoS) can approach 100%.⁵⁹⁻⁶¹ Increasing DoS has been shown to have a positive effect on water uptake properties, which is proportional to proton conductivity, however the conductivity of SPEEK has a stronger dependence on relative humidity than NafionTM. The choice of casting solvent also affects the electrochemical performance of a SPEEK membrane, for example it has been shown that membranes cast from a solution of dimethylformamide (DMF) tend to have poorer conductivities than those cast from dimethylacetamide (DMAc) or dimethyl sulfoxide (DMSO) at a wide range of testing conditions.^{62, 63} This is believed to be due to hydrogen bonding interactions between residual solvent molecules and polymer acid sites, leading to changes in microchannel morphology as well as acid strength. Swelling can be a dramatic issue with SPEEK membranes; depending on the DoS the volume of a membrane can increase by nearly 90%.⁶⁴ High DoS SPEEK membranes not only swell more severely, but at high relative humidities they may take on enough water to essentially self-dissolve. Pure SPEEK membranes, therefore, tend to be used under somewhat narrow conditions, i.e. between 40 - 80 % DoS, at moderate to high humidities (50 - 100 % RH, depending on DoS) and high temperature. Lower

DoS SPEEK can be used at a wider range of conditions at the cost of proton conductivity.

More recently, a new ionomer membrane class based on sulfonated phenyl-polyphenylene (sPPP) has shown promise, significantly overtaking NafionTM in terms of proton conductivity while matching or improving upon its physical and chemical resistance.⁶⁵⁻⁶⁷ These ionomers are polymerized as sulfonated monomers, and so the positioning of acidic sites on their many phenyl rings can be tightly controlled and optimized. They possess no ether linkages, and so are highly resistant to radical attack. One study showed that a sPPP membrane suffered no significant mass loss after treatment with Fenton's reagent, a mixture of hydrogen peroxide and Fe²⁺. This test exposes a membrane to radical attack at an accelerated rate compared to normal PEM usage, and simulates the degradation from peroxides a membrane experiences over long-term usage. While sPPP-based materials show potential, their synthesis is non-trivial compared to other ionomers, and significant progress must be made on this front before any competition with the industry standards is to be had.

1.2.3 PEM Composites

The use of composite membranes containing a PFSA or hydrocarbon ionomer support and relatively small amounts of various dopants has been explored extensively, and significant progress has been made in recent years. There are various dopant types, e.g. salts, oxides, acidic organics and many more, and they have proven to improve the performance of PEMs in unique ways. Multiple informative

reviews have detailed the impressive progress in the field of ionomer membrane composites.⁶⁸⁻⁷¹ It is observed, for instance, that composite membranes can have better water uptake and retention properties, especially at temperatures above 100 °C.⁷²⁻⁷⁴ This feature is especially attractive since it improves the reaction kinetics for hydrogen oxidation / oxygen reduction, and therefore the overall proton conductivity, under conditions where a pure ionomer would dehydrate and become an insulator. Higher temperature operation is a goal for the PEM-FC industry not only because of favourable reaction rates, but because the CO poisoning of costly platinum catalysts is less rapid as well. Why exactly these dopants can cause such dramatic changes in membrane performance, even at doping levels as low as 0.1 %wt, is not completely understood. Dopant introduction may help to disrupt any long-range order in the ionomer matrix (crystallinity, for lack of a better term), which makes for a more cross-linked network of proton conductive channels, allowing for easier movement of water through the membrane. Certain dopants may bring acidic sites of their own, increasing the overall acidity of the membrane and facilitating proton transfer over longer distances. Relevant examples of certain dopant types are given in the following sections.

1.2.3.1 Oxides and Polyacids

The addition of oxides of silicon, zirconium, and many others has been explored as a method to relax the stringent requirements of pure ionomer membranes for adequate proton conductivity. The precise mechanism behind this reliable observation is still under investigation, but optimization studies have shown that oxide

particle amount and size both have a strong effect on conductivity enhancement. Mechanical mixing of ionomer and dopant materials will result in a composite membrane, but control over the homogeneity and particle size is poor, and so a more predictable technique is to form the dopant particles *in-situ* either during or after the casting process. As an example from the Author's research group, Ye et al. used this technique to synthesize composite NafionTM / silica membranes.⁴⁷ They infused tetraethyl orthosilicate into ionomer membranes and forced the polymerization of silica within the hydrophilic channels of NafionTM through heating, thereby controlling particle size. They found that incomplete hydrolysis of alkyl groups from the silicon source was caused by higher concentrations or infusion times, and these residual organic chains stalled mobile protons and reduced conductivity. At lower concentrations or with smaller particle sizes, residual hydroxide groups on the silica particles strengthened the hydrogen-bonded network of NafionTM acidic groups and residual water, leading to better water retention and higher proton conductivities at high temperatures and low relative humidity. In contrast, this interaction between dopant particles and ionomer acid sites has at other times been found to have a negative effect on conductivity in other materials (zirconia, titania, SPEEK, etc.) where the surface area of the particles (and therefore the number of surface hydroxide groups) is large.

1.2.3.2 Graphitic Additives

Graphene and its functionalized analogues, particularly graphene oxide (GO), have been used with success as performance-enhancing ionomer additives. These

materials will be described more thoroughly in a later section. Fowler et al. studied the incorporation of GO and GO functionalized with sulfonic acid groups (SGO).⁷⁵ They tested the proton conductivity of raw graphitic powders as well as composites of GO / SGO and NafionTM, the current benchmark proton conducting membrane material, as a function of temperature and relative humidity. The GO composites showed significantly greater proton conductivity than the bare Nafion at low relative humidity and high temperature, where Nafion is known to perform poorly. SGO composites were able to outperform bare GO composites in terms of proton conductivity, indicating the added acid sites were participating in proton conductivity. They demonstrated an increase in water uptake and ion exchange capacity for the functionalized composite membranes as well. A similar effect was noted by Hwang et al. while investigating GO composition into sulfonated polyimide / polystyrene sulfonate membranes.⁷⁶ They were able to optimize the weight percent of GO composition in order to maximize proton conductivity, doubling that of NafionTM at similar, non-optimum humidity and temperature. A summary of their relevant results is shown in **Figure 1.6**. Other groups have recently studied GO incorporation into other membrane materials, and to looking at the effect of the physical properties of GO (sheet size, stacking, etc.) on proton conductivity.⁷⁷⁻⁷⁹

1.3 Carbon Allotropes

Carbon accounts for only a fraction of a percent of the elemental make-up of the planet, and yet it is one of the most ubiquitous elements in modern application, and perhaps the most versatile. Of the thousands of different carbon-rich materials,

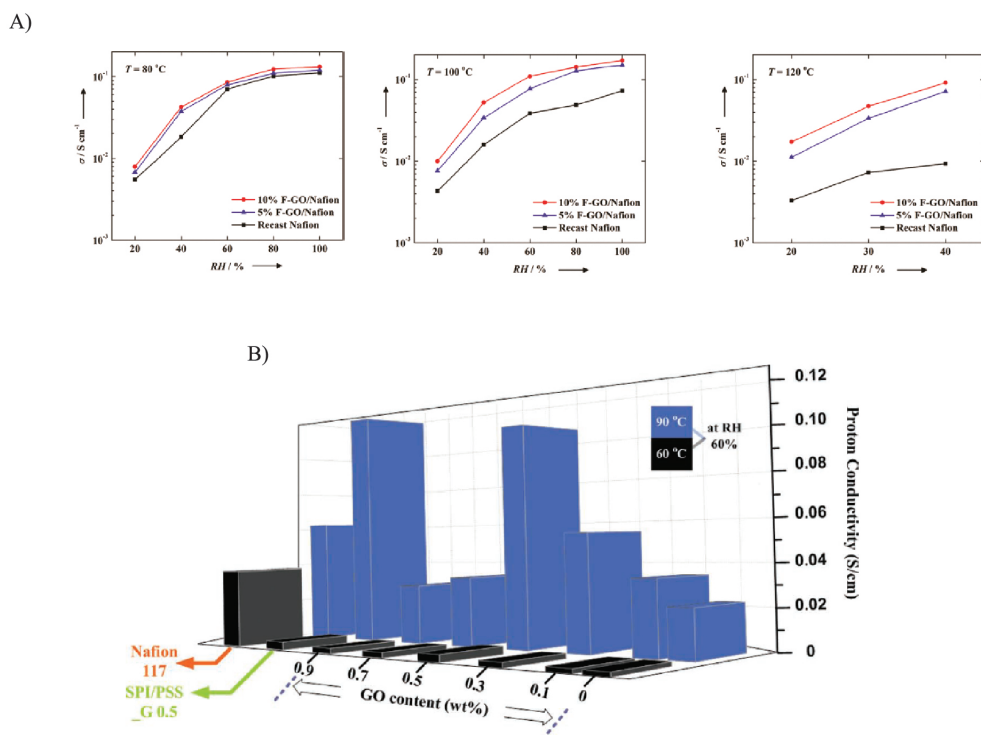


Figure 1.6: A summary of the contributions of A)Fowler et al. and B)Hwang et al. regarding composite PEM materials and their performance at varied environmental conditions. Compiled from figures in references 75 and 76, subject to copyright restrictions.

this section focusses on some of the most geometrically simple. These materials are used as catalyst supports, current collectors and performance-enhancing dopants. This study focusses on carbons as additives for improving the performance of ionic transport layers in PEM-FCs, as well as carbon-based catalysts for the FC electrode layers. One common feature for the specific carbon allotropes studied in this work is that they contain, at least in part, conjugated sp^2 -hybridized carbon atoms, and therefore have electronically conductive networks of π electrons. In addition to the physical properties sought, this electrical conductivity has important implications to the collection of solid-state NMR data which will be explained in the experimental section of this thesis.

1.3.1 Carbon Black

Elemental carbon comes in a wide variety of forms, and the oldest might be carbon black (CB). It is tempting to think that modern synthesis and manufacturing have produced a refined, improved CB: an advanced descendant of the soot and charcoal that has been being made in nature and by humans for tens of thousands of years. This belief has been proven baseless, however. While there are complicated methods of producing CB on an industrial scale with fine control over surface area, conductivity and many other properties, there is a wide body of research into CB produced from the burning of specific types of wood, rice husks, coconut shells, palm fronds and many other plentiful and renewable sources of organic carbon.⁸⁰⁻⁸³ Morphologically, CB from any source consists of sheets of fused benzene rings arranged in stacks of 10-20, separated by roughly 2.45 Å.⁸⁴⁻⁸⁶ These stacks are closely packed into disordered clusters, forming the microscopic structure of CB. On this scale, CB is textured and highly porous, possessing an extremely high surface area dependant on the synthesis method (ca. 1 km²/g). In this state carbon has significant application for adsorption of gasses and organic compounds. Within this work, CB was studied due to its presence within the catalyst layers of many modern fuel cells. The interaction between current collecting, catalyst supporting CB and the other components of the CCM (Pt nanoparticle catalysts, ionomer) is complicated, but important to understanding the long-term and end-of-life performance of PEM-FCs.

1.3.2 Graphene & Graphene Oxide

One of the largest breakthroughs in the field of nanostructured materials came with the cheap and easy production of graphene, single sheets of sp^2 -hybridized carbon atoms.^{87, 88} These sheets possess extremely interesting thermal, mechanical, and electronic properties, and so they are expected to find application in the development of medical, sensor and super-strong composite material technologies among many other examples. Production of graphene sheets may be done (perhaps most famously) by the scotch-tape exfoliation method, where layers of graphene are removed individually from a larger piece of graphite.^{89, 90} It has proven difficult to develop bulk materials based in graphene which share its micro-scale properties. These properties come, chiefly, from the conduction of electrons in two dimensions through the conjugated network of π electrons above and below the sheet: this is the smallest-scale observation of the Hall effect, where a cloud of plasma can conduct electricity due to its liberated electrons. As a result, graphene sheets display uncharacteristically high charge mobility, helping to explain its unusual electronic properties.⁹¹ The pure material has a zero band gap, but graphene can be made into a semiconductor through various means. Chang et al. have recently shown that the doping of isoelectronic boron nitride clusters in graphene opens up a band gap in the material, and the size of this gap is tunable through control of the doping level.^{92, 93} At low levels of doping, for example, a band gap of ca. 600 meV was recorded through X-ray absorption / emission spectroscopies and field effect transistor measurements. Morin et al. have shown that highly graphitized materials or graphene sheets with tightly controlled dimensions (i.e. graphene

nanoribbons) show distinct photoluminescence, a sign that an electronic band gap has been introduced into the material.^{94, 95} In both these cases, it is made clear that the presence of defects, while detrimental to overall electronic conductivity and (likely) mechanical stability, can assist in fine-tuning the electronic properties of graphene.

Graphene can also be made (to a lesser degree of purity) from the oxidation and subsequent reduction of graphite powder.^{96, 97} An intermediate along this pathway is a 2D material of significance: GO.⁹⁸ While the precise structure of GO is still a matter of some debate, a generalized description of the functional groups present in GO is shown in **Figure 1.7**. Technically speaking, the term “graphene” refers to a semi-infinite 2D sheet of sp^2 -hybridized carbon atoms, while “graphite” is used to describe smaller sheets, which may or may not be stacked together. These materials and their derivatives would have significantly different properties. Similar terminology could be used to distinguish between graphene oxide and graphite oxide. For simplicity, the stacks of sheets of oxidized or functionalized sp^2 -hybridized carbon atoms will be referred to as Graphene Oxides.

GO sheets display several differences when compared to graphene sheets or graphite powder as the presence of several oxygen-based functional groups on the surface and edges of graphene-like sheets causes a number of physico-chemical changes. The 3D structure of neatly stacked graphene sheets or graphite powder is disrupted by the presence of surface oxygen groups, and so GO sheets are highly disordered and display no 3D symmetry. The presence of hydroxyl and epoxide groups on the surface makes GO much more hydrophilic than graphite. These

groups also disrupt the π -electron network present in the graphene sheet, meaning GO is less electronically conductive than graphene.^{99, 100} GO paper, made from the slow deposition of GO onto a cellulose acetate screen in a vacuum filtration set-up, has shown remarkable mechanical strength properties, and possesses a respectable in-plane proton conductivity as well.^{101, 102}

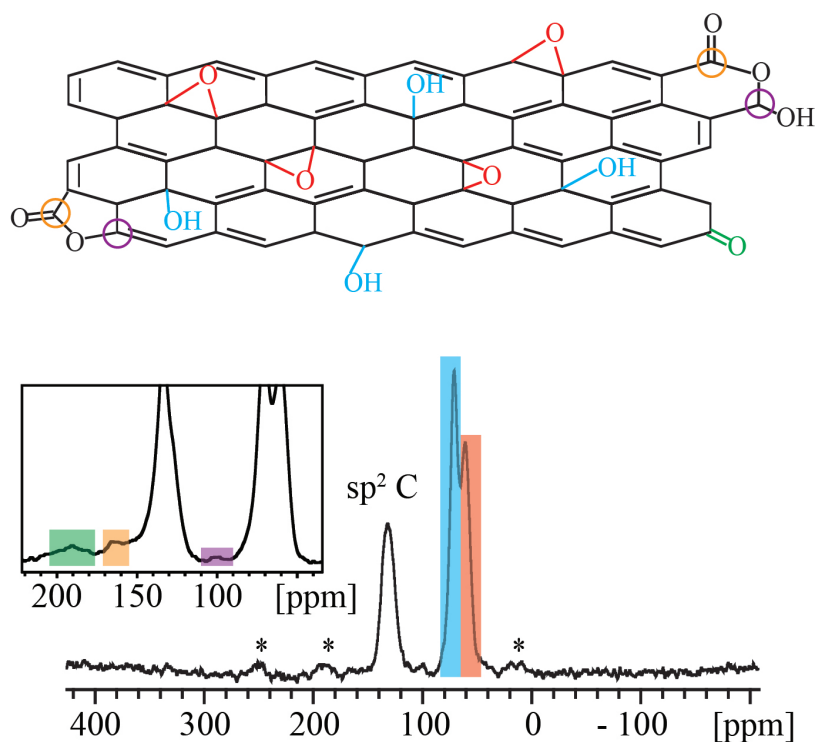


Figure 1.7: The molecular structure of Graphene Oxide (GO), and a $^1\text{H} \rightarrow ^{13}\text{C}$ CPMAS NMR spectrum (11.7 T, 15 kHz MAS) with site assignments.¹⁰³

The introduction of oxygen-based functional groups to a graphene sheet means that these groups can be used as handles on which to do further functionalization chemistry. GO, being a 2D hydrophilic material, is highly receptive to non-covalent bonding.^{104, 105} The planar graphene sheets bond well to high surface area polymers, such as polysaccharides, and these functionalized graphenes have been used as biomarkers for drug carrier and delivery systems.^{106, 107} Covalent functionaliza-

tion is being investigated as well, especially as it generally affects the electronic and thermal properties of the basal graphene sheet.¹⁰⁸⁻¹¹⁰ A remarkable amount of work has been done to try to ‘normalize’ graphene and make it accessible to researchers everywhere, and what has been reported here is certainly only the first glimpse into the interesting world of graphene chemistry.

1.3.3 Carbon Nanotubes

Carbon nanotubes (CNTs) have been known to exist for around 70 years, have been readily synthesized for nearly 50 years, and have enjoyed particular research attention.^{111, 112} This insurgence is likely due to two factors: first, the development of new and facile synthesis methods and second, the interesting properties of modified or composite materials based in CNTs. A ‘perfect’ nanotube (i.e. without defects or modification) can be either metallic or semiconducting depending on how the tube is rolled, producing ‘armchair’, ‘zigzag’, and chiral CNTs.^{113, 114} The size of the semiconductor band gap is related to the style of tube rolling as well as inversely proportional to the diameter of the tubes.¹¹⁵ CNTs may be synthesized as discrete tubes (single-walled, SWCNTs) which can have a diameter between ca. 3 - 20 Å or as nested sets of tubes (multi-walled, MWCNTs) which may have diameters above 100 Å.¹¹⁶ In either case, the length of the tube can be many orders of magnitude larger than the diameter, sometimes extending into the centimeter range. Common synthesis methods for CNTs are based on arc or laser ablation methods, or on chemical vapour deposition, generally requiring a catalyst or seed matrix to select for CNTs above other carbon allotropes.¹¹⁷ This portends

a difficult issue in CNT synthesis; purity. Dispersions of tube length, diameter and even wrapping are ubiquitous in CNT synthesis, which can complicate their accurate study.^{118, 119} Significant progress has been made in the covalent modification of CNTs for purposes including selective separation of different lengths and wrappings among many others.¹²⁰⁻¹²² The cost of pure CNTs is extremely high as a result, and a successful translation of an individual CNT's properties to a macro-scale object (transistors, woven cables for electricity / structural support, etc.) remains an elusive goal. This is not to say that CNTs have no practical application to date. Even at small loading levels, composite materials made of CNTs and polymer or plastic matrices can become semiconductors or conductors, opening the door to novel electrically conductive materials.¹²³⁻¹²⁵ Thanks to their favourable electrochemical properties, CNTs have shown promise when used as electrode materials in supercapacitors. Their capacitance and power density come mostly from their high surface area and the small distance between the conductive surface and ions in the electrolyte.¹²⁶⁻¹²⁸ CNTs have also been investigated for use as electrodes (or in composite electrodes) in ion battery systems, and while they show a remarkably high capacity, they tend to display a less favourable voltage profile and hysteresis when compared to the more commonly used graphite.¹²⁹⁻¹³¹ Applications for CNTs of all types are being uncovered and improved constantly, in these and other related fields such as transistors, displays, nano-scale electronics, quantum computing, and many more. Regarding fuel cells, CNTs have also found application, particularly when used as a support for the platinum catalyst in the electrode layer.^{132, 133} Once again, the high surface area and conductivity

of CNTs allows for increased fuel cell electrochemical performance. In addition, the presence of CNTs in the CCM helps to anchor and stabilize the platinum nanoparticles, reducing degradation and increasing lifetimes. Doped CNTs have been used, with some success, as catalysts themselves.^{134, 135} It is proposed that dopant or defect sites in these CNTs act as active-site-like pockets where reactions are facilitated, particularly the HOR and ORR.

1.4 Motivation and Targets

While fuel cells represent a promising step towards environmentally sound industrial practices, there is an absence in the scientific literature regarding the atomic-scale interactions which improve fuel cell performance. This contrasts with the wealth of engineering literature which reports on significant performance increases in fuel cell systems featuring modified graphitic additives (e.g. GO, sulfonated graphene, heteroatomically doped carbons, etc.) in either the PEM or CCM. For the intelligent design of more effective fuel cells, as well as for the study of graphene chemistry, this thesis details the application of ssNMR techniques on chemically modified carbons and ionomer-carbon composites, also exploring the electrochemical properties of the latter. ssNMR is an invaluable tool for the study of these disordered, complicated materials thanks to the atomic-scale resolution and minute sensitivity it provides. Through NMR, many crucial but vanishingly subtle details about structure and dynamics which may be invisible or ambiguous through other analytical means. Specifically, direct one dimensional NMR experiments focussing on ^1H , ^{13}C , and a number of other nuclei are used to anal-

use the chemical structure of functionalized or doped carbons. 1D heteronuclear experiments are used to probe strongly distance-dependant dipolar interactions between nuclei to explore connectivity. 2D homonuclear and heteronuclear experiments are used to uncover ion exchange pathways and phase changes in composites. Composite impedance, a measure of the efficiency of ion transport through the membrane, is measured at operational conditions through a 4-electrode electrochemical impedance spectroscopy experiment to link ssNMR properties to the reported increase in fuel cell performance over pure PEMs. Details for all relevant experiments used in this thesis are given in **Chapter 2**.

References

- [1] Ellingsen, L. A.-W.; Singh, B.; Strømman, A. H. *Enviro. Res. Lett.* **2016**, *11*(5), 54010.
- [2] Myhre, G.; Highwood, E. J.; Shine, K. P.; Stordal, F. *Geophys. Res. Lett.* **1998**, *25*(14), 2715–2718.
- [3] Ramanathan, V.; Feng, Y. *Atmo. Enviro.* **2009**, *43*(1), 37–50.
- [4] Robertson, G. P.; Paul, E. A.; Harwood, R. R. *Science* **2000**, *289*(5486), 1922–1925.
- [5] Rodhe, H. *Science* **1990**, *248*(4960), 1217.
- [6] Adger, W. N.; Arnell, N. W.; Tompkins, E. L. *Glob. Environ. Chang.* **2005**, *15*(2), 77–86.
- [7] Knutti, R.; Rogelj, J.; Sedláček, J.; Fischer, E. M. *Nature Geosci.* **2016**, *9*(1), 13–18.
- [8] Solomon, S.; Plattner, G.-K.; Knutti, R.; Friedlingstein, P. *Proc. Natl. Acad. Sci.* **2009**, *106*(6), 1704–1709.
- [9] Thuiller, W.; Lavorel, S.; Araújo, M. B.; Sykes, M. T.; Prentice, I. C. *Proc. Nat. Acad. Sci.* **2005**, *102*(23), 8245–8250.
- [10] Vörösmarty, C. J.; Green, P.; Salisbury, J.; Lammers, R. B. *Science* **2000**, *289*(5477), 284–288.
- [11] Obama, B. *Science* **2017**, *355*(6321), 126–129.
- [12] Stern, N. H. *The Economics of Climate Change: the Stern Review*; Cambridge University Press, **2007**.
- [13] Foley, A. M.; Leahy, P. G.; Marvuglia, A.; McKeogh, E. J. *Renew. Energ.* **2012**, *37*(1), 1–8.
- [14] Bahnemann, D. *Sol. Energy* **2004**, *77*(5), 445–459.
- [15] Blunden, L.; Bahaj, A. *Proc. Inst. Mech. Eng. A: J. Pow. Energ.* **2007**, *221*(2), 137–146.
- [16] Rourke, F. O.; Boyle, F.; Reynolds, A. *Appl. Energ.* **2010**, *87*(2), 398–409.
- [17] Li, G.; Shrotriya, V.; Huang, J.; Yao, Y.; Moriarty, T.; Emery, K.; Yang, Y. *Nature Mater.* **2005**, *4*(11), 864.
- [18] Stein, W.; Buck, R. *Sol. Energy* **2017**, *152*, 91–105.
- [19] Prasad, A. R.; Natarajan, E. *Energy* **2006**, *31*(12), 1943–1954.
- [20] Lukic, S. M.; Cao, J.; Bansal, R. C.; Rodriguez, F.; Emadi, A. *IEEE Trans. Indust. Elec.* **2008**, *55*(6), 2258–2267.

- [21] Karden, E.; Ploumen, S.; Fricke, B.; Miller, T.; Snyder, K. *J. Pow. Sourc.* **2007**, *168*(1), 2–11.
- [22] Khaligh, A.; Li, Z. *IEEE Trans. Vehic. Tech.* **2010**, *59*(6), 2806–2814.
- [23] Grove, W. R. *Philos. Trans. Royal Soc.* **1843**, *133*, 91–112.
- [24] Barbir, F. *PEM Fuel Cells: Theory and Practice*; Academic Press, **2012**.
- [25] Carrette, L.; Friedrich, K. A.; Stimming, U. *ChemPhysChem* **2000**, (1), 162–193.
- [26] Carrette, L.; Friedrich, K.; Stimming, U. *Fuel Cells* **2001**, *1*(1), 5–39.
- [27] Dyer, C. K. *J. Power Sources* **2002**, *106*(1), 31–34.
- [28] Othman, R.; Dicks, A. L.; Zhu, Z. *Int. J. Hydrogen. Energ.* **2012**, *37*(1), 357–372.
- [29] Chen, Z.; Higgins, D.; Yu, A.; Zhang, L.; Zhang, J. *Energ. Environ. Sci.* **2011**, *4*(9), 3167–3192.
- [30] Susac, D.; Sode, A.; Zhu, L.; Wong, P.; Teo, M.; Bizzotto, D.; Mitchell, K.; Parsons, R.; Campbell, S. *J. Phys. Chem. B* **2006**, *110*(22), 10762–10770.
- [31] Hoogers, G. *Fuel Cell Technology Handbook*; CRC Press, **2014**.
- [32] Larminie, J.; Dicks, A.; McDonald, M. *Fuel Cell Systems Explained*; John Wiley & Sons, **2008**.
- [33] Mauritz, K. A.; Moore, R. B. *Chem. Rev.* **2004**, *104*(10), 4535–4586.
- [34] Rostrup-Nielsen, J. R. *Catal. Today* **2000**, *63*(2), 159–164.
- [35] Vielstich, W.; Lamm, A.; Yokokawa, H.; Gasteiger, H. A. *Handbook of Fuel Cells: Fundamentals Technology and Applications*, Vol. 2; John Wiley & Sons, **2009**.
- [36] Holdcroft, S. *Chem. Mater.* **2013**, *26*(1), 381–393.
- [37] von Grothaus, C. *Ann. Chim.* **1806**, *58*(54).
- [38] Kreuer, K.-D.; Rabenau, A.; Weppner, W. *Angew. Chem. Int. Ed.* **1982**, *21*(3), 208–209.
- [39] Luduena, G. A.; Kuhne, T. D.; Sebastiani, D. *Chem. Mater.* **2011**, *23*(6), 1424–1429.
- [40] Grot, W. *Chem. Ind.* **1985**, *1*, 647–9.
- [41] Kim, K.-H.; Lee, K.-Y.; Kim, H.-J.; Cho, E.; Lee, S.-Y.; Lim, T.-H.; Yoon, S. P.; Hwang, I. C.; Jang, J. H. *Int. J. Hydrogen Ener.* **2010**, *35*(5), 2119 – 2126.
- [42] Zhang, J.; Giotto, M. V.; Wen, W.-Y.; Jones, A. A. *J. Memb. Sci.* **2006**, *269*(12), 118 – 125.
- [43] Dong, B.; Gwee, L.; Salas-de La Cruz, D.; Winey, K. I.; Elabd, Y. A. *Nano Lett.* **2010**, *10*(9), 3785–3790.

- [44] Ramya, K.; Velayutham, G.; Subramaniam, C.; Rajalakshmi, N.; Dhathathreyan, K. *J. Power Sourc.* **2006**, *160*(1), 10–17.
- [45] Coronado, E.; Galán-Mascarós, J. R.; Gómez-García, C. J.; Laukhin, V. *Nature* **2000**, *408*(6811), 447–450.
- [46] Yang, C.; Srinivasan, S.; Bocarsly, A.; Tulyani, S.; Benziger, J. *J. Memb. Sci.* **2004**, *237*(1), 145–161.
- [47] Ye, G.; Hayden, C.; Goward, G. *Macromolecules* **2007**, *40*(5), 1529–1537.
- [48] Ghassemzadeh, L.; Kreuer, K.-D.; Maier, J.; Muller, K. *J. Phys. Chem. C* **2010**, *114*(34), 14635–14645.
- [49] De Almeida, N. E.; Paul, D. K.; Karan, K.; Goward, G. R. *J. Phys. Chem. C* **2015**, *119*(3), 1280–1285.
- [50] Paul, D. K.; Karan, K.; Docoslis, A.; Giorgi, J. B.; Pearce, J. *Macromolecules* **2013**, *46*(9), 3461–3475.
- [51] Hensley, J. E.; Way, J. D.; Dec, S. F.; Abney, K. D. *J. Memb. Sci.* **2007**, *298*(1), 190–201.
- [52] Slade, S.; Campbell, S.; Ralph, T.; Walsh, F. *J. Electrochem. Soc.* **2002**, *149*(12), A1556–A1564.
- [53] Arcella, V.; Troglia, C.; Ghielmi, A. *Indust. Eng. Chem. Res.* **2005**, *44*(20), 7646–7651.
- [54] Gebert, M.; Ghielmi, A.; Merlo, L.; Corasaniti, M.; Arcella, V. *ECS Trans.* **2010**, *26*(1), 279–283.
- [55] Schaberg, M. S.; Abulu, J. E.; Haugen, G. M.; Emery, M. A.; O’Conner, S. J.; Xiong, P. N.; Hamrock, S. *ECS Trans.* **2010**, *33*(1), 627–633.
- [56] Kordesch, K. V. *J. Electrochem. Soc.* **1978**, *125*, 77.
- [57] Warshay, M.; Prokopius, P.; Le, M.; Voecks, G. In *Energy Conversion Engineering Conference, 1997. IECEC-97., Proceedings of the 32nd Intersociety*, Vol. 1, pages 228–231. IEEE, **1997**.
- [58] Wnek, G.; Ehrenberg, S.; Serpico, J.; Tangredi, T.; Doell, G.; Zador, E. *Fuel Cells Bull.* **1999**, *2*(4), 6–8.
- [59] Bishop, M. T.; Karasz, F. E.; Russo, P. S.; Langley, K. H. *Macromolecules* **1985**, *18*(1), 86–93.
- [60] Huang, R.; Shao, P.; Burns, C.; Feng, X. *J. Appl. Poly. Sci.* **2001**, *82*(11), 2651–2660.
- [61] Li, X.; Wang, Z.; Lu, H.; Zhao, C.; Na, H.; Zhao, C. *J. Memb. Sci.* **2005**, *254*(1), 147–155.

- [62] Luu, D. X.; Cho, E.-B.; Han, O. H.; Kim, D. *J. Phys. Chem. B* **2009**, *113*(30), 10072–10076.
- [63] Mikhailenko, S. D.; Wang, K.; Kaliaguine, S.; Xing, P.; Robertson, G. P.; Guiver, M. D. *J. Memb. Sci.* **2004**, *233*(1), 93–99.
- [64] Wei, G.; Xu, L.; Huang, C.; Wang, Y. *Int. J. Hydrogen Ener.* **2010**, *35*(15), 7778–7783.
- [65] Adamski, M.; Skalski, T. J.; Britton, B.; Peckham, T. J.; Metzler, L.; Holdcroft, S. *Agnew. Chem.* **2017**, *129*(31), 9186–9189.
- [66] Skalski, T. J.; Britton, B.; Peckham, T. J.; Holdcroft, S. *J. Am. Chem. Soc.* **2015**, *137*(38), 12223–12226.
- [67] Umezawa, K.; Oshima, T.; Yoshizawa-Fujita, M.; Takeoka, Y.; Rikukawa, M. *ACS Macro Lett.* **2012**, *1*(8), 969–972.
- [68] Alberti, G.; Casciola, M. *Ann. Rev. Mat. Res.* **2003**, *33*(1), 129–154.
- [69] Mehta, V.; Cooper, J. S. *J. Power Sourc.* **2003**, *114*(1), 32–53.
- [70] Quartarone, E.; Angioni, S.; Mustarelli, P. *Materials* **2017**, *10*(7), 687.
- [71] Kraytsberg, A.; Ein-Eli, Y. *Energy & Fuels* **2014**, *28*(12), 7303–7330.
- [72] Li, Q.; He, R.; Jensen, J. O.; Bjerrum, N. J. *Chem. Mater.* **2003**, *15*(26), 4896–4915.
- [73] Yeo, S. C.; Eisenberg, A. *J. Appl. Polym. Sci.* **1977**, *21*(4), 875–898.
- [74] Zook, L. A.; Leddy, J. *Anal. Chem.* **1996**, *68*(21), 3793–3796.
- [75] Zarrin, H.; Higgins, D.; Jun, Y.; Chen, Z.; Fowler, M. *J. Phys. Chem. C* **2011**, *115*(42), 20774–20781.
- [76] Tseng, C.-Y.; Ye, Y.-S.; Cheng, M.-Y.; Kao, K.-Y.; Shen, W.-C.; Rick, J.; Chen, J.-C.; Hwang, B.-J. *Adv. Ener. Mat.* **2011**, *1*(6), 1220–1224.
- [77] He, Y.; Tong, C.; Geng, L.; Liu, L.; Lü, C. *J. Memb. Sci.* **2014**, *458*, 36–46.
- [78] Kuila, T.; Mishra, A. K.; Khanra, P.; Kim, N. H.; Lee, J. H. *Nanoscale* **2013**, *5*(1), 52–71.
- [79] Yuan, T.; Pu, L.; Huang, Q.; Zhang, H.; Li, X.; Yang, H. *Electrochim. Acta* **2014**, *117*, 393–397.
- [80] Chuah, T.; Jumariah, A.; Azni, I.; Katayon, S.; Choong, S. T. *Desalination* **2005**, *175*(3), 305–316.
- [81] Hammes, K.; Smernik, R. J.; Skjemstad, J. O.; Herzog, A.; Vogt, U. F.; Schmidt, M. W. *Org. Geochem.* **2006**, *37*(11), 1629–1633.
- [82] Laine, J.; Yunes, S. *Carbon* **1992**, *30*(4), 601–604.

- [83] Salman, J.; Hameed, B. *J. Hazard. Mater.* **2010**, *175*(1), 133–137.
- [84] Bansal, R. C.; Goyal, M. *Activated Carbon Adsorption*; CRC press, **2005**.
- [85] Biscoe, J.; Warren, B. *J. Appl. Phys.* **1942**, *13*(6), 364–371.
- [86] Donnet, J.-B. *Carbon Black: Science and Technology*; CRC Press, **1993**.
- [87] Geim, A. K. *Science* **2009**, *324*(5934), 1530–1534.
- [88] Geim, A. K.; Novoselov, K. S. *Nat. Mater.* **2007**, *6*(3), 183–191.
- [89] Kang, J.; Shin, D.; Bae, S.; Hong, B. H. *Nanoscale* **2012**, *4*(18), 5527–5537.
- [90] Lin, T.; Tang, Y.; Wang, Y.; Bi, H.; Liu, Z.; Huang, F.; Xie, X.; Jiang, M. *Ener. Environ. Sci.* **2013**, *6*(4), 1283–1290.
- [91] Neto, A. C.; Guinea, F.; Peres, N. M.; Novoselov, K. S.; Geim, A. K. *Rev. Mod. Phys.* **2009**, *81*(1), 109.
- [92] Chang, C.-K.; Kataria, S.; Kuo, C.-C.; Ganguly, A.; Wang, B.-Y.; Hwang, J.-Y.; Huang, K.-J.; Yang, W.-H.; Wang, S.-B.; Chuang, C.-H.; others. *ACS Nano* **2013**, *7*(2), 1333–1341.
- [93] Zhang, W.; Lin, C.-T.; Liu, K.-K.; Tite, T.; Su, C.-Y.; Chang, C.-H.; Lee, Y.-H.; Chu, C.-W.; Wei, K.-H.; Kuo, J.-L.; others. *ACS Nano* **2011**, *5*(9), 7517–7524.
- [94] Levesque, I.; Néabo, J. R.; Rondeau-Gagné, S.; Vigier-Carrière, C.; Daigle, M.; Morin, J.-F. *Chem. Sci.* **2014**, *5*(2), 831–836.
- [95] Rondeau-Gagné, S.; Morin, J.-F. *Chem Soc. Rev.* **2014**, *43*(1), 85–98.
- [96] Kang, H.; Kulkarni, A.; Stankovich, S.; Ruoff, R. S.; Baik, S. *Carbon* **2009**, *47*(6), 1520–1525.
- [97] Stankovich, S.; Dikin, D. A.; Piner, R. D.; Kohlhaas, K. A.; Kleinhammes, A.; Jia, Y.; Wu, Y.; Nguyen, S. T.; Ruoff, R. S. *Carbon* **2007**, *45*(7), 1558–1565.
- [98] Hummers Jr, W. S.; Offeman, R. E. *J. Am. Chem. Soc.* **1958**, *80*(6), 1339–1339.
- [99] Dreyer, D. R.; Park, S.; Bielawski, C. W.; Ruoff, R. S. *Chem. Soc. Rev.* **2010**, *39*(1), 228–240.
- [100] Zhu, Y.; Murali, S.; Cai, W.; Li, X.; Suk, J. W.; Potts, J. R.; Ruoff, R. S. *Adv. Mater.* **2010**, *22*(35), 3906–3924.
- [101] Dikin, D. A.; Stankovich, S.; Zimney, E. J.; Piner, R. D.; Dommett, G. H.; Evmenenko, G.; Nguyen, S. T.; Ruoff, R. S. *Nature* **2007**, *448*(7152), 457–460.
- [102] Kumar, R.; Mamlouk, M.; Scott, K. *Int. J. Electrochem.* **2011**, *2011*.
- [103] Cai, W.; Piner, R. D.; Stadermann, F. J.; Park, S.; Shaibat, M. A.; Ishii, Y.; Yang, D.; Velamakanni, A.; An, S. J.; Stoller, M. *Science* **2008**, *321*(5897), 1815–1817.

- [104] Choi, E.-Y.; Han, T. H.; Hong, J.; Kim, J. E.; Lee, S. H.; Kim, H. W.; Kim, S. O. *J. Mat. Chem.* **2010**, *20*(10), 1907–1912.
- [105] Georgakilas, V.; Otyepka, M.; Bourlinos, A. B.; Chandra, V.; Kim, N.; Kemp, K. C.; Hobza, P.; Zboril, R.; Kim, K. S. *Chem. Rev.* **2012**, *112*(11), 6156–6214.
- [106] Bao, H.; Pan, Y.; Ping, Y.; Sahoo, N. G.; Wu, T.; Li, L.; Li, J.; Gan, L. H. *Small* **2011**, *7*(11), 1569–1578.
- [107] Du, D.; Wang, L.; Shao, Y.; Wang, J.; Engelhard, M. H.; Lin, Y. *Anal. Chem.* **2011**, *83*(3), 746–752.
- [108] Compton, O. C.; Dikin, D. A.; Putz, K. W.; Brinson, L. C.; Nguyen, S. T. *Adv. Mater.* **2010**, *22*(8), 892–896.
- [109] Chien, S.-K.; Yang, Y.-T.; Chen, C.-K. *Appl. Phys. Lett.* **2011**, *98*(3), 033107.
- [110] Kuila, T.; Bose, S.; Mishra, A. K.; Khanra, P.; Kim, N. H.; Lee, J. H. *Prog. Mater. Sci.* **2012**, *57*(7), 1061–1105.
- [111] Oberlin, A.; Endo, M.; Koyama, T. *J. Cryst. Growth* **1976**, *32*(3), 335–349.
- [112] Radushkevich, L.; Lukyanovich, V. *J. Phys. Chem. (Moscow)* **1952**, *26*, 88–95.
- [113] Endo, M.; Strano, M. S.; Ajayan, P. M. In *Carbon nanotubes*; Springer, **2007**; pages 13–62.
- [114] Jorio, A.; Kauppinen, E.; Hassaniien, A. In *Carbon Nanotubes*; Springer, **2007**; pages 63–100.
- [115] Baughman, R. H.; Zakhidov, A. A.; De Heer, W. A. *Science* **2002**, *297*(5582), 787–792.
- [116] Dresselhaus, M. S.; Dresselhaus, G.; Eklund, P.; Rao, A. In *The Physics of Fullerene-Based and Fullerene-Related Materials*; Springer, **2000**; pages 331–379.
- [117] Dai, H. *Acc. Chem. Res.* **2002**, *35*(12), 1035–1044.
- [118] Krause, B.; Boldt, R.; Pötschke, P. *Carbon* **2011**, *49*(4), 1243–1247.
- [119] Li, J.; Ma, P. C.; Chow, W. S.; To, C. K.; Tang, B. Z.; Kim, J.-K. *Adv. Funct. Mater.* **2007**, *17*(16), 3207–3215.
- [120] Homenick, C. M.; Lawson, G.; Adronov, A. *Poly. Res.* **2007**, *47*(2), 265–290.
- [121] Liang, S.; Zhao, Y.; Adronov, A. *J. Am. Chem. Soc.* **2014**, *136*(3), 970–977.
- [122] Yang, M.; Gao, Y.; Li, H.; Adronov, A. *Carbon* **2007**, *45*(12), 2327–2333.
- [123] Grossiord, N.; Loos, J.; Regev, O.; Koning, C. E. *Chem. Mater.* **2006**, *18*(5), 1089–1099.
- [124] Han, Z.; Fina, A. *Prog. Poly. Sci.* **2011**, *36*(7), 914–944.

- [125] Zhang, D.; Ryu, K.; Liu, X.; Polikarpov, E.; Ly, J.; Tompson, M. E.; Zhou, C. *Nano Lett.* **2006**, *6*(9), 1880–1886.
- [126] Ma, R.; Liang, J.; Wei, B.; Zhang, B.; Xu, C.; Wu, D. *J. Power Sourc.* **1999**, *84*(1), 126–129.
- [127] Niu, C.; Sichel, E. K.; Hoch, R.; Moy, D.; Tennent, H. *Appl. Phys. Lett.* **1997**, *70*(11), 1480–1482.
- [128] Lu, W.; Qu, L.; Henry, K.; Dai, L. *J. Power Sourc.* **2009**, *189*(2), 1270–1277.
- [129] Liu, X.-M.; dong Huang, Z.; woon Oh, S.; Zhang, B.; Ma, P.-C.; Yuen, M. M.; Kim, J.-K. *Compos. Sci. Tech.* **2012**, *72*(2), 121–144.
- [130] Wang, W.; Ruiz, I.; Guo, S.; Favors, Z.; Bay, H. H.; Ozkan, M.; Ozkan, C. S. *Nano Ener.* **2014**, *3*, 113–118.
- [131] Cheng, J.; Wang, B.; Park, C.-M.; Wu, Y.; Huang, H.; Nie, F. *Chem. Euro. J.* **2013**, *19*(30), 9866–9874.
- [132] Matsumoto, T.; Komatsu, T.; Arai, K.; Yamazaki, T.; Kijima, M.; Shimizu, H.; Takasawa, Y.; Nakamura, J. *Chem. Comm.* **2004**, (7), 840–841.
- [133] Li, W.; Wang, X.; Chen, Z.; Waje, M.; Yan, Y. *Langmuir* **2005**, *21*(21), 9386–9389.
- [134] Cruz-Silva, E.; Cullen, D. A.; Gu, L.; Romo-Herrera, J. M.; Muñoz-Sandoval, E.; López-Urías, F.; Sumpter, B. G.; Meunier, V.; Charlier, J.-C.; Smith, D. J. *ACS Nano* **2008**, *2*(3), 441–448.
- [135] Cruz-Silva, E.; Lopez-Urias, F.; Munoz-Sandoval, E.; Sumpter, B. G.; Terrones, H.; Charlier, J.-C.; Meunier, V.; Terrones, M. *ACS Nano* **2009**, *3*(7), 1913–1921.

2 — Experimental Methods

This chapter will describe the theory and practice behind the analytical techniques used for these studies. The method of solid-state nuclear magnetic resonance (ssNMR) spectroscopy will receive the most focus, due to its complexity and the relative amount of data it produced. A brief explanation of electrochemical impedance spectroscopy (EIS) is also provided. Synthetic methods for the samples mentioned in this work are included in the introductions to their relevant chapters, and so are omitted here.

2.1 Solid-State Nuclear Magnetic Resonance (ssNMR)

ssNMR spectroscopy is a versatile, ubiquitous, nuanced analytical technique which exploits almost imperceptible differences between magnetic and/or electronic environments within a molecule or material.¹⁻⁵ While ssNMR is technically low in sensitivity compared to other methods, it provides extremely high specificity and resolution. An enormous variety of experiments, targeting molecular structure & purity, dynamics, kinetics, micro-imaging and many others, are possible with it. This section will describe the origin of signal in a ssNMR experiment, the interactions between nuclei and electromagnetic fields, and detail the ssNMR experiments routinely used in this work.

2.1.1 Signal Origin & The Zeeman Effect

Nuclei consist of protons and neutrons, which are in turn made up of elementary particles, specifically, quarks held together by gluons (the force mediator particle of

the strong nuclear force).⁶ Quarks are Fermionic sub-atomic particles which possess an inherent angular momentum known as spin, represented by the quantum number I , which must equal a half-integer (integer spin particles, like the gluon, are known as Bosons). Being made up of particles with spin angular momentum, certain nuclei themselves can therefore possess spin. Nuclear spin depends on how many nucleons of which type are present in an atom, and predicting it can quickly become very complicated for larger nuclei. A quick guideline is that a nucleus with odd numbers of both protons and neutrons will have an integer spin (e.g. ^{14}N , $I = 1$, ^{10}B , $I = 3$) while nuclei with mixed-parity numbers of protons and neutrons (i.e. odd-even or even-odd) will have a half-integer spin (e.g. ^1H , $I = \frac{1}{2}$, ^{23}Na , $I = \frac{3}{2}$). Nuclei with even numbers of protons and neutrons (e.g. ^{12}C) have no spin and are NMR inactive.

Nuclear spin differs significantly from classical or orbital angular momentum, but they are similar enough that it can be useful to think of them in similar terms. As a result, a “spinning” positively charged nucleus will produce a magnetic field, as any moving charge would (an effect described closely by the Biot-Savart law). Absent any applied magnetic field, a bulk sample of well-separated spins would have no magnetization: the overall bulk magnetization vector for a sample of nuclei is zero since each nuclear magnetic dipole has no preferred orientation. Within an external magnetic field, however, the Zeeman effect of quantum mechanics establishes certain stable orientations for the nuclear spins, called spin states.⁷

The spin-state energy levels are quantized, and the number of allowed energy levels is fixed by the spin quantum number of the nucleus in question to $2I + 1$. An illustration of the effect of a strong magnetic field on a small population of nuclear spins is shown in **Figure 2.1**.

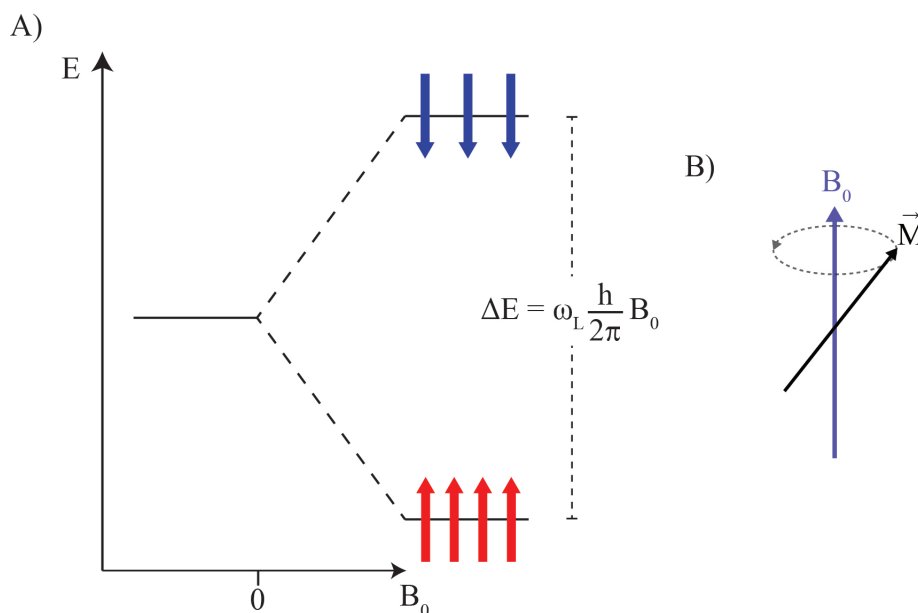


Figure 2.1: A) A schematic representation of the Zeeman effect. As the strength of the applied magnetic field, B_0 , increases the nuclear magnetization vectors of $I = \frac{1}{2}$ NMR-active nuclei will align with (red) or against (blue) that field. This results in two distinct spin states separated by a field-dependent energy, ΔE . The difference in energy results in a population difference between these two states, giving rise to a bulk magnetization vector. B) The bulk magnetization vector, \vec{M} , precesses about the applied field, B_0 , at the Larmor frequency, ω_L .

The difference in energy between these spin states is orders of magnitude smaller than the ambient thermal energy at room temperature, and so a roughly equal population of spins exists in each spin state. Taking a proton nucleus as an example ($I = \frac{1}{2}$, $\gamma = 26.75 \times 10^7 \text{ rad T}^{-1} \text{ s}^{-1}$);

$$\Delta E = h\nu = \frac{h}{2\pi} \gamma B_0 \quad (2.1)$$

$$\frac{n_{\text{upper}}}{n_{\text{lower}}} = e^{-\frac{\Delta E}{kT}} \quad (2.2)$$

where ΔE is the difference in energy levels between the two allowed spin states, h is Planck's constant, ν is the frequency of this energy difference, γ is the gyromagnetic ratio ($\text{rad T}^{-1} \text{ s}^{-1}$), an intrinsic parameter of the nucleus in question, B_0 is the strength

of the applied magnetic flux density, $\frac{n_{upper}}{n_{lower}}$ is the population ratio between allowed states, and k is the Boltzmann constant.

It is clear that only a small excess of nuclear spins exists in the lower energy spin state, and this is the root of the innate lack of sensitivity of NMR spectroscopy. Other nuclei besides ^1H show even smaller differences between numbers of spins in the high and low energy Zeeman states and poorer sensitivity, since ^1H has the highest gyromagnetic ratio of any stable isotope. This small excess, however, defines the bulk magnetization vector, \vec{M} of the spin population, which aligns with the external field B_0 .

The alignment of \vec{M} is actually a geometrically averaged description of the precession of individual nuclear magnetic moments within the applied field. Each individual spin which makes up the sample magnetization vector precesses around the applied field vector at a rate proportional to the applied field strength and the gyromagnetic ratio;

$$\omega_L = 2\pi\nu = \gamma B_0 \quad (2.3)$$

where ω_L is the so-called Larmor frequency.

2.1.2 Pulses, Relaxation & Signal Acquisition

In the presence of a strong externally applied magnetic field the nuclei of a sample do not produce observable signals without further perturbation despite their polarization. In order to probe this spin system in a meaningful way, an oscillating magnetic field, B_1 , must be applied in order to mix the high- and low-energy spin states, generating an unstable system which can be observed as it relaxes back to equilibrium. In order to mix these spin states, the perturbing field must be at a frequency which matches the energy difference between states split by the Zeeman effect. This means the field must be on the

same order as radiofrequency radiation (kHz to GHz) at the magnetic fields available to modern NMR spectrometers, and so radiofrequency synthesizers and amplifiers are used to generate probe signals or ‘pulses’. Pulses are generated by passing current through a coil surrounding the sample in the spectrometer probe. The same coil is also used to measure the response of the system after being perturbed.

In a more classical description, the pulse is used to exert torque on the bulk magnetic field vector of the sample nuclei, tipping it from the laboratory z-axis (parallel to B_0) to the lab x-y plane. After being tipped, the motion of the magnetization vector becomes very complicated while returning to an equilibrium state, but is subject to (at least) two different forms of relaxation.⁸ The first is named the spin-lattice relaxation, T_1 , and is a result of energy exchange between the magnetization vector (a set of spins) and its surroundings. This effect is quantified by the relaxation rate constant T_1 , which describes how quickly a perturbed spin system regains magnetization in the direction of the lab z-axis. More practically, the system will take $5 \times T_1$ in order to return to an equilibrium state after a pulse, and so an appropriate recycle delay can be estimated for an experiment if the T_1 is known, even approximately. The second form of relaxation describes the mutual exchange of spin energy within the system itself, which causes the coherent magnetization to dephase irrecoverably after a pulse. This rate is known as spin-spin relaxation, quantified by the rate constant T_2 . A related measure is T_2^* , which takes into account magnetic field inhomogeneity, according to the following equation;

$$\frac{1}{T_2^*} = \frac{1}{T_2} + \frac{1}{T_i} \quad (2.4)$$

where T_i arises from differences in the field across the sample. Practically, the length of T_2 inversely affects the linewidth of the final, processed signal (vide infra). There

are a number of factors which can significantly affect relaxation times, especially when unpaired electrons (e.g. radicals, paramagnetic species) are present in the sample.

Sample magnetization in the x-y plane is the source of signal in an NMR experiment. It is read through the sample generator coil as an induced current. This current oscillates in response to precession and decays under the effects of T_1 and T_2 relaxation. A magnetization vector precessing at a single frequency, for instance, would produce a signal resembling a sine wave which exponentially decays, and the oscillation frequency and rate of decay are effects of the electronic environment of the spin system. Multiple spins in a sample, with slightly different precession rates and relaxation rates (as a result of their site-specific internuclear interactions), will produce a number of oscillating, decaying signals superimposed on each other. In either case, the raw signal is known as a free induction decay (FID), a plot of induced signal intensity with respect to time.

Imaginably, even with a small number of discrete signals, an FID can be difficult to interpret. A Fourier transform is used to convert the time domain signal to the frequency domain, which separates signals into a more readable state with units of frequency, or more commonly parts-per-million (i.e. the ratio between the observed signal precession rate, in Hz, and the pulse frequency, in MHz). The position of signals on this scale, as well as their width and shape, are extremely sensitive to the internuclear interactions experienced by sites within the sample, this being the source of the high selectivity and specificity of NMR.

2.1.3 Relevant Nuclear Interactions

Nuclei are extremely sensitive to their local magnetic and electronic environment, which is perturbed due to the presence of electrons (as well as other nuclei). The strengths of these internuclear interactions can change the precession frequency of nuclear

spins at specific molecular sites as much as several kHz or even MHz, which is the source of discrimination between similar nuclei based on their position and surroundings in a sample. Two of the most common interactions happen to be less important to the work in this thesis: scalar (or J) spin-spin coupling, a kHz-range through-bond interaction; and quadrupolar coupling, a potentially MHz-range interaction affecting nuclei with spins higher than $I = \frac{1}{2}$, and so explanations for these two interactions are omitted here. Explanations of the chemical shift and dipolar coupling interactions follow.

2.1.3.1 Magnetic Shielding & Chemical Shift

The chemical shift interaction arises as an effect of the external applied field on the electrons in a molecule or material.⁹ A circulation of electrons within molecular orbitals induces a small counter field, which means that the field ‘felt’ by any nucleus is being affected by the precise electronic environment around it. This effect is simple to model for a hypothetical single nucleus with a spherically symmetric electron cloud; the induced field runs opposite to the applied field and shrinks the energy difference between Zeeman spin states by a small amount, i.e., the nucleus is shielded from the external field by the induced field from its electron cloud. Molecular orbitals are not spherically symmetrical, and so the induced field may add or subtract from the external field and shield or deshield the nucleus depending on the symmetry of the molecule.

In a solid powder sample, an infinite number of static molecular orientations are present, and so the orientation-dependence of the strength of the chemical shift interaction becomes evident. This is not the case for solution NMR, where the rate of molecular rotation for small molecules is on the nano- to picosecond order, much faster than the effects of the second to millisecond order of inverse chemical shift anisotropies. The directional dependence of chemical shielding is therefore averaged to an isotropic value,

σ_{iso} , over the course of a solution-state NMR experiment. In the laboratory axis system, this orientation dependence can be described by a second-rank tensor:

$$\sigma = \begin{bmatrix} \sigma_{xx} & \sigma_{xy} & \sigma_{xz} \\ \sigma_{yx} & \sigma_{yy} & \sigma_{yz} \\ \sigma_{zx} & \sigma_{zy} & \sigma_{zz} \end{bmatrix} \quad (2.5)$$

which can be diagonalized for symmetric σ tensors by shifting to a principle axis system, PAS.

$$\sigma^{PAS} = \begin{bmatrix} \sigma_{11} & 0 & 0 \\ 0 & \sigma_{22} & 0 \\ 0 & 0 & \sigma_{33} \end{bmatrix} \quad (2.6)$$

Chemical shielding is therefore described by the three principal values: σ_{11} , σ_{22} , and σ_{33} . For example, consider the highly symmetric carbon dioxide molecule, as seen in **Figure 2.2**. Two of the principal shielding values are equivalent in carbon dioxide thanks to its symmetry, so there exists one unique chemical shift with the molecule aligned parallel to the external field, described by σ_{\parallel} , and a second unique chemical shift with the molecule aligned in any of the infinite orientations perpendicular to it, described by σ_{\perp} . The signal frequency in between these two shifts comes from their linear combination as a response to the infinite number of possible molecular orientations between σ_{\parallel} and σ_{\perp} . This gives rise to an NMR spectrum with a distinctive ‘powder pattern’. For a molecule with less than cylindrical symmetry, the powder pattern indicates all three components of the chemical shielding separately.

σ_{iso} represents the weighted average of the chemical shielding tensor components, as would be seen in a comparable solution spectrum where they are averaged by rapid molecular motion. Two other shielding parameters, anisotropy, Ω , and asymmetry, η , in

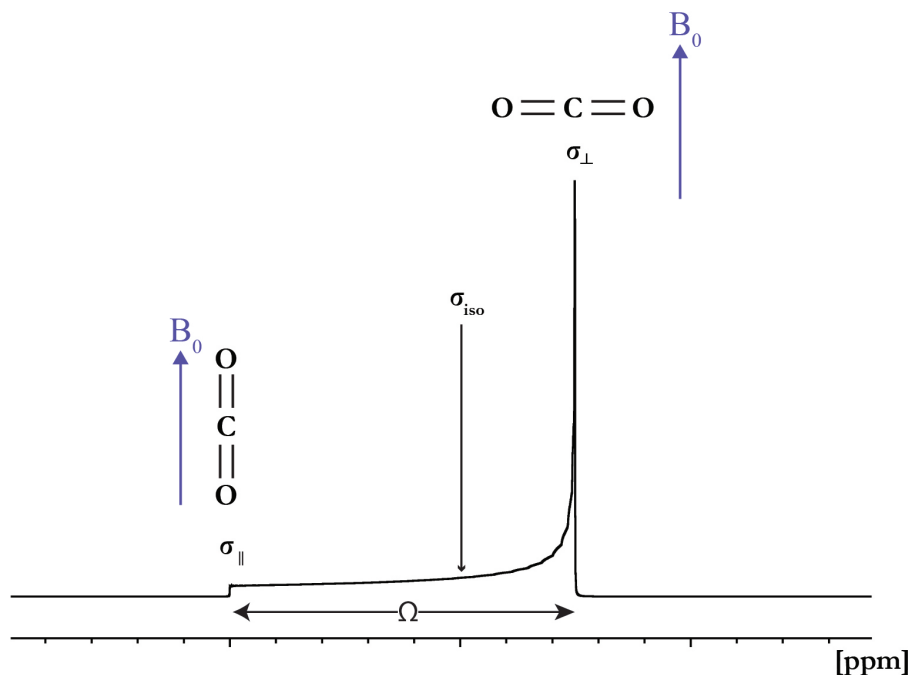


Figure 2.2: A simulated ^{13}C stationary sample powder pattern of CO_2 , indicating the components of the chemical shift tensor, σ_{\parallel} and σ_{\perp} , the isotropic chemical shift, σ_{iso} , and the span, Ω . The signal frequency is dependent on the orientation of the CO_2 molecule with respect to B_0 , while the signal intensity is dependent on the probability of that orientation in the sample.

In addition to σ_{iso} , are commonly used as alternative variables to the tensor components shown above:

$$\sigma_{iso} = \frac{\sigma_{11} + \sigma_{22} + \sigma_{33}}{3}$$

$$\Omega = \sigma_{33} - \sigma_{iso} \quad (2.7)$$

$$\eta = \frac{\sigma_{22} - \sigma_{11}}{\sigma_{33} - \sigma_{iso}}$$

The frequency of a nucleus in any individual molecule or crystallite as a result of chemical shielding can be described as follows:

$$\omega_{CS}(\theta, \phi) = \omega_0 \left(\sigma_{iso} + \frac{\Omega}{2} (3\cos^2\theta - 1) + \eta (\sin^2\theta \cos^2 2\phi) \right) \quad (2.8)$$

where θ and ϕ describe the polar and azimuthal angles, respectively, of the spherical coordinates of the B_0 field in the principal axis system, and ω_0 is the frequency of a bare nucleus (as in **Equation 2.3**). The spherical integral of this equation produces the powder pattern of the static NMR signal.

Chemical shielding is by definition a frequency shift with respect to the Larmor frequency of the nucleus in question absent any internuclear or electronic interactions. It is much more common to use the chemical shift scale (δ , generally in units of ppm), which compares an analyte sample to the signal of a reference sample. An ideal reference material would be chemically inert in order to be applicable as an internal standard and should quickly produce sharp signals which are well resolved from sample peaks (in addition to being inexpensive and easy to handle in the laboratory). Generally these standards have high symmetry or mobility. Common examples of NMR standards in solution include tetramethyl silane (for ^1H , ^{13}C , and ^{29}Si), phosphoric acid (for ^{31}P), and ammonium chloride (for ^{15}N).^{10, 11}

2.1.3.2 Dipolar Coupling

The local field experienced by a nucleus is modified by the induced fields from other nuclei nearby to it. This highly distance-dependent through-space interaction is known as dipolar coupling, and can have a significant effect on spectra, especially in the solid state.² The ‘alphabet’ expression of the dipolar Hamiltonian reads as follows;

$$\begin{aligned}
 \hat{H}_D &= -\left(\frac{\mu_0}{4\pi}\right)\left(\frac{\gamma_I\gamma_S\hbar^2}{r_{IS}^3}\right)(A + B + C + D + E + F) \\
 A &= \hat{I}_{Iz}\hat{I}_{Sz}(3\cos^2\theta - 1) \\
 B &= -\frac{1}{4}(\hat{I}_I^+\hat{I}_S^- + \hat{I}_I^-\hat{I}_S^+)(3\cos^2\theta - 1) \\
 C &= -\frac{3}{2}(\hat{I}_I^+\hat{I}_{Sz} + \hat{I}_{Iz}\hat{I}_S^+)(\sin\theta\cos\phi)e^{-i\phi} \\
 D &= -\frac{3}{2}(\hat{I}_I^-\hat{I}_{Sz} + \hat{I}_{Iz}\hat{I}_S^-)(\sin\theta\cos\phi)e^{i\phi} \\
 E &= -\frac{3}{4}(\hat{I}_I^+\hat{I}_S^+)(\sin^2\theta)e^{-2i\phi} \\
 F &= -\frac{3}{4}(\hat{I}_I^-\hat{I}_S^-)(\sin^2\theta)e^{+2i\phi}
 \end{aligned} \tag{2.9}$$

where μ_0 is the permeability of free space, $\gamma_{I,S}$ are the gyromagnetic ratios of spins I and S, r and θ represent the internuclear distance and angle with respect to the lab z-axis between spin I and S, and \hat{I} are operators representing the denoted component of nuclear spin angular momentum.⁸ However, terms C to F do not commute with the Zeeman Hamiltonian and so do not change the energy level of Zeeman states to an appreciable degree. They can affect relaxation, but in general these terms are negligible. In cases of heteronuclear coupling, the effects of the B term becomes small enough to ignore as well, and the Hamiltonian is further simplified.

The strength of the dipolar coupling between nuclei is extremely sensitive to internuclear distance, and can be an important metric of structure and dynamics in solids. It is described by the dipolar coupling constant, D , which is calculated as follows:

$$D = \left(\frac{\mu_0}{4\pi}\right)\left(\frac{\gamma_I\gamma_S}{r_{IS}^3}\right)\left(\frac{\hbar}{2\pi}\right) \tag{2.10}$$

Dipolar coupling is an additive effect, and so it is strongest where there are a large concentration of spins with high γ values. In solutions the angular term of the dipolar

Hamiltonian becomes time dependent, and thanks to rapid molecular tumbling the effect of dipolar coupling on a solution spectrum is negligible (except for relaxation rates).

2.1.4 Solids & Magic Angle Spinning

Signals from a solid sample can be as broad as several kHz or MHz, and interpretation of a spectrum with an increasing number of signals quickly becomes nontrivial.^{1, 12-14} As highlighted in **Equation 2.9** above, an angular dependence of the dipolar interaction (in the more important A and B terms) is noted by the term $3\cos^2\theta - 1$, where θ represents the angle between the lab z-axis and the internuclear vector. In a static powder sample, an infinite number of these angles might exist, meaning that an array of interactions of different strengths may lead to a large band of different Zeeman states and broad signals. **Equation 2.8** indicates that the CS interaction also displays a similar angular dependence, and CSA can have a severe detrimental effect on signal resolution and spectral interpretation.

The method of magic angle spinning (MAS) is used to reduce the contributions of the orientation-dependent parts of these interactions in the solid state to allow the collection of interpretable spectra with narrower signals. A solid sample is packed into a sample tube with a finned drive tip, or rotor, and spun at an angle of 54.74° , the ‘magic’ angle which sets the term $3\cos^2\theta - 1$ to 0. Spinning is achieved by passing pressurized gas along the rotor to relieve friction and across the drive tip fins to induce spinning: the current fastest spinning speeds available exceed 100 kHz, or six million rpm. This practice introduces a time dependence to these anisotropic interactions, and the aim is to achieve a spinning rate faster than the effect of those interactions. As a result, the angular term of the dipolar Hamiltonian is averaged to 0 over one rotation in a rapidly

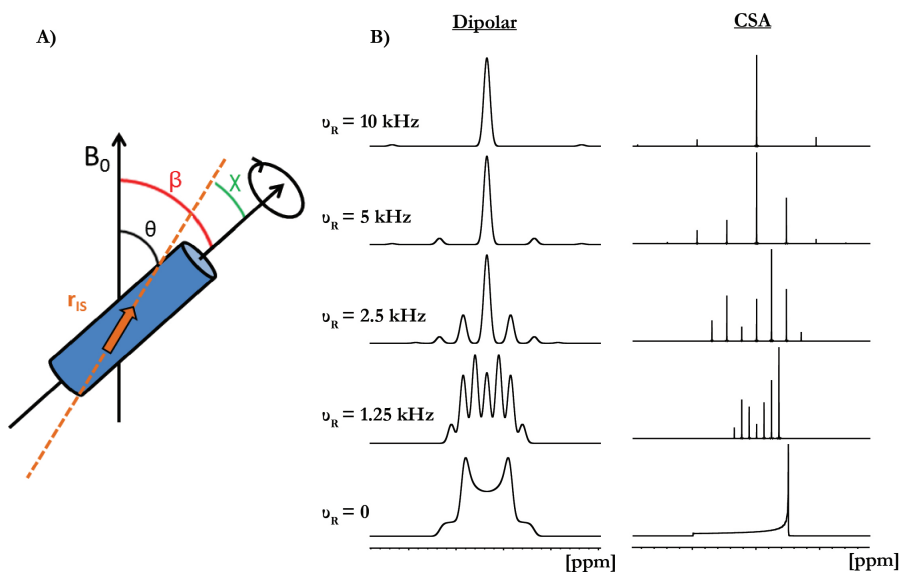


Figure 2.3: A) An illustration of hypothetical dipolar interaction between spins I and S, separated by vector r_{IS} , inside the MAS rotor. There are an infinite number of angles, θ , in a powder sample, however rapid spinning about the magic angle β , 54.74° , causes these angles to rapidly cycle between $\beta + \chi$ and $\beta - \chi$, allowing for reduction of broadening under sufficiently fast MAS.¹² B) Simulated spectra indicating the effect of increasing MAS rate on the dipolar and chemical shift interactions. Without MAS ($\nu_R = 0$), dipolar coupling causes a mirrored powder pattern, the Pake doublet, due to the effect of the nuclei's local magnetic fields interacting with one another.¹⁵ As ν_R increases, the broad signal is split into sharper peaks, separated by the MAS frequency. MAS has a similar effect on the CSA interaction due to a similar angular dependence in the CSA Hamiltonian. MAS splits the broad pattern into spinning sidebands and leaving only the isotropic peak at sufficient rates.

spinning rotor, as is the sum of the angular terms in the CS Hamiltonian. An illustration of the MAS rotor and relevant angles is given in **Figure 2.3A**.

MAS can have remarkable effects on the consequences of the dipolar coupling interaction; in all but the most strongly coupled cases (i.e. 1H homonuclear coupling or others where γ values are high) sufficiently fast MAS will largely eliminate dipolar broadening. **Figure 2.3B** shows the effect of an increasing MAS rate on the shape of a hypothetical Pake pattern. Where the strength of the interaction is close to the MAS rate, the coupling is not fully eliminated over the course of the experiment, and instead refocusses once per rotor period in such a way that causes the recorded FID to be periodic. Since the Fourier transform of a periodic function is also periodic, the

broad signal is split into these sidebands, separated by the spinning speed. As spinning speed increases, the sidebands separate further and attenuate while the central signal sharpens and intensifies.

A similar effect of increasing MAS rate on a CS powder pattern is seen in **Figure 2.3B**. The isotropic chemical shift of this site is denoted by the only signal which does not change its position with changing MAS rates; furthermore, this signal is not necessarily more intense than its spinning sidebands nor is it located at the exact centre of the powder pattern. As the spinning speed increases, the intensity of the sidebands, which depends on the symmetry and magnitude of the CSA, decreases and they space apart further from the isotropic peak.

The removal of signal broadening from orientation-dependent nuclear interactions is often a necessity to avoid a spectrum which is crowded with overlapping signals and difficult to interpret. MAS and other decoupling techniques can achieve this in nearly all cases, but in doing so a significant amount of information is sacrificed. The strength of a dipolar coupling interaction, for example, has been used to probe mobility, structure and reaction mechanisms with encouraging success.¹⁶⁻¹⁸ The features of a static powder CSA lineshape can provide structural information of the site it represents.¹⁹⁻²¹ Selectively reintroducing the effects of orientation-dependent nuclear interactions has widespread applications. There are many pulse sequences which aim to do just that, and those used in this thesis are described in the following sections.

2.2 Pulse Sequences

Finally, with pulse lengths and powers properly calibrated, their sample packed into a rapidly spinning rotor and at the strongest and most homogeneous point within the

B_0 field, a spectroscopist can begin to analyze their material. A large (and constantly increasing) number of pulse sequences exist, with even more permutations and variations on those coming along with them. The following sections describe the pulse sequences used most frequently in this thesis.

2.2.1 The Bloch Decay & Spin Echo: Standard ssNMR Pulse Sequences

The Bloch decay experiment, illustrated in **Figure 2.4A** involves applying a single pulse, tipping at least a portion of the bulk z-magnetization into the x-y plane so its precession can induce a current in the RF coil for processing into a spectrum.⁴ One flaw, however, is that the same RF coil must be used to apply the pulse *and* to record the sample's response. The result is that the process of applying a pulse to the sample, switching off the pulse, allowing the current to dissipate and switching on acquisition to record the sample-induced current can become crowded in time, and these steps may overlap slightly. Probe ringing, where the FID contains data points of high intensity early in acquisition, can swamp out the crucial first few points of actual data. It is possible to miss acquiring these first few points due to mistakes in the timing of the acquisition window.

In order to capture the entire FID and produce the most accurate spectra, the spin echo is often used as an alternative. **Figure 2.4B** shows a schematic of the pulse sequence for the Hahn echo: a single channel, two pulse experiment.²² The first 90° pulse is used to generate intensity in the x-y plane, just as it is in a Bloch decay experiment. At this point, the magnetization vector will begin to decay according to T_2 relaxation and differing sites will see their vectors dephase under the effects of differing local interactions. After a fixed amount of time, τ , a second 180° pulse is applied. This pulse

flips the dephasing x-y magnetization, refocussing each spin at the same rate at which it was dephased after the first pulse. After another period of time, τ , the signals have been rephased, and begin to dephase again in the opposite direction, signifying the beginning of the FID and the most intense portion of the titular echo. By this time in the experiment T_2 relaxation has caused at least some signal intensity loss, but there is little to no residual current from the pulses in the RF coil, and so the problem of probe ringing is removed. Acquisition of the FID begins slightly before the top of the echo so the spectroscopist can be sure to collect the entire signal without significant dephasing.

2.2.2 The Carr-Purcell-Meiboom-Gill (CPMG) Sequence: Single-channel Signal Enhancement

CPMG is a signal-enhancement technique which is particularly useful in boosting the signal-to-noise ratio (SNR) of spectra collected from samples with medium to long T_2 relaxation times.^{23, 24} In the pulse sequence, shown in **Figure 2.4C**, is essentially a train of Hahn-echo pulse sequences. Each of the repeating 180° pulses serve to continually refocus the dephasing coherences, resulting in a train of echoes which can be acquired as a FID for 100s of ms or even entire seconds, depending on the T_2 of the sample. This allows the collection of an FID numerous times per scan, resulting in a significant signal-intensity boost. The collected FID is a periodic series of smaller FIDs from the echo, and so the CPMG experiment produces a signal which splits the total amount of signal intensity into evenly spaced spikelets. The actual NMR spectrum is represented by the tops of these spikelets. CPMG provides a high-intensity spectrum over shorter experimental times than many other pulse sequences, however the success of the method is tied intimately to T_2 , and so its performance can be highly sample specific.

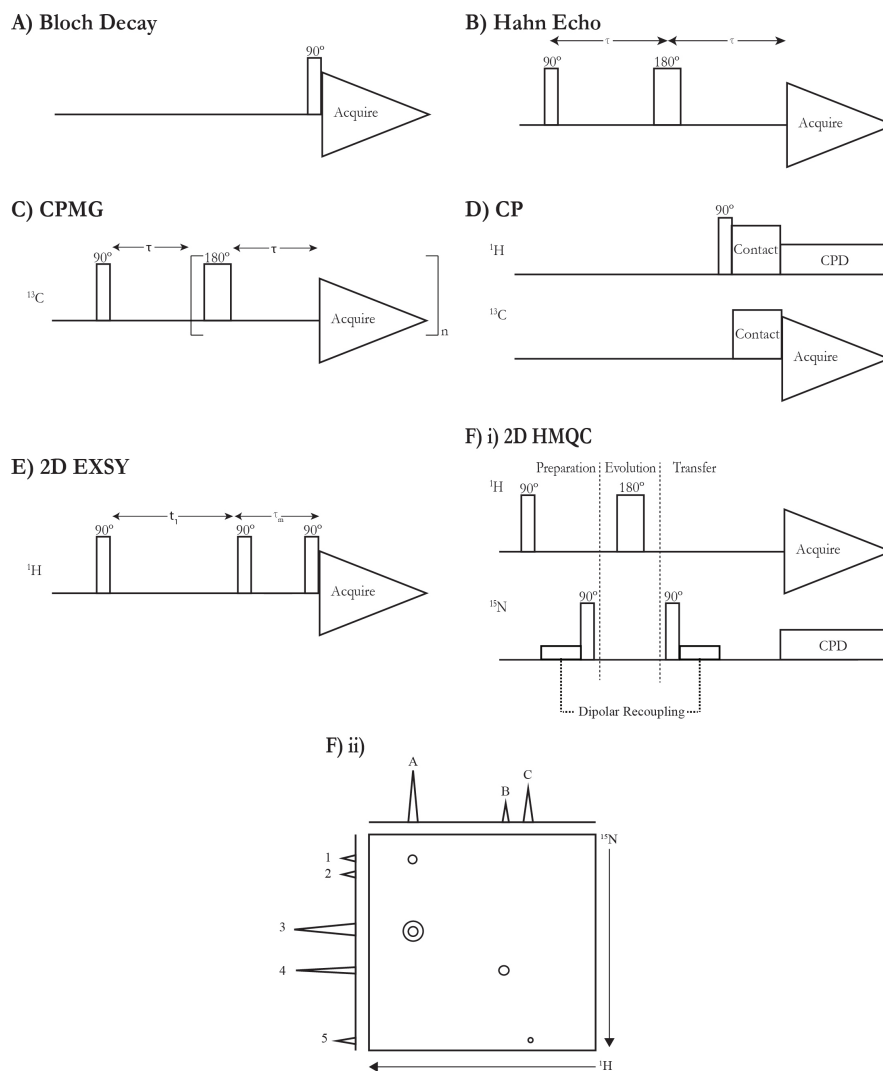


Figure 2.4: Schematics of the pulse sequences used most routinely for this thesis: A) the Bloch decay, B) the Hahn echo, C) the Carr-Purcell-Meiboom-Gill sequence, D) cross polarization, E) the Exchange Spectroscopy sequence, F)i) the heteronuclear multiple quantum coherence sequence with ii) a simulated set of 2D HMQC data.

2.2.3 Cross Polarization

Often the most interesting and important results from a ssNMR study involve the least intense signals, or the least receptive nuclei. A classic example is that of ^{13}C NMR, which has been used with remarkable success in the analysis of molecules of all sizes in solution and the solid state, despite ^{13}C NMR being an unremarkable NMR nucleus (ca. 1% natural abundance, generally long T_1 values leading to long experimental times,

etc.). As a result, it is often advantageous or necessary to boost signal intensity above what can be gotten from a poor spin system on its own, and cross polarization (CP) is a useful method to do so.

CP involves polarization transfer from a highly receptive spin system, I, generally ^1H , ^{19}F or another receptive and abundant nuclide, to a less receptive system, S.²⁵ The major benefit of CP spectroscopy comes from signal enhancement: the theoretical maximum improvement in signal strength matches the ratio of the γ values for spin systems I and S, and so a quadrupling of signal intensity for $^1\text{H} \rightarrow ^{13}\text{C}$ CP spectra over direct ^{13}C spectra, a ten-fold increase for $^1\text{H} \rightarrow ^{15}\text{N}$ CP, etc. can theoretically be achieved. A frequently made analogy for this process is the transfer of thermal energy between two glass beakers filled with cold and hot water. When the beakers are brought into contact with each other energy will flow as heat from the hot to the cold beaker until equilibrium is reached. The CP pulse sequence, shown in **Figure 2.4D**, begins by tipping the I magnetization into the x-y plane, followed by a contact (or spin-lock) pulse on both channels. The goal of this contact pulse is to have the I-S spin system meet the Hartmann-Hahn matching condition, i.e. to have them both stationary within their own rotating frame of reference. Under these conditions, the spin system energy level splittings for each nuclide are matched sufficiently that entropic transfer of magnetization can occur, and so signal intensity is transferred to the poorer S spin system. This transfer of magnetization is mediated by the dipolar coupling interaction, and so as a result it has a strong through-space distance dependence. As the length of this contact pulse is increased, the signal intensity transfer becomes more efficient, up to a point. Eventually, the signal will begin to decay under the effects of $T_{1\rho}$ relaxation, a relaxation parameter similar to T_1 but applicable to the rotating frame.²⁶ The maximum signal transfer is therefore dependent on a number of variables and so a proper contact time needs to be

calibrated for each sample. After the magnetization transfer occurs for as much time as the spectroscopist deems necessary (typically 1 - 10 ms), an FID is acquired from the spin-poor system's channel.

An added feature of CP spectroscopy is that it is only necessary for the receptive spin system to relax fully between scans. Especially in the common case where the typically fast-relaxing ^1H is the main source of magnetization, this means that more scans can be performed per unit time than in a direct spectrum of the low receptivity system, further increasing experimental efficiency. A CP spectrum, unlike a direct one, is not quantitative. Signal intensity is based not only on site population but on proximity to the polarizing nuclei as well. Progress is being made to re-equip the signal boosting CP method with the ability to quantize signal intensity.^{27, 28}

2.2.4 2D NMR Experiments

2D NMR has been used extensively in mapping correlations in materials, perhaps most productively in the study of biological macromolecules.²⁹ There are four general sections to the pulse sequence of any 2D NMR experiment. In the initial preparation period, the equilibrium bulk magnetization vector is perturbed as in any NMR experiment (e.g. by the application of a 90° pulse). Next, this new coherence is allowed to evolve and relax over an incremented evolution period. The evolved coherence is then transformed into an observable coherence during the mixing period before being recorded in the fourth and final detection period. The end result after Fourier transformation is a 2D spectrum where each topographical point has an intensity and two frequency coordinates.

One such experiment used in this thesis, 2D exchange spectroscopy (EXSY), reveals different signals which are in chemical exchange with one another, or in spin exchange.

The EXSY pulse sequence is shown in **Figure 2.4E**. Initially, magnetization is tipped into the x-y plane and allowed to evolve under the effects of chemical shift for a short time, t_1 . Two 90° pulses follow t_1 , separated by a mixing time, t_m . If one site is in chemical exchange with another over the time scale of the mixing period, this pulse train would result in an exchange of signal intensity between these two sites. After the final 90° pulse the FID is recorded, and the process is repeated at the next incremented evolution time. The end result would be a 2D EXSY spectrum with a cross peak shared between two sites which are in chemical exchange with one another. By changing the mixing time, exchange dynamics over different time scales can be probed, i.e. cross peaks present at shorter mixing times indicate that those two sites are in rapid exchange. During the mixing time, spin exchange may begin to occur whether chemical exchange is possible or not, where a cross peak will appear due to the interaction of two sites near in space to one another exchanging polarization without chemical exchange. The information encoded during the mixing time is highly dependent on spin exchange rates, which vary closely with internuclear distance. As a result the EXSY spectrum can be a useful tool for structure elucidation in certain cases.

Another useful sequence, heteronuclear multiple quantum correlation (HMQC) shown in **Figure 2.4F-i**, is an extremely sensitive tool for probing structure in solid samples.³⁰ In this thesis, the experiment was used to investigate ^1H - ^{15}N interactions. The purpose of the experiment is two-fold: to transfer magnetization between highly and poorly receptive spin systems, and to tie together resonances for these two nuclei to assist in site assignment. The latter purpose is achieved because, in the solid state, the multiple-quantum states under study evolve under the effect of dipolar coupling, which is intensely distance-dependant. These multiple-quantum coherences are shared between two nuclides, and allowed to evolve under the effect of the X-nuclide CS interaction dur-

ing the evolution period. The proton chemical shift is refocussed over this period by a 180° pulse to avoid unwanted ^1H chemical shift evolution. Magnetization is transferred back to the proton spin system before being read out, such that the 1D ^1H spectrum contains only signals from sites very close in space, or even bonded, to ^{15}N sites. Incrementing the evolution time in a rotor-synchronized fashion and Fourier transforming the indirect dimension results in a 2D spectrum where any cross peaks indicate that those two signals represent sites which are either bonded or else extremely close in space to one another. A simulated set of data is shown in **Figure 2.4F-ii**. In this hypothetical sample, proton site A correlates to nitrogen sites 1 and 3, proton site B correlates to nitrogen site 4, proton site C correlates to nitrogen site 5, and nitrogen site 2 is isolated from protons.

2.3 Sample-Specific Considerations

The materials studied in this thesis add yet another layer of complexity and challenge to meaningful analysis by ssNMR. Namely, these graphitic materials may display spectroscopic oddities due to the difficulties of conductive-sample NMR, and the effects of aromatic ring current shifts and paramagnetic nuclear relaxation. These phenomena are the likely cause of the relatively light amount of literature available on the ssNMR analysis of graphitic materials, but significant information can be obtained by accepting these challenges. The following section will describe these three effects, their influence on the ssNMR study of graphitic (or similar) materials, and the methods used to either counteract or account for them.

2.3.1 Sample Conductivity

Some of the materials being studied in this work are electronically conductive on the macroscopic scale; consider again graphene and its functionalized analogues, which contains large π -electron conducting networks of sp^2 carbon atoms. In the rapidly spinning ssNMR rotor, a sample of graphitic material will be compacted by extreme centrifugal force, eventually forming a dense, electrically conductive ‘slug’. Within the intense magnetic field of a NMR spectrometer, a significant local current can be induced within a rotating sample, and these so-called “eddy currents” can cause the sample and rotor to resist movement.^{31, 32} This phenomenon must be considered because the two opposing fields can make it more mechanically difficult to spin a rotor containing a conductive material. Higher pressures of bearing and drive gasses must be used to achieve the same spinning rates than would be necessary for a typical sample, and spinning can be much less stable as a result as well.

In addition, the presence of a conductive sample can cause severe difficulties in tuning and matching the RF components of the NMR probe. NMR pulses are only effective on their target nuclei as long as the frequency of the applied pulses closely match the precession rate of those nuclear spin magnetization vector precession rates. The RF circuit must be tuned to the appropriate frequency, and part of that circuit is impacted by the relative permittivity of the sample within the coil. Depending on the design of the NMR probe its RF channels may be tunable across a broad spectrum of frequencies, but the presence of a sample with a relative permittivity which is very different from the expected can make it impossible to tune the circuit to the correct frequency.

There are methods to counteract the negative effects of conductive sample NMR, but most have deleterious effects on signal resolution and magnitude. The strength

of the eddy currents is dependent on the strength of the B_0 field, and so working at lower field strengths will partially alleviate the mechanical spinning issues at the cost of signal resolution. It can also help to centre pack the NMR rotor, sandwiching the sample between layers of insulating material and reducing the size of the conductive sample, allowing for weaker eddy currents and a lessened spinning resistance. Dilution of the sample by mixing with an inactive material prevents the formation of a dense conductive material as well. Both of the proceeding solutions, however, will reduce the amount of signal per scan and extend experimental times, and may make sample retrieval challenging or impossible.

2.3.2 Ring Current Shifts

Graphene is made of a network of interlinked benzene rings, and so a curious effect on the chemical shift interaction is noticed when applying NMR to nuclei in close proximity to these rings. Since the π electrons in benzene are delocalized, within a strong magnetic field they will begin to circulate around the ring under the effects of Faradaic induction. This moving charge will produce a small local magnetic field in opposition to the inducing field. Nuclei (e.g. ^1H) nearby to this small field will have their chemical shift precession rates changed depending on the orientation of the nucleus with respect to the local field. This effect is very well known and characterized in similar materials.^{33, 34} The vastly more common case for the materials in this work is for a proton to be localized above or below a benzene ring, and in this orientation the chemical shift of that proton is shifted to lower values. Nuclei localized on the edges of a benzene ring would have their shifts become more positive, but comparing the facial area of the graphene sheet to the area at its edge, the former case is overwhelmingly seen. Ring current shifts cause a relatively small effect (> 10 ppm) to ^1H chemical shift, but considering the small chemical shift

range seen in ^1H spectroscopy (generously speaking ca. 20 ppm total) they are difficult to ignore.

There is very little to be done to eliminate this effect. Moving the nucleus in question away from the graphene sheets would mean fundamentally changing the material under study. Increased mobility can help to alleviate the effect, and so hydration or heating can reduce the effects of a ring current shift. Ultimately, the spectroscopist must appreciate that the sites within these and similar materials will not produce spectra which can be identified by direct comparison with another reference, as their chemical shifts may be different than expected. Each spectrum should be looked at with appropriate scrutiny given to the site assignments.

2.3.3 Paramagnetic Relaxation

Electrons are Fermionic particles possessing a spin angular momentum value of $I = \frac{1}{2}$, and as a result they are subject to probing via magnetic resonance. More accurately, single electrons are magnetic-resonance active, while pairs of electrons, having equal but opposite spin angular momenta, are inactive. As a result, paramagnetic nuclei within a sample can have enormous effects on magnetic resonance studies. This is exploited for the study of paramagnetic materials via the separate but related field of electron paramagnetic resonance (EPR) spectroscopy, and as a signal enhancement technique in the extremely popular NMR-based method of dynamic nuclear polarization (DNP).^{35, 36} A standard NMR experiment is also affected by the presence of paramagnetic nuclei thanks in part to the electron g-factor, g_e , a parameter which is analogous to the nuclear gyromagnetic ratio, γ .

g_e is significantly higher than even the highest nuclear γ , and so coupling between NMR active nuclei and lone electrons is severe. Nuclear relaxation in particular is made

significantly faster in the presence of even small numbers of paramagnetic nuclei, which can cause signal broadening for sites nearby to those nuclei due to shrinking T_2 values.³⁷ In fact, doping with small amounts of paramagnetic material is often used as a method to reduce a prohibitively long relaxation time in order to make an experiment feasible in a reasonable amount of time.^{38, 39} This enhanced relaxation can be a problem in certain circumstances, for example where preservation of signal intensity within the x-y plane is desired.

Certain samples under study in this thesis are synthesized using paramagnetic transition metal ions for oxidation, catalysis, and other purposes. Despite rigorous and thorough work-ups, trace amounts of these metals remain in the purified samples. Removal of these paramagnetic impurities is the only way to remove their effects on spectral acquisition, and this may be achieved with middling success through repeated rinsing with deionized water, but the only way to completely avoid the problem would be not to use paramagnetic reagents in the first place. This strategy was not possible for the goals of this thesis, and so repeated washing and careful sample treatment, coupled with significant trial-and-error, were employed to collect meaningful data from these materials.

2.3.4 Additional Challenges

Two further issues can complicate the ssNMR study of these materials, both arising from the chemical structure of the samples themselves. First, these graphitic materials are highly heterogeneous and as a result, chemically identical nuclei may experience different local environments. A more homogeneous environment around, for example, sp^2 -hybridized carbon atoms in a small molecule would produce a sharp ^{13}C ssNMR signal centered ca. 120 ppm (with respect to a TMS reference). Heterogeneous graphitic

carbons, instead, produce extremely broad ^{13}C signals, centred about the same shift. This signal broadening reduces resolution and necessitates longer experimental times to collect interpretable spectra. Similar to the first point, the magnetic susceptibility of each nanoscopic sample particle is not identical, and as a result there is no isotropy regarding susceptibility for the whole sample within the rotor. Anisotropic bulk magnetic susceptibility causes even further signal broadening due to the presence of an array of slightly different magnetic environments.

2.4 Electrochemical Impedance Spectroscopy (EIS)

In order to measure the bulk electrochemical performance of electrolytes (particularly solids and polymers), the method of electrochemical impedance spectroscopy (EIS) is often employed due to its low cost, ease of use, and high sensitivity.^{40, 41} EIS is routinely used in the study of energy storage materials, sensors, corrosion, and many other fields where a resistance is experienced by the moving charged particles. Broadly speaking this method applies an oscillating test voltage to a sample electrolyte and measures the oscillating current response (or vice versa). An ideal conductor would have no difference in phase between the applied and measured values but real electrolytes impede the responding signal, and this impedance is noted as the ratio between the voltage and current. The impedance of an ideal resistor, consequently, would be independent of oscillation frequency and produce a constant phase shift. Important EIS metrics are calculated from raw data via the following equations:

$$Z(\omega) = \frac{V \sin(\omega t)}{I \sin(\omega t + \theta)} = Z_0 \frac{\sin(\omega t)}{\sin(\omega t + \theta)} = Z_0(\cos\theta + i \sin\theta)$$

$$Z' = Z_0 \cos\theta$$

$$Z'' = Z_0 \sin\theta$$
(2.11)

where Z is the impedance, ω is the frequency of the applied oscillating signal, V is voltage, I is current, t is time, and θ is the difference in phase between the applied and measured signal. The impedance value is further processed into Z' , the resistance, and Z'' , the reactance of the system under investigation through the Euler relationship. Impedance data can be processed and presented in many different ways, but a particularly useful method for solid electrolytes is to plot Z' and Z'' on axes of equal scale, producing a Nyquist plot. A sample Nyquist plot is given in **Figure 2.5**, alongside an equivalent circuit model which is used as a model of the system in order to fit the data.

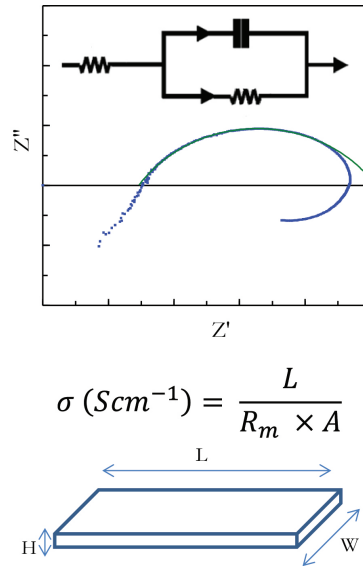


Figure 2.5: A sample Nyquist plot with equivalent circuit model, and a diagram of the electrolyte membrane measurements necessary to calculate proton conductivity, σ .

The model depicts a resistor connected to two components in parallel: a second resistor and a capacitor. Provided that the data is plotted correctly, the key feature of the spectrum, the resistance of the sample membrane, is represented in the circuit diagram

as the resistor connected in parallel, and its resistance is measured as the diameter of the semi-circular regime of the spectrum, R_m , which represents the resistance of the membrane or other solid being probed. In this work, a 4-electrode (working, reference, working counter, and counter) test cell was used to perform EIS. The ionic conductivity, σ , of the membrane can then be calculated:

$$\sigma = \frac{L}{R_m A} \quad (2.12)$$

where L is the distance between the inner working electrodes and A is the cross sectional area of the membrane. The design of the 4-electrode test cell features an exposed membrane, so the environmental conditions (i.e. temperature, relative humidity) can be changed *in-situ* in an environmental test chamber without having to adjust the cell between measurements.

References

- [1] Duer, M. J. *Solid State NMR Spectroscopy: Principles and Applications*; John Wiley & Sons, **2008**.
- [2] Levitt, M. H. *Spin Dynamics: Basics of Nuclear Magnetic Resonance*; John Wiley & Sons, **2001**.
- [3] Rabi, I. I. *Phys. Rev.* **1937**, *51*(8), 652.
- [4] Bloch, F. *Phys. Rev.* **1946**, *70*(7-8), 460.
- [5] Purcell, E.; Pound, R.; Bloembergen, N. *Phys. Rev.* **1946**, *70*(11-12), 986.
- [6] Kane, G. *Modern Elementary Particle Physics: Explaining and Extending the Standard Model*; Cambridge University Press, 2017.
- [7] Zeeman, P.; Bôcher, M. *Nature* **1897**, *55*(347), 3.
- [8] Keeler, J. *Understanding NMR Spectroscopy*; John Wiley & Sons, **2011**.
- [9] Facelli, J. C. *Prog. Nucl. Magn. Reson. Spectrosc.* **2011**, *58*(3-4), 176.
- [10] Hayashi, S.; Hayamizu, K. *Bull. Chem. Soc. Jpn.* **1991**, *64*(2), 685–687.
- [11] Jameson, C. J.; De Dios, A.; Jameson, A. K. *Chem. Phys. Lett.* **1990**, *167*(6), 575–582.
- [12] Andrew, E. *Int. Rev. Phys. Chem.* **1981**, *1*(2), 195–224.
- [13] Andrew, E. R.; Bradbury, A.; Eades, R. *Nature*. **1958**, *182*(4650), 1659–1659.
- [14] Lowe, I. *Phys. Rev. Lett.* **1959**, *2*(7), 285.
- [15] Pake, G.; Purcell, E. *Phys. Rev.* **1948**, *74*(9), 1184.
- [16] Yan, Z. B.; Brouwer, D. H.; Goward, G. R. *Macromolecules* **2016**, *49*(19), 7331–7339.
- [17] Tjandra, N.; Omichinski, J. G.; Gronenborn, A. M.; Clore, G. M.; Bax, A. *Nat. Struct. Mol. Biol.* **1997**, *4*(9), 732–738.
- [18] Prestegard, J.; Bougault, C.; Kishore, A. *Chem. Rev.* **2004**, *104*(8), 3519–3540.
- [19] Kong, X.; Scott, E.; Ding, W.; Mason, J. A.; Long, J. R.; Reimer, J. A. *J. Am. Chem. Soc.* **2012**, *134*(35), 14341–14344.
- [20] Pandey, M. K.; Zhang, R.; Hashi, K.; Ohki, S.; Nishijima, G.; Matsumoto, S.; Noguchi, T.; Deguchi, K.; Goto, A.; Shimizu, T.; others. *J. Magn. Reson.* **2015**, *261*, 1–5.
- [21] Koskela, T.; Ylihautala, M.; Jokisaari, J.; Vaara, J. *Phys. Rev. B* **1998**, *58*(22), 14833.
- [22] Hahn, E. L. *Phys. Rev.* **1950**, *80*(4), 580.

- [23] Carr, H. Y.; Purcell, E. M. *Phys. Rev.* **1954**, *94*, 630–638.
- [24] Meiboom, S.; Gill, D. *Rev. Sci. Instrum.* **1958**, *29*(8), 688–691.
- [25] Hartmann, S.; Hahn, E. *Phys. Rev.* **1962**, *128*(5), 2042.
- [26] Redfield, A. G. *Phys. Rev.* **1955**, *98*(6), 1787.
- [27] Fu, R.; Hu, J.; Cross, T. A. *J. Magn. Reson.* **2004**, *168*(1), 8–17.
- [28] Johnson, R. L.; Schmidt-Rohr, K. *J. Magn. Reson.* **2014**, *239*, 44–49.
- [29] Van de Ven, F. J.; others. *Multidimensional NMR in liquids*; Vch, 1995.
- [30] Tricot, G.; Trbosc, J.; Pourpoint, F.; Gauvin, R.; Delevoye, L. Vol. 81 of *Annual Reports on NMR Spectroscopy*; Academic Press, 2014; pages 145 – 184.
- [31] Aubert, G.; Jacquinet, J.-F.; Sakellariou, D. *J. Chem. Phys.* **2012**, *137*(15), 154201.
- [32] Aguiar, P. M.; Jacquinet, J.-F.; Sakellariou, D. *J. Mag. Res.* **2009**, *200*(1), 6–14.
- [33] Harris, R. K.; Thompson, T. V.; Norman, P. R.; Pottage, C.; Trethewey, A. N. *J. Chem. Soc., Faraday Trans.* **1995**, *91*(12), 1795–1799.
- [34] Harris, R. K.; Thompson, T. V.; Norman, P. R.; Pottage, C. *Carbon* **1999**, *37*(9), 1425–1430.
- [35] Leifson, O.; Jeffries, C. *Phys. Rev.* **1961**, *122*(6), 1781.
- [36] Zavoisky, E. *J. Phys. USSR* **1945**, *9*, 211–245.
- [37] Narayanan, A.; Hartman, J.; Bain, A. *J. Magn. Res. A* **1995**, *112*(1), 58–65.
- [38] Bakhmutov, V. I. *Practical Nuclear Magnetic Resonance Relaxation for Chemists*; John Wiley & Sons, **2005**.
- [39] Foley, I.; Farooqui, S.; Kleinberg, R. *J. Mag. Res., Ser. A* **1996**, *123*(1), 95–104.
- [40] Barsoukov, E.; Macdonald, J. R. *Impedance spectroscopy: theory, experiment, and applications*; John Wiley & Sons, 2005.
- [41] Kreuer, K.-D. *Chemistry of Materials* **1996**, *8*(3), 610–641.

3 — Structure and Dynamics in Functionalized Graphene Oxides through Solid-State NMR

This chapter is a reformatted version of an article previously published in *Chemistry of Materials* (MacIntosh, A.R., Harris, K.J. and Goward, G.R., **2015**, 28(1), 360-367). The co-authors were Kristopher Harris and Gillian Goward. The author was responsible for the synthesis and characterization of all samples as well as the preparation of the manuscript. Multinuclear solid-state NMR (ssNMR) spectroscopy was used to analyze the structure and dynamics of graphene oxide (GO) and a number of sulfonic acid derivatives of GO, both novel and previously reported. ^{13}C CP-MAS spectra showed the disappearance of surface-based oxygen groups upon GO functionalization, and can be used to identify linker group carbon sites in previously synthesized and novel functionalized GO samples with high specificity. Dehydration of these samples allows the collection of ^1H spectra with resolved acidic proton and water peaks. The effect of dehydration on the proton spectrum is partially reversible through rehydration. Deuteration of the acidic groups in high temperature and acidic conditions was virtually unsuccessful, indicating that only the surface and not the intercalated functional groups play a role in the enhanced proton conductivity of ionomer / functionalized GO composites. Increased surface area and increased delamination of functionalized GO is suggested to be important to improved PEM-FC performance. This synthesis and method of analysis proves the utility of ssNMR in the study of structure and dynamics in industrially rel-

evant amorphous carbon materials, despite the obvious difficulties caused by naturally broad signals and low sensitivity.

3.1 Introduction

The development of alternatives to the burning of fossil fuels for energy is one of the most important goals of modern science. Finding a green energy replacement for the automotive sector would reduce dependence on non-renewable energy sources and significantly relieve environmental stresses.¹⁻³ As it stands, there is much work to be done on one of the most promising replacement candidates: the fuel cell.

Proton exchange membrane fuel cells (PEM-FCs) offer a unique alternative to internal combustion by replacing gasoline with hydrogen as a fuel source.^{4, 5} The proton exchange membrane (PEM) is an acidic polymer which generally possesses channels of hydrophilic sulfonic acid groups through which protons can travel. They are shuttled through the cell via either the vehicular or Grotthuss mechanism of proton transport.⁶⁻¹⁰ NafionTM is an industry standard due to its high proton conductivity; however its robustness is less than perfect; performing best under high relative humidity and at a temperature range which is conducive to poisoning of the platinum catalyst layer of the PEM-FC.¹¹⁻¹⁵ The mixing of common PEM materials with functionalized graphene sheets has recently been shown to have a positive effect on proton conductivity.¹⁶⁻¹⁸

Graphene oxide (GO) is a known proton conductor, and can be assembled into stand-alone sheets which possess considerable through-plane proton conductivity (i.e. through the graphene sheet, perpendicular to the two-dimensional sheet itself).^{19, 20} Addition of GO into common PEM materials can cause an order of magnitude increase in the proton conductivity of cast membranes.²¹⁻²³ This effect was noted by Hwang

et al. while investigating GO mixed into sulfonated polyimide / polystyrene sulfonate membranes.¹⁶ They were able to optimize the weight percent of GO composition in order to maximize proton conductivity, doubling that of Nafion at similar humidity and temperature. Other groups have recently studied GO incorporation into other membrane materials, and have examined the effect of the physical properties of GO (sheet size, etc.) on proton conductivity.^{18, 24, 25}

Furthermore, the oxygen-based functional groups on the GO surface have been used as handles for further chemical functionalization with interesting results. Fowler et al. studied the incorporation of GO and sulfonated GO (SGO) into prospective PEM materials.¹⁷ Proton conductivity was measured for both pure samples as well as composites of GO / SGO and Nafion, as a function of temperature and relative humidity. Perhaps surprisingly, the GO composites showed significantly greater proton conductivity than the bare Nafion, particularly at high temperatures where Nafion is known to perform poorly. SGO composites were able to outperform bare GO composites in tests of proton conductivity. They demonstrated an increase in water uptake and ion exchange capacity for the functionalized composite membranes as well.

Generally an analysis of these materials based upon XRD, XPS and TGA is presented in literature along with data indicating the electrochemical performance of composite PEMs. Such a suite of methods can satisfactorily demonstrate that GO/SGO incorporation can have a positive effect on proton conductivity in a polymer composite but fails to provide molecular-level chemical insight into this phenomenon. For this reason, we focus here on the ion-transport and dynamic properties of the functionalized GO themselves. Solid-state NMR (ssNMR) has been used in the past to uncover relationships between PEM and composite materials (organic salts, silica, etc.) with a high degree of precision and sensitivity.²⁶⁻²⁸ There are numerous examples in literature of ¹³C ssNMR studies be-

ing done on a wide range of technological carbon materials including GO, nanodiamond and others.^{29, 30} In addition, ^1H NMR has been used extensively as a tool for investigation bonding motifs and local dynamics in strongly H-bonded systems.³¹⁻³³ Despite the potential information content, there are many challenges with applying ssNMR to modified GO. In addition to the usual issues of low isotopic abundance in the nuclei of interest (specifically ^{13}C) the materials are expected to be amorphous and rigidly H-bonded samples, and there is a strong likelihood of ring-current effects on the NMR resonances of interest. Moreover, the possibility of paramagnetic impurities from the synthesis process makes the collection of useful data challenging. Here we report the syntheses of a number of acid-functionalized GO samples with varying linker groups (see **Figure 3.1**) and their characterization using ssNMR. The products obtained are referred to as graphene oxide (GO), propylsulfonic graphene oxide (Propyl SGO), butylsulfonic graphene oxide (Butyl SGO) and phenylsiloxysulfonic graphene oxide (Phenylsiloxy SGO). The latter two are reported here for the first time, and represent significant developments in the functionalization of graphene. Materials featuring similar siloxy motifs have been used successfully in electrochemical processes, and thus show potential utility in the desired applications.³⁴⁻³⁶

3.2 Experimental

Graphite powder ($<20\ \mu\text{m}$, synthetic), sodium nitrate ($>97\%$), 1,3-propanesultone, 1,4-butanedisultone and trimethoxyphenylsilane were purchased from Sigma-Aldrich. Potassium permanganate (99%) was purchased from Caledon Laboratories Ltd. Hydrogen peroxide (30%) was purchased from Fischer Chemical. All chemicals were used as received.

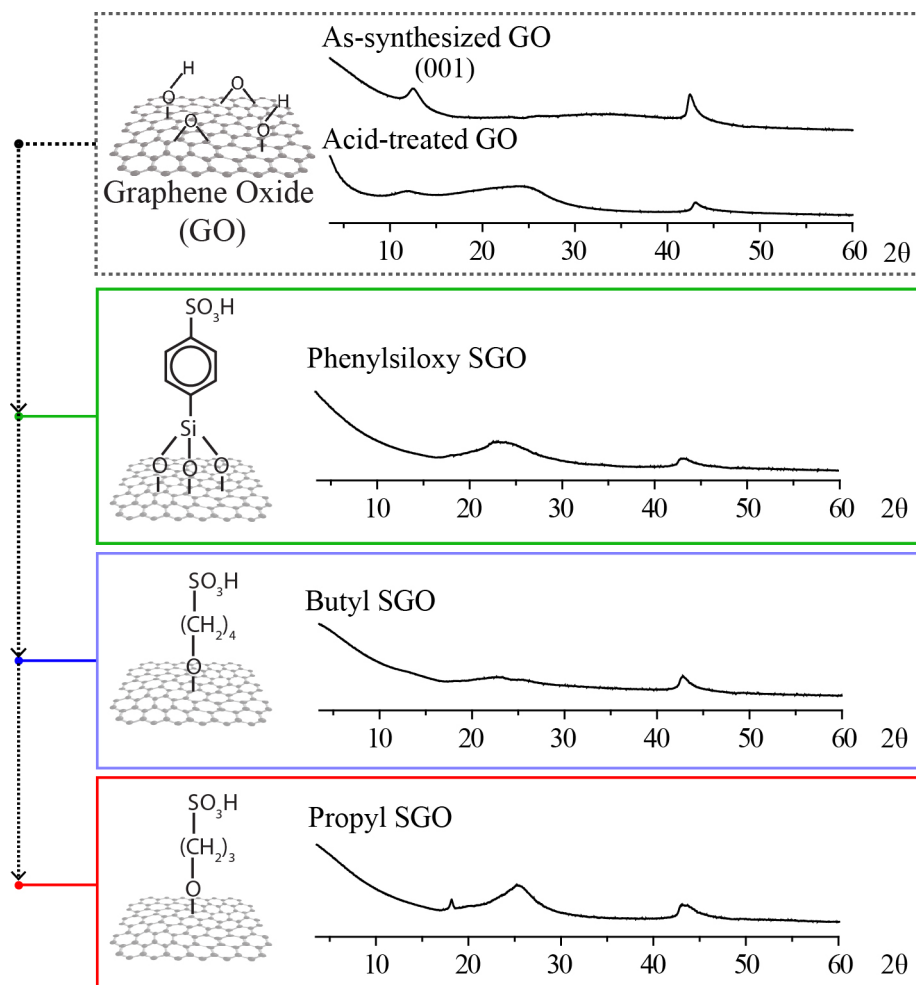


Figure 3.1: Sulfonated graphene oxides derived from GO. Powder XRD for derivatives and acidified GO are shown.

A stock supply of GO was produced from the modified Hummers method of graphite oxidation.^{37, 38} Briefly, graphite powder (4 g) was added to concentrated sulfuric acid (92 mL) and sodium nitrate (2 g) and stirred for several hours. Afterwards, potassium permanganate (12 g) was added to start the oxidation. After 24 hours, the reaction was halted by the addition of hydrogen peroxide (ca. 20 mL, dropwise), and the GO powder product was filtered, washed and dried.

Using this GO as a starting material, the synthesis of a set of sulfonated GOs (SGOs) was performed following modified literature procedures.³⁹ Appropriate amounts of sulfonic acid linker group precursor were added to suspensions of GO (ca. 0.5 g) in

toluene (300 mL) which had been sonicated for 4 hours. 1,3-propanesultone (1.5 g), 1,4-butanedisulfone (1.7 g) and phenyltrimethoxysilane (2.5 g) were used as acid group precursors. A 24 hour reflux period followed. In the case of the phenylsiloxy product, the intermediate formed at this stage was suspended in H₂SO₄ and heated to 80 °C overnight to sulfonate the functional groups. Workup by centrifugation, washing in 50% ethanol/water and drying at less than 100 °C produced the finished SGO samples. Further dehydration, if necessary, was done in a vacuum reactor bomb at 120 °C.

The typical pulse sequences used in this report were the well-described standard Bloch decay, the Hahn-echo and the cross polarization (CP) experiment.⁴⁰ Unless otherwise noted in this report, the ssNMR spectra shown were collected on a Bruker Avance 500 MHz spectrometer with 2.5mm MAS rotors spun at 15 kHz (for ¹H-¹³C CP experiments) or 25 kHz (for ¹H Hahn-echo experiments), or a Bruker Avance 850 MHz spectrometer with 3.2mm MAS rotors spun at 18 kHz (for variable-temperature experiments). The ¹H spectra were referenced to adamantane at 1.85 ppm. The pulses were calibrated to produce a nutation frequency of 62.5 kHz. The ¹³C spectra were referenced to the high-frequency peak in adamantane at 38.5 ppm. The pulses were calibrated to produce a nutation frequency of 62.5 kHz. For ¹H-¹³C CP experiments a contact time of 5 ms was used.⁴¹

The ion exchange capacities (IEC) were probed through back-titration against standardized sodium hydroxide. Samples were dried in vacuo for 16+ hours and then weighed inside a glovebox to avoid adsorption of atmospheric moisture. The samples were then soaked in saturated sodium chloride solution for 24 hours to allow H⁺ - Na⁺ ion exchange. Titration with a standard concentration of sodium hydroxide provided a measure of IEC on a millimolar equivalent per gram (meq/g) basis. Dynamic flash combustion CHNS elemental analysis was performed on washed samples with a Fisons Instruments S.p.A.

EA 1108. Powder X-ray diffraction (p-XRD) was performed using a Bruker D8 Advance diffractometer with a point detector and focused Cu $K\alpha_1$ X-rays. Thermogravimetric analysis (TGA) was performed at a heating rate of 10-20 °C/minute in air using a TA Instruments Q50 thermogravimetric analyzer. Raman spectra were collected with a Renishaw InVia spectrometer with a 514 nm laser.

3.3 Results & Discussion

Bulk characterization of GO, being the starting point of all functionalized materials, is important as it is a complex structure which can vary significantly depending on synthesis method. The IEC of the GO product was 1.512 ± 0.2 meq/g as measured by the titrimetric method. This value is comparable with that noted for other GO paper materials (1.1 meq/g), and is larger than Nafion 117 at similar conditions (0.9 meq/g), indicating that the synthesized GO will serve as a suitable host for functionalization.²⁰ A Raman analysis of the GO and SGO samples revealed two major bands at ca. 1575 and 1350 cm^{-1} , assigned as the G and D bands respectively. The G band results from vibrations in the sp^2 hybridized graphitic sheets while the D band is the result of “defect” sites, or in the present case, sp^3 hybridized sheet carbons attached to functional groups, as has been noted in previous studies.^{42, 43} The D:G band intensity ratios for GO, Propyl SGO, Butyl SGO and Phenylsiloxy SGO were 0.86, 0.89, 0.89 and 0.85, respectively. This negligible change in D:G ratio upon functionalization, when coupled with ^{13}C NMR results (vide infra), indicate a high degree of reaction success, and specifically, a high level of acid functionalization. The distribution of these functional groups is difficult to ascertain, since diffusion in between bonded GO sheets would hamper access to reactive sites.

Table 3.1: Summary of elemental analysis

Sample	C (at%)	H (at%)	S (at%)	S:C
Propyl SGO	67.90	1.77	3.06	0.05
Butyl SGO	65.62	1.81	1.04	0.02
Phenylsiloxy SGO	63.90	1.55	1.55	0.01

Elemental analyses for the functionalized GO samples are summarized in **Table 3.1**. The ratio of carbon to sulfur is used as an initial metric of the degree of functionalization within these materials. Propyl SGO appears to have the highest degree of sulfonation, with a S:C ratio of 0.05. Assuming a uniform distribution of functional groups around the graphene oxide sheet and correcting for the number of carbon atoms within the functional group itself, this corresponds roughly to one sulfonic acid group for every 7.52 carbon atom sheet. Given a similar analysis, the Butyl SGO sample shows a lower S:C ratio of 0.02, corresponding roughly to one functional group per 13^2 carbon atom sheet. The cause of this apparent reduced functionalization is attributed to the relative stability of the 6-membered heterocyclic butanesultone starting material compared to the 5-membered propanesultone. Under the same reaction conditions, a lesser degree of ring opening (and subsequent sheet functionalization) may be expected. The Phenylsiloxy SGO sample shows the lowest level of functionalization, with a S:C ratio of 0.01, or one acid group per 16^2 carbon atom sheet. It is difficult to determine whether this is due to low reaction yield or to the possibility of multiple binding sites for each functional group (see **Figure 3.1**).

3.3.1 Impacts of Functionalization on Sheet Spacing via Powder XRD

Figure 3.1 shows the XRD patterns for GO and functionalized GO samples. The low-angle diffraction peak (ca. $12.5^\circ(2\theta)$) in the GO diffractogram corresponds to the (001) reflection and denotes an interlayer spacing of 7.5 - 8 Å. Such a large spacing is

due to a layer of strongly hydrogen-bonded water molecules positioned between sheets of GO. This spacing is typical of previously published GO p-XRD results.^{44, 45} The breadth of this diffraction peak is correlated to the largely amorphous nature of the GO sheets, resulting in a distribution of interlayer spacing in the sample. This calculated interlayer spacing shows the expected increase when compared to the starting material graphite powder, with an interlayer spacing closer to 3 Å noted in literature.^{46, 47}

To test the effect of the acidic conditions introduced by functionalization, a dummy synthesis was performed where a portion of H₂SO₄ (equimolar to the amount of functional group precursor added in the actual syntheses) was added to GO suspended in toluene and reacted as usual. The X-ray diffraction pattern for this acid treated GO is also shown in **Figure 3.1**. The (001) diffraction peak from the GO starting material has broadened and decreased in intensity, while a new, very broad diffraction peak appears centred about 25° (2θ). The broadness of these reflections indicates a large distribution of interlayer spacing within the sample, caused by the highly disordered and sporadic placement of oxygen functional groups within the sample. The appearance of the higher angle diffraction peak would seem to indicate a significant collapse of interlayer spacing after treatment in acid. This spacing is not sufficiently large to allow for a layer of intercalated water, in contrast to the case of GO itself, and so the acid treatment of GO appears to have reduced the bulk hydrophilicity of the sheets.

The disappearance of the (001) reflection in functionalized samples seen in **Figure 3.1** shows the loss of well-defined inter-sheet spacing, commonly seen in the literature upon graphene and GO functionalization.^{20, 48} Sporadic areas of relatively low stacking order (i.e. only a few layers per stack) in the GO and functionalized GO samples are evidenced by the diffraction at 25° (2θ), while peaks at ca. 19 and 42.5° (2θ) represent graphitic starting material. Differences between the diffractograms of functionalized

GOs are a response to the number and structure of functional groups present in the sample, where the Propyl and Phenylsiloxy SGO samples display more ordered sheet stacking than the Butyl SGO sample signified by the stronger diffraction seen at 25° (2θ). Given the broadness of this peak in all three functionalized samples and under the assumption of uniform functionalization in the graphitic sheets, it would appear the diffraction peak at 25° (2θ) represents the spacing between sheet and functional group carbon atoms, indicating a collapse of inter-sheet spacing upon functionalization.

3.3.2 Evidence of Functional Group Structure by ^1H - ^{13}C NMR

The ^1H - ^{13}C CP spectrum of as-synthesized GO is shown in **Figure 3.2A**. It shows clearly the hydroxy and epoxy functional group carbons as well as the basal sheet sp^2 hybridized carbon signal (ca. 70, 60 and 130 ppm, respectively). This spectrum matches well with published spectra of ^{13}C -labeled GO.^{29, 49} The signals are notably broad, despite the signal enhancement techniques employed in ssNMR: this signal broadness likely is caused by the highly disordered structure of GO. The ^1H - ^{13}C CP spectrum of the acid treated GO product after drying for 48 hours at 75°C in vacuo is also shown in **Figure 3.2A**. The acid treatment removes nearly all of the signal intensity from hydroxy and epoxy functional groups, leaving only the sp^2 hybridized carbon site and a small signal at ca. 20 ppm, indicating a population of alkane-like carbon sites (e.g. methyl or methylene carbons). These results, coupled with the collapsing inter-sheet spacing observed in the XRD data, suggest that in acidic conditions a significant amount of dehydration occurs, removing the hydroxy and epoxy functional groups and forming graphite-like sp^2 hybridized carbon sites. This conversion explains the reduced interlayer spacing, while a small amount of direct alcohol sulfonation (or small regions of isolated, unreacted oxygen functional groups) could cause the broad, GO-like (001)

diffraction peak seen in the XRD and the sp^3 hybridized signal seen in the 1H - ^{13}C CP NMR spectra.

The 1H - ^{13}C CP spectra of as-synthesized GO and SGO samples are shown in **Figure 3.2B**. Under optimal conditions and with a large number of scans, the edge-based functional group carbons within GO can be resolved (enol, ketone, etc., highlighted in the insert). After functionalization to Propyl SGO, the surface hydroxy and epoxy carbon signals almost completely disappear. This is noteworthy as it indicates a nearly complete conversion from GO to Propyl SGO with very few remaining surface oxide groups, and a highly homogeneous surface. The sp^2 carbon peak at ca. 120 ppm is broadened and shifted to low frequency compared to its position in the GO spectrum, indicating an increase in the disorder of the basal carbon sheet. The three small signals found at ca. 60, 38 and 20 ppm represent the three methylene carbons in the propyl chain: one sulfonate-bound, one alkane-like and one ether-bound, respectively. These chemical shifts correlate with previously reported shifts for similar methylene carbons.⁵⁰ Signal intensity in the 70 ppm region can be assigned mainly to sp^3 hybridized ether carbons within the functional groups, although similar sp^3 hybridized ether carbons within the sheet would also appear at this chemical shift. Varying the CP contact time used in these pulse sequences affects the efficiency of 1H - ^{13}C polarization transfer, and at shorter contact times these functional group carbon peaks display an increase in intensity, as expected for the short distance between directly bonded protons and carbons in an alkyl chain.

The Butyl SGO spectrum differs most significantly from the Propyl SGO spectrum in the presence of an intense, sharp peak at ca. 70 ppm. This peak is assigned to a significant population of unreacted hydroxyl groups, and this result matches well with the previously reported lesser degree of functionalization seen in EA (*vide supra*). A

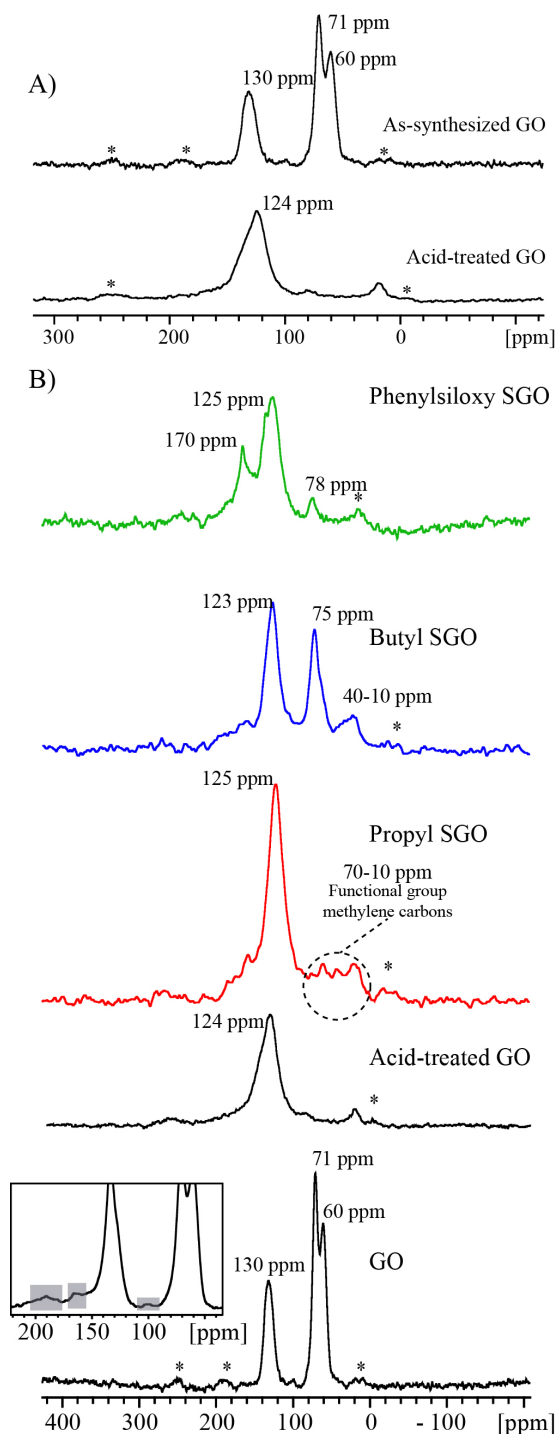


Figure 3.2: A) ^1H - ^{13}C CPMAS spectra of GO before (11.7 T, 15 kHz MAS) and after (7 T, 9.5 kHz MAS) treatment in toluene and H_2SO_4 , mimicking the result of functionalization without the presence of organic functional groups. B) ^1H - ^{13}C CPMAS spectra of GO (11.7 T, 15 kHz MAS), Propyl SGO (7 T, 11 kHz MAS), butyl SGO (7 T, 11 kHz MAS) and Phenylsiloxy SGO (11.7 T, 15 kHz MAS). Higher resolution insert shows the presence of edge-based functional group carbons. * = spinning side bands.

broad peak is seen in the alkyl chain region (ca. 40 ppm) which leans toward the low frequency side. This indicates an increase in the methylene carbon signal intensity, as would be expected when comparing a butyl group (with two methylene carbons) to a propyl group (with only one). This result demonstrates the remarkable utility of NMR in uncovering minute differences in samples, even at low functional group concentration.

The Phenylsiloxy SGO spectrum indicates a higher degree of reaction success than in the Butyl SGO case, with almost completely attenuated signal intensity in the 70–60 ppm range. The small peak at ca. 70 ppm can be assigned to in-sheet sp^3 hybridized ether carbons as in the Propyl SGO spectrum. Coupled with the relatively low level of functionalization seen through EA, this indicates that each phenylsiloxy group is likely attached to the graphitic sheet through more than one of its ether moieties. A broad peak at 170 ppm represents the aryl ring carbons in the acid group linker. The non-Gaussian shape of this feature indicates a large degree of heterogeneity with respect to chemical shift and mobility within the functional group carbon atoms.

These spectra provide direct evidence of the functional groups of two novel functionalized graphene samples, both of which may prove useful in the improvement of hydrogen fuel cell electrolyte membrane proton conductivity. In addition, the functional group carbons of Propyl SGO, a material which has been used successfully in the improvement of fuel cell performance (referenced above) have been resolved through 1H - ^{13}C CP NMR. Functionalization of GO causes the conversion of oxygen-based functional groups into anchor points for the acidic alkyl chains. These acid groups are then able to catalyze the dehydration of remaining hydroxy or epoxy functional groups, provided that the functionalization was sufficiently successful as is the case in Propyl SGO. With less successful functionalization (e.g. in Butyl and Phenylsiloxy SGO) some oxygen functional groups are left unconverted. In both cases, functionalization causes a collapse of inter-

layer spacing and an overall increase in sheet stacking disorder as shown by XRD. A schematic of these materials is shown in **Figure 3.3**.

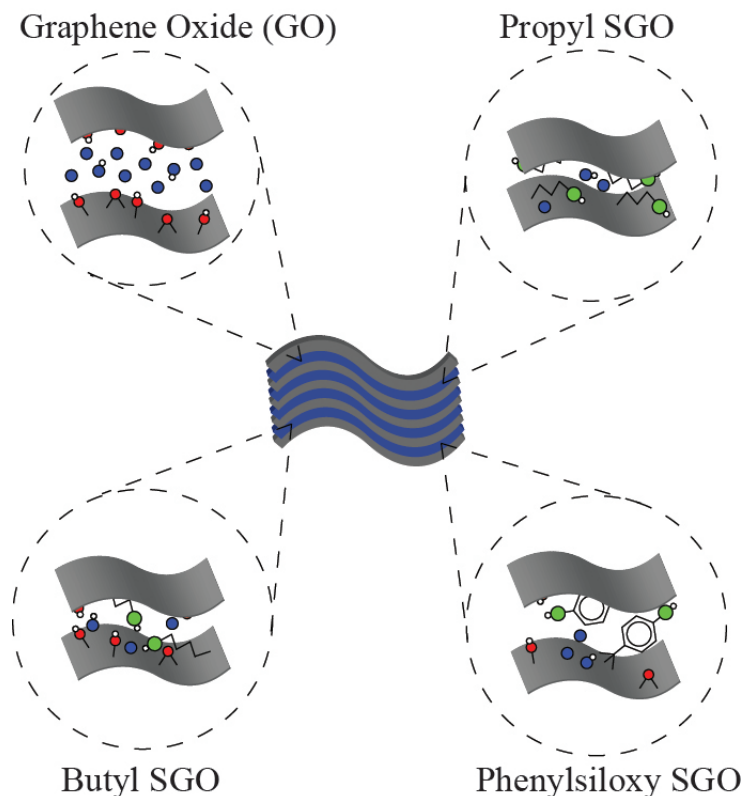


Figure 3.3: Diagram of functionalization of GO samples, showing collapse of interlayer spacing upon acid functionalization (blue circles represent H_2O molecules, red circles represent oxygen in surface functional groups, green circles represent sulfonic acid groups, and white circles represent ionizable protons).

3.3.3 Thermal Analysis of Functionalized SGO Stability

Figure 3.4 displays TGA curves for the as-synthesized GO as well as functionalized GO samples. The curves show 3 main weight losses when heated in air. In order from low to high temperature, the first is due to evaporation of adsorbed water, the second is due to loss of oxygen-based functional groups, and the third is due to loss of the sheet carbons through oxidation to CO_2 .⁵¹ The loss due to water occurs at higher temperatures in the functionalized samples compared to GO, especially for the Propyl and Phenylsiloxy SGOs, indicating an increase in bulk hydrophilicity. Functionalization

also appears to destabilize the carbon sheet, as degradation to CO₂ occurs at a lower onset temperature (from 10 to 100 °C lower) in all functionalized cases as compared to the bare GO. The functional group in the Phenylsiloxy SGO sample is more thermally stable than those in the Butyl SGO, displaying a more gradual loss of mass between 200 and 350 °C. Residual mass after high temperature treatment can be noted for the Phenylsiloxy SGO sample, and is attributed to remaining silica (assuming that all silica came from linker groups, and that the functionalization reaction went to completion, this mass indicates that the Phenylsiloxy SGO had 1.67×10^{-2} moles of functional groups per gram of sample). Between the SGO samples, it appears that sheet thermal stability matches with functionalization success (defined as the disappearance of hydroxy and epoxy group signals from ¹H-¹³C CP NMR spectra). This is particularly evident for Butyl SGO, where TGA mass losses are sharper and occur at lower temperature, and which has the highest leftover ¹H-¹³C CP signal intensity.

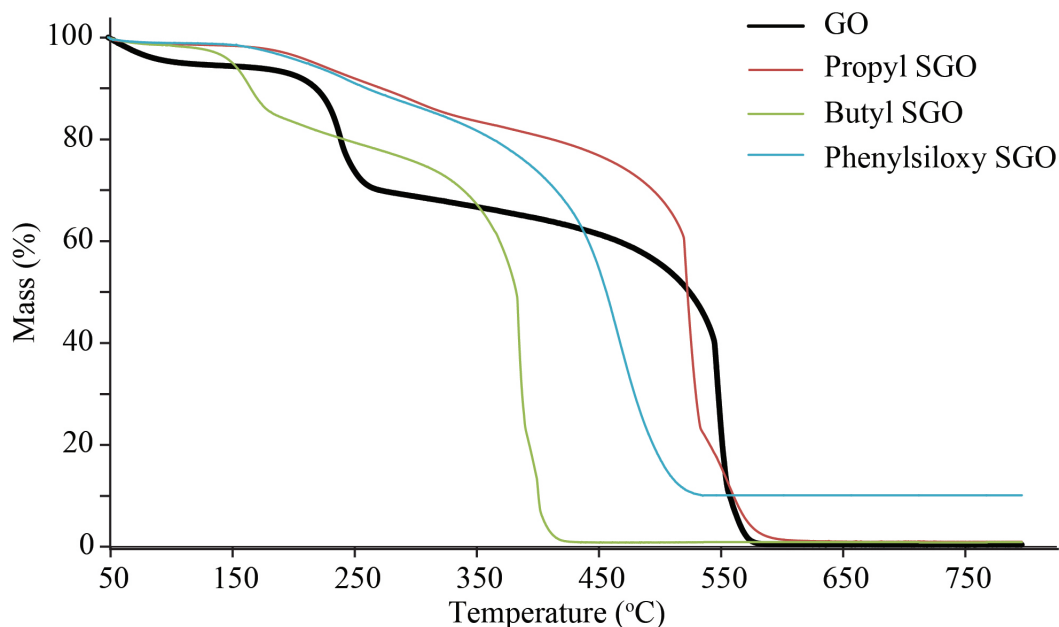


Figure 3.4: TGA curves for GO and SGOs (ramp to 800 °C in air).

3.3.4 Evaluation of Local Mobility and Exchange by ^1H & ^2H ssNMR

Figure 3.5 shows ^1H and ^2H (referenced to D_2O) spectra of Propyl SGO as it responds to post-synthesis treatments. The spectrum for the as-synthesized sample is broad and featureless. Although chemically one might expect to see protons from the functional group (an acidic proton as well as three methylene proton sites), possibly in addition to some leftover hydroxy protons from unreacted GO functional groups, it appears that these signals are buried underneath the rigid water signal. After 96 hours of dehydration at $140\text{ }^\circ\text{C}$ in vacuo, the strong water signal is substantially attenuated, revealing a high frequency narrow peak due to acidic protons. The lower frequency broad peak may be caused by strongly bound intercalated water, still obscuring the methylene protons in the functional groups, or alternatively the methylene protons, themselves rigidly held in the heterogeneous local environment of the SGO. Purposeful rehydration of the sample by soaking in deionized water caused the bulk water signal to return, which then caused the acid site to appear as a high frequency shoulder off the main peak.

Intriguingly, exchange of the acid proton site with deuterium proved to be very difficult. **Figure 3.5** shows ^2H spectra of Propyl SGO which had been refluxed in D_2O or treated in 1M DCl , and the amount of signal observed for each spectrum is extremely low compared to the proton spectra. In the case of the refluxed sample, the deuterons seem to preferentially occupy the acid proton-mobile water site, based on their chemical shift. However, considering the low signal-to-noise ratio, these deuterations were practically unsuccessful. This may be a result of poor access to acidic sites other than those on the surfaces of SGO sheet stacks, or possibly a result of poor functionalization.

^1H variable temperature spectra were collected in order to discover any proton dynamics within these materials. The spectra collected for GO and Propyl SGO are shown

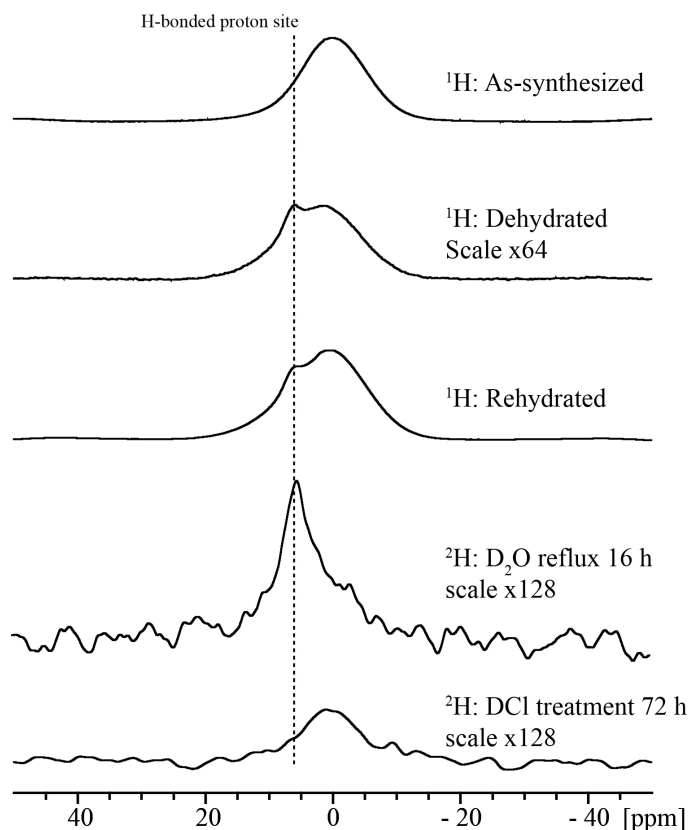


Figure 3.5: ^1H and ^2H spectra (25 kHz MAS) of Propyl SGO after post-synthesis dehydration, rehydration and deuteration. 1024 transients were collected for each spectrum (scaling factors are noted). Reduced intensity of the deuterium spectra indicates poor deuterium (and therefore, proton) exchange, despite acidic and high temperature conditions.

in **Figure 3.6**. Higher rates of MAS were employed to minimize homonuclear dipolar coupling and a background suppressing Hahn-echo was used to minimize the appearance of any signals caused by non-sample protons within the probe. The GO peak is relatively narrow, and at higher temperatures gets slightly narrower. No change in chemical shift is observed as there are no exchange processes activating at heightened temperatures (i.e. no acidic protons). The Propyl SGO is significantly broader than that for GO, possibly due to the heightened disorder in the functionalized sample. Signals caused by the variety of proton sites within this sample (e.g. acidic proton, alkyl group) were not readily resolvable from these experiments. At increasing temperature, the signal attenuates significantly, most likely indicating dehydration of the sample. The signal

also shifts slightly to higher frequency; this is likely caused by changes in ring current shift as the material dehydrates and contracts at increasing temperature. An increase in proton exchange rate between acid groups and bulk water has been reported in the past to cause a shift to lower frequency as the protons spend more and more time in the bulk water-like phase. Given that the shift here is in the opposite direction, that process is not likely the cause of the minor chemical shift change seen here. These results also contrast sharply with proton spectra collected for Nafion (taken as an example of a highly proton conductive material) at higher temperature, which displays a very narrow peak for the acidic proton / bulk water signal.⁵²

This investigation points toward a rigid, strongly-bound intercalated layer of water existing between layers of Propyl SGO. This is supported by the collapse of interlayer spacing seen upon functionalization in the XRD. It would seem unlikely that the functional groups within this material would be able to contribute to the proton conductivity of any PEM, being that it holds its acidic functional groups within such a rigid layer of water. Similar behavior is noted in the novel Butyl and Phenylsiloxo SGO, suggesting that this trend is due to bulk properties rather than the molecular structure of the functional groups. This surprising new data provides useful insight into the process of intelligent functionalization of GO for use as a proton conductivity enhancer. It is therefore suggested that the previously observed increase in bulk proton conductivity caused by this material is due primarily to functional groups located on the surfaces and edges of functionalized GO stacks, and that intercalated functional groups are unnecessary for the improvement of proton dynamics for increased conductivity. It is recommended that further studies into PEM/GO composites are focused on well-dispersed functionalized GO additives which resist sheet stacking, or increase surface area of dopant GO derivatives, in order to improve the efficiency of proton conducting acidic sites.

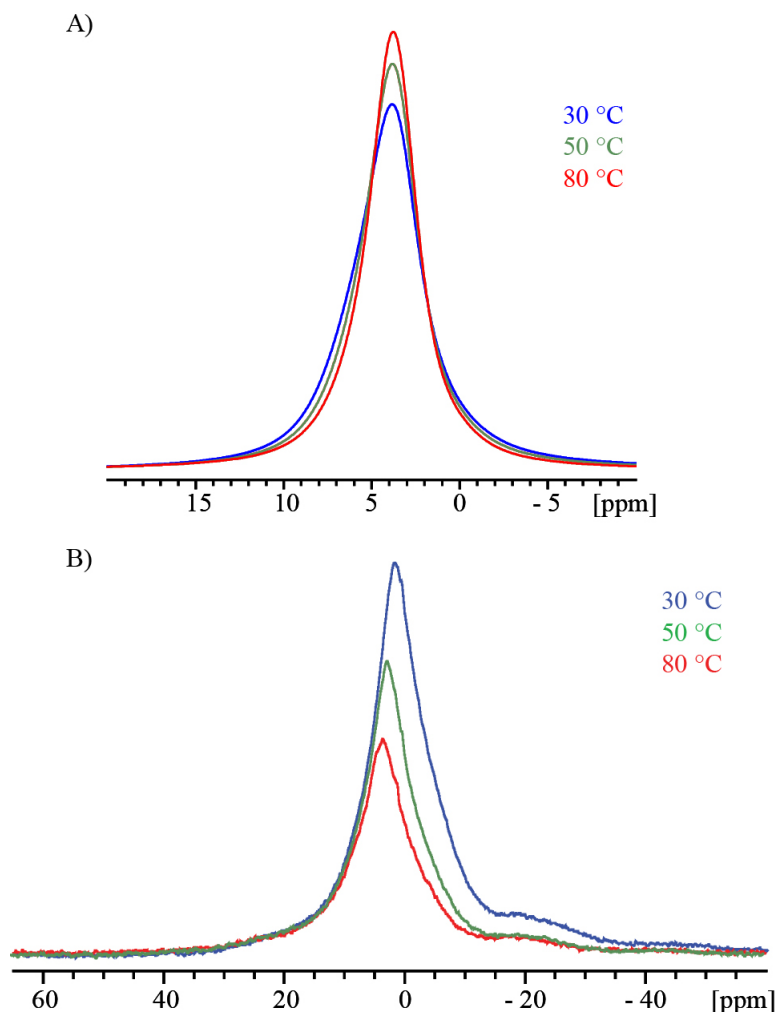


Figure 3.6: ^1H VT spectra of A) GO (25 kHz MAS at 11.7 T) and B) Propyl SGO (18 kHz MAS at 20 T). Minimal chemical shift changes are seen at high temperature, implying poor proton conductivity.

3.4 Conclusions

Functionalized GO samples (including two novel materials) with different organic linkers between the graphene sheet and sulfonic acid groups were successfully synthesized. These materials produced XRD, Raman, EA and TGA data consistent with previously published data regarding similar materials. ^1H - ^{13}C CPMAS spectra were able to clearly identify unique functional groups in the GO precursor, the previously synthesized Propyl SGO and the novel butyl SGO and Phenylsiloxy SGO. The unexpected level of sensitivity seen in these spectra allows for the resolution of separate carbon sites

within these functional groups. It is proposed that the attached acidic functional groups catalyze the dehydration of remaining oxygen-based GO functional groups, resulting in a uniform product where functionalization success is high. Dehydration and deuteration experiments indicate that the water within Propyl SGO is held extremely rigidly, and exchange with intercalated acidic sites is highly infrequent. This would seem to indicate that only the functional groups based on the surface of SGO stacks are responsible for the increase in proton conductivity reported in composites of PEM polymers and GO / Propyl SGO. It is suggested that the prevention of sheet stacking in composites will result in further increases in proton conductivity. A thorough solid-state NMR method of analysis is presented which can distinguish between functionalized, nanostructured carbons samples based on individual carbon atoms in their functional groups with high sensitivity. These results not only prove the utility of ssNMR in studying these non-trivial samples, but provide an important starting point for the use of ssNMR in studying polymer-SGO composites (i.e. for PEM-FC applications) in the future.

References

- [1] Dyer, C. K. *J. Power Sources* **2002**, *106*(1), 31–34.
- [2] Pollet, B. G.; Staffell, I.; Shang, J. L. *Electrochim. Acta* **2012**, *84*(1), 235–249.
- [3] Thomas, C. *Int. J. Hydrogen Energy* **2009**, *34*(15), 6005–6020.
- [4] Carrette, L.; Friedrich, K. A.; Stimming, U. *ChemPhysChem* **2000**, (1), 162–193.
- [5] Carrette, L.; Friedrich, K.; Stimming, U. *Fuel Cells* **2001**, *1*(1), 5–39.
- [6] Luduena, G. A.; Kuhne, T. D.; Sebastiani, D. *Chem. Mater.* **2011**, *23*(6), 1424–1429.
- [7] Wojnarowska, Z.; Wang, Y.; Paluch, K. J.; Sokolov, A. P.; Paluch, M. *Phys. Chem. Chem. Phys.* **2014**, *16*(19), 9123–9127.
- [8] Ogawa, T.; Kamiguchi, K.; Tamaki, T.; Imai, H.; Yamaguchi, T. *Anal. Chem.* **2014**, *86*(19), 9362–9366.
- [9] Pivovar, B. S. *Polymer* **2006**, *47*(11), 4194–4202.
- [10] Yamada, M.; Honma, I. *Electrochim. Acta* **2003**, *48*(17), 2411–2415.
- [11] Mauritz, K. A.; Moore, R. B. *Chem. Rev.* **2004**, *104*(10), 4535–4586.
- [12] Sone, Y.; Ekdunge, P.; Simonsson, D. *J. Electrochem. Soc.* **1996**, *143*(4), 1254–1259.
- [13] Cappadonia, M.; Erning, J. W.; Niaki, S. M. S.; Stimming, U. *Solid State Ionics* **1995**, *77*, 65–69.
- [14] Dang, Q. K.; Henkensmeier, D.; Krishnan, N. N.; Jang, J. H.; Kim, H.-J.; Nam, S. W.; Lim, T.-H. *J. Memb. Sci.* **2014**, *460*, 199–205.
- [15] Davis, E. M.; Stafford, C. M.; Page, K. A. *ACS Macro Lett.* **2014**, *3*(10), 1029–1035.
- [16] Tseng, C.-Y.; Ye, Y.-S.; Cheng, M.-Y.; Kao, K.-Y.; Shen, W.-C.; Rick, J.; Chen, J.-C.; Hwang, B.-J. *Adv. Ener. Mat.* **2011**, *1*(6), 1220–1224.
- [17] Zarrin, H.; Higgins, D.; Jun, Y.; Chen, Z.; Fowler, M. *J. Phys. Chem. C* **2011**, *115*(42), 20774–20781.
- [18] Mishra, A. K.; Kim, N. H.; Jung, D.; Lee, J. H. *J. Memb. Sci.* **2014**, *458*, 128–135.
- [19] Kumar, R.; Mamlouk, M.; Scott, K. *Int. J. Electrochem.* **2011**, *2011*.
- [20] Scott, K.; others. *Chem. Comm.* **2012**, *48*(45), 5584–5586.
- [21] Tateishi, H.; Hatakeyama, K.; Ogata, C.; Gezuhara, K.; Kuroda, J.; Funatsu, A.; Koinuma, M.; Taniguchi, T.; Hayami, S.; Matsumoto, Y. *J. Electrochem. Soc.* **2013**, *160*(11), F1175–F1178.

- [22] Cao, Y.-C.; Xu, C.; Wu, X.; Wang, X.; Xing, L.; Scott, K. *J. Power Sourc.* **2011**, *196*(20), 8377–8382.
- [23] Jiang, Z.; Zhao, X.; Manthiram, A. *Int. J. Hydrogen Energ.* **2013**, *38*(14), 5875–5884.
- [24] He, Y.; Tong, C.; Geng, L.; Liu, L.; Lü, C. *J. Memb. Sci.* **2014**, *458*, 36–46.
- [25] Yuan, T.; Pu, L.; Huang, Q.; Zhang, H.; Li, X.; Yang, H. *Electrochim. Acta* **2014**, *117*, 393–397.
- [26] Yan, Z. B.; De Almeida, N. E.; Traer, J. W.; Goward, G. R. *Phys. Chem. Chem. Phys.* **2013**, *15*(41), 17983–17992.
- [27] Ye, G.; Hayden, C.; Goward, G. *Macromolecules* **2007**, *40*(5), 1529–1537.
- [28] De Almeida, N. E.; Goward, G. *J. Power Sourc.* **2014**, *268*, 853–860.
- [29] Cai, W.; Piner, R. D.; Stadermann, F. J.; Park, S.; Shaibat, M. A.; Ishii, Y.; Yang, D.; Velamakanni, A.; An, S. J.; Stoller, M. *Science* **2008**, *321*(5897), 1815–1817.
- [30] Fang, X.; Mao, J.; Levin, E. M.; Schmidt-Rohr, K. *J. Am. Chem. Soc.* **2009**, *131*(4), 1426–1435.
- [31] Brown, S. P.; Spiess, H. W. *Chem. Rev.* **2001**, *101*(12), 4125–4156.
- [32] Schmidt, J.; Hoffmann, A.; Spiess, H. W.; Sebastiani, D. *J. Phys. Chem. B* **2006**, *110*(46), 23204–23210.
- [33] Grünberg, B.; Emmler, T.; Gedat, E.; Shenderovich, I.; Findenegg, G. H.; Limbach, H.-H.; Buntkowsky, G. *Chem. Euro. J.* **2004**, *10*(22), 5689–5696.
- [34] Faure, M.; Pallandre, A.; Chebil, S.; Le Potier, I.; Taverna, M.; Tribollet, B.; Deslouis, C.; Haghiri-Gosnet, A.-M.; Gamby, J. *Lab Chip* **2014**, *14*(15), 2800–2805.
- [35] Fiset, E.; Bae, J.-S.; Rufford, T. E.; Bhatia, S.; Lu, G. Q.; Hulicova-Jurcakova, D. *J. Sol. State. Electrochem.* **2014**, *18*(3), 703–711.
- [36] Shao, Y.; Wang, J.; Wu, H.; Liu, J.; Aksay, I. A.; Lin, Y. *Electroanalysis* **2010**, *22*(10), 1027–1036.
- [37] Hummers Jr, W. S.; Offeman, R. E. *J. Am. Chem. Soc.* **1958**, *80*(6), 1339–1339.
- [38] Li, X.; Meng, X.; Liu, J.; Geng, D.; Zhang, Y.; Banis, M. N.; Li, Y.; Yang, J.; Li, R.; Sun, X.; others. *Adv. Funct. Mater.* **2012**, *22*(8), 1647–1654.
- [39] Wang, Y.; Yang, D.; Zheng, X.; Jiang, Z.; Li, J. *J. Power Sourc.* **2008**, *183*(2), 454–463.
- [40] Duer, M. J. *Solid State NMR Spectroscopy: Principles and Applications*; John Wiley & Sons, **2008**.
- [41] Hayashi, S.; Hayamizu, K. *Bull. Chem. Soc. Jpn.* **1991**, *64*(2), 688–690.

- [42] Das, A.; Chakraborty, B.; Sood, A. *Bull. Mater. Sci.* **2008**, *31*(3), 579–584.
- [43] Zhao, G.; Jiang, L.; He, Y.; Li, J.; Dong, H.; Wang, X.; Hu, W. *Adv. Mater.* **2011**, *23*(34), 3959–3963.
- [44] Dikin, D. A.; Stankovich, S.; Zimney, E. J.; Piner, R. D.; Dommett, G. H.; Evmenenko, G.; Nguyen, S. T.; Ruoff, R. S. *Nature* **2007**, *448*(7152), 457–460.
- [45] Marcano, D. C.; Kosynkin, D. V.; Berlin, J. M.; Sinitskii, A.; Sun, Z.; Slesarev, A.; Alemany, L. B.; Lu, W.; Tour, J. M. *ACS Nano* **2010**, *8*(4), 4806–4818.
- [46] Wang, G.; Yang, J.; Park, J.; Gou, X.; Wang, B.; Liu, H.; Yao, J. *J. Phys. Chem. C* **2008**, *112*(22), 8192–8195.
- [47] Bissessur, R.; Liu, P. K.; Scully, S. F. *Synth. Metals* **2006**, *156*(16), 1023–1027.
- [48] Shao, G.; Lu, Y.; Wu, F.; Yang, C.; Zeng, F.; Wu, Q. *J. Mater. Sci.* **2012**, *47*(10), 4400–4409.
- [49] Gao, W.; Alemany, L. B.; Ci, L.; Ajayan, P. M. *Nature Chem.* **2009**, *1*(5), 403–408.
- [50] Freeman, F.; Angeletakis, C. N. *Org. Magn. Res.* **1983**, *21*(2), 86–93.
- [51] Enotiadis, A.; Angjeli, K.; Baldino, N.; Nicotera, I.; Gournis, D. *Small* **2012**, *8*(21), 3338–3349.
- [52] Ye, G.; Janzen, N.; Goward, G. *Macromolecules* **2006**, *39*(9), 3283–3290.

4 — Phosphorus and Nitrogen Centers in Doped Graphene and CNTs Analyzed Through Solid-State NMR

This chapter is a reformatted version of an article submitted for publication in *The Journal of Physical Chemistry C* (MacIntosh, A.R., Jiang, G., Zamani, P., Song, Z., Riese, A., Harris, K.J., Fu, X., Chen, Z., Sun, X. and Goward, G.R., **2018**, 122(12), 6593-6601). The co-authors were Gaopeng Jiang, Pouyan Zamani, Zhongxin Song, Adam Reise, Kristopher Harris, Xiaogang Fu, Zhongwei Chen, Andy Sun, and Gillian Goward. The author was responsible for the characterization of all samples as well as the preparation of the manuscript, except for the experimental synthesis sections. Gaopeng Jiang, Pouyan Zamani, and Xiaogang Fu were responsible for the synthesis and electron spectro-microscopy of the graphitic samples (supervised by Zhongwei Chen). Zhongxin Song and Adam Reise were responsible for the synthesis and electron spectro-microscopy of the nanotube samples, as well as the (supervised by Andy Sun). ^{15}N -labeled nitrogen doped graphene synthesized as reported here was found to contain mainly graphitic nitrogen sites located on the edges of sheets and around defect sites. ^1H - ^1H and ^1H - ^{15}N correlations were also used to probe dopant nitrogen sites in labeled and unlabeled N-doped graphene. A nearly homogeneous population of phosphorus in P-doped graphene was found, with an overwhelming majority of graphitic phosphorus and a small amount of phosphate oligomer. Similar findings were noted for the phosphorus sites in phosphorus and nitrogen co-doped CNTs with a minor change in chemical shift, as would be

expected from two chemically similar phosphorus sites in carbon allotropes (nanotubes versus graphene sheets) with significantly different electronic band gaps.

4.1 Introduction

Fuel cells and high-density batteries have been under intense investigation in recent years, and are well-positioned to become ubiquitous in the auto transportation, aviation and bulk power-storage industries. When fuelled or charged with energy from a green, renewable source, these devices represent half of the solution to the world's energy problem, the other half being the collection of energy from renewable sources (solar, geothermal, wind, tidal, etc.).¹⁻⁵ An unfortunate drawback of these devices is the necessity of precious metals (commonly platinum, iridium and palladium) in order to catalyze the electrochemical reactions to convert chemical energy from hydrogen into electricity. Even with the increasingly present economic and political impetus for new energy storage and distribution systems, these devices would benefit greatly from seeing a reduced or removed dependence on precious metals.⁶⁻¹⁰ The use of doped graphitic materials (i.e. graphene, carbon nanotubes (CNTs)) has been shown in recent publications to reduce dependence on precious metals for catalysis. Doped carbons can be used as metal-free catalysts toward the oxygen reduction reaction (ORR), and exhibit outstanding catalytic activity and durability in alkaline media.¹¹⁻¹⁴ Both nitrogen and phosphorus doped carbons have been used as metal-free catalysts. Significant differences in electrochemical activity are found between doped and undoped carbons which has been attributed to changes in the electronic band structure of these materials brought on by doping, despite loading levels of as little as 0.5% by weight.¹⁵⁻¹⁸ While the bulk electrochemical and physical properties of doped carbon materials are relatively simple

to study, the non-stoichiometric and poorly ordered nature of these structures make the collection of meaningful data on the micro to nanoscopic scale challenging. To understand the nature of these doped carbon materials, a clear picture of the chemical environment around dopant sites must be drawn, and so a structural analysis method with high resolution and high specificity is necessary. Most structural analyses of these materials are based on X-ray spectro-microscopies, particularly energy-dispersive X-ray (EDX) spectroscopy, and electron microscopy. Scanning and transmission electron microscopy (SEM and TEM) can be used to get an idea of any bulk morphological changes doping may have on sheets and tubes, and EDX can provide surface elemental composition with micron-level spatial resolution, but even with these data in hand it can be difficult to link structure and function in these materials in a chemically meaningful way. Solid-state nuclear magnetic resonance (ssNMR) spectroscopy is an ideal analysis method due to its extreme sensitivity toward slight changes in chemical environment. Significant analytical work has been done on nonconductive carbons, but a relatively small amount has been applied to conductive and/or doped carbon samples. Some of the earliest ssNMR work done on amorphous carbons was done to investigate which of the many potential models of graphene was correct. This study required careful thin film deposition of carbon with isotopically labelled precursors, however resolution between graphitic and other carbon sites was obtained, and a clearer picture of the structure of graphene was developed.¹⁹ Ishii et al. synthesized graphene oxide through chemical vapour deposition using ^{13}C labelled methane, and were able to collect 2D ^1H - ^{13}C correlation spectra in reasonable experimental time, which unambiguously solved the debated structure of graphene oxide.²⁰ Leskes et al. have built a body of work applying ssNMR techniques to conductive and doped carbon materials, both ex and in situ, for use in battery and supercapacitor systems, recently using isotopic labelling and dynamic

nuclear polarization enhancement to selectively study the solid-electrolyte interface at the surface of graphitic current collectors.²¹⁻²³ In previous work, various ^1H , ^2H , and ^{13}C techniques were used to characterize acidic functional groups covalently attached to graphene with unprecedented resolution; the recorded spectra even showed appreciable resolution between carbon atoms in a functional group aliphatic chain.²⁴ In addition, the surfaces of the graphene-like MXene family of layered metallic materials were successfully characterized through ssNMR, even probing the interactions between surface hydroxide and fluoride sites.²⁵ In a separate study, the carbon spectra of a graphene nanosheet coated with tin-graphite core-shell nanoparticles was found to be extremely sensitive to carbon density, and respond to changes as the anode carbon was reduced during discharge. This ssNMR information was produced from a tiny amount of sample thanks to the use of signal-enhancing magic angle spinning along with long, rotor-synchronized pulse trains.²⁶ However, the amorphous and inhomogeneous nature of these samples tends to produce crowded, difficult-to-acquire spectra with overlapping broad signals. Furthermore, the electronic conductivity of these materials leads to a magnetically induced current within the sample which, in turn, produces a non-negligible magnetic field. The interaction of this field with the applied field can cause issues with the physical acquisition of data and can make the collection of interpretable spectra yet more challenging. As a result, part of the work described here is NMR method development, whereas the ultimate goal of this line of study is to unambiguously link catalyst stabilization or catalytic performance to specific structures, leading to the selective tuning of the electronic properties of these fascinating materials.²⁷⁻²⁹ In this work, the ssNMR analysis of a number of doped carbon materials are described: nitrogen doped graphene, phosphorus doped graphene and CNTs co-doped with both phosphorus and nitrogen. ssNMR has been used successfully to analyze graphene and other amorphous carbons,

however this study will use this tool to focus on dopant sites specifically. These samples were synthesized with varying methods and precursor materials, both with and without isotopic labelling. The results shown here elucidate the chemical environments around dopant sites in graphene and CNTs, leading to a deeper understanding of the function of these materials in energy storage and delivery media. ssNMR is shown to be a useful tool in the analysis of novel carbon allotropes, and can provide important chemical information that is inaccessible through the usual means of SEM and EDX. The samples studied in this work were i) two closely related phosphorus doped graphenes, one with a significant presence of oxygen (PG and PG-O), ii) nitrogen doped graphene (NG) and iii) phosphorus / nitrogen co-doped carbon nanotubes (PNCNTs), synthesized by a variety of methods.

4.2 Experimental

4.2.1 Synthesis: Doped Graphenes (PG, PG-O, NG)

GO was synthesized according to the improved Hummers method from natural graphite flakes.³⁰ First, 98% H₂SO₄ (360 mL) and 85% H₃PO₄ (40 mL) were mixed carefully in a round-bottom flask in an ice bath. Graphite powder (2 g) was added into the concentrated mixed acid and stirred for 1 h. Then, the strong oxidizing agent KMnO₄ (18 g) was added slowly into the mixture, and the oxidation reaction was kept at 50 °C for 16 h. After cooling down the mixture, the oxidation reaction was terminated. Distilled deionized (DDI) water (400 mL) and 20 mL H₂O₂ (20 mL) were added dropwise and then stirred for 30 min. Afterward, the mixture was centrifuged and washed with DDI water, 5% HCl, and ethanol. Finally, the GO nanosheets were obtained by freeze-drying the GO suspension. To convert GO into phosphorus doped graphene (PG),

typically 300 mg of triphenyl phosphine was first dissolved in 100 mL isopropyl alcohol (IPA) at ambient temperature. Then, freeze-dried GO powder (60 mg) was added to the solution and the mixture was dispersed by sonication for 2 hours. After the color of suspension changed to dark grey, the mixture was transferred onto a hot plate and IPA was evaporated overnight. The obtained solid was ground and placed in an alumina boat. Then the mixture underwent heat treatment to 1000 °C with a ramp of 10 °C min⁻¹ under an atmosphere of Ar. The temperature was maintained at 1000 °C for 30 min under Ar and another 30 min under 10% H₂/Ar. PG was collected after this treatment.

A second sample, synthesized via the same method as noted above but with the final heating done in a pure Ar atmosphere (i.e., without H₂ gas), produced a PG with significantly higher amounts of oxygen than in the original synthesis. This oxygen-rich phosphorus doped graphene will be referred to as PG-O.

For NG, a synthesis based on the pyrolysis of polyaniline was employed. ¹⁵N-labelled aniline (3 g), iron (III) chloride (FeCl₃, 30 mg), ammonium peroxydisulfate (APS, 6.8 g) and a carbon source (CNTs, 400 mg) were added sequentially to a hydrochloric acid solution. These components in solution acted as a nitrogen source precursor, catalyst, oxidizer and carbon source, respectively. The mixtures were vigorously stirred at room temperature for 48 h to allow full polymerization of the aniline into polyaniline. After two days, the liquid was evaporated, and the solid polymer was assembled. This precursor was then pyrolyzed at 200 °C and later at 900 °C for 1 h using a 30 °C min⁻¹ heating rate under an argon atmosphere. The solid carbonized materials were then leached in sulfuric acid at 80 - 90 °C to remove the remaining iron complexes as well as to introduce porosity. After this leaching step, the material was heat-treated at 900 °C in argon for

3 h. At this point the sample is referred to as NG. Where noted, treatment in ammonia gas was then performed at 900 °C for 15 minutes.

4.2.2 Synthesis: Doped Carbon Nanotubes (PNCNTs)

PNCNTs were prepared via the floating-catalyst CVD method using ferrocene (98%, Aldrich) as the catalyst with triphenyl-phosphine (TPP) (99%, Sigma) and imidazole (99%, Sigma) as the P and N sources, respectively. Both precursors also provided the carbon for CNT growth. A mixture of imidazole and 2.5wt.% TPP (2 g total) was placed in a small quartz crucible. 20 mg of ferrocene was placed in a small holder, separate from the precursors, on the quartz crucible. A substrate alumina crucible was placed in the center of a quartz tube in a tube furnace. The precursor and catalyst crucibles were placed near the opening of the furnace and Ar gas was flowed through the tube for 20 minutes to remove air. The temperature was raised to 850 °C, at which point the ferrocene and the precursors were evaporated and transferred to the substrate by the Ar flow. The substrates were kept at the set temperature for 10 minutes and then cooled to ambient temperature under Ar.

4.2.3 Characterization

The morphology and surface elemental analysis of PG and NG samples were examined by SEM (LEO 1530) and XPS (Thermo Scientific, Al K-Alpha X-ray source). The morphology and structure of the PNCNTs were studied using a Hitachi S-4800 field-emission SEM and a JEOL 2010F TEM. Chemical compositions of PNCNTs were investigated by X-ray photoelectron spectroscopy using a Kratos Axis Ultra-spectrometer. XPS data was interpreted using the NIST X-ray Photoelectron Spectroscopy Database.³¹ A summary of these elemental analyses can be found in **Table 4.1**.

Table 4.1: Summary of elemental analyses via XPS survey scan.

Sample	C(at%)	N(at%)	O(at%)	P(at%)
PG	98.74	-	0.03	1.26
PG-O	96.01	-	3.39	0.60
NG	91.40	4.07	4026	-
PNCNTs	88.7	6.2	3.8	1.1

ssNMR spectra were collected on Bruker Avance 300, 500 and 850 MHz spectrometers using 1.9, 2.5 or 4 mm MAS rotors. Where samples were conductive enough to cause difficulty with spinning the rotors or tuning/matching the probe, dilution with Teflon powder was used (up to 5:1 by mass of Teflon : sample). ^1H and ^{13}C spectra were referenced to adamantane at 1.85 ppm and 38.5 ppm (high-frequency peak), respectively. ^{31}P spectra were referenced to 1 M phosphoric acid at 1 ppm, and ^{15}N spectra were referenced to glycine-HCl at 33.9 ppm (in the unified ^{15}N chemical shift scale proposed by Bertani et al.).³² Typically, hard pulses were calibrated to produce a nutation frequency of 62.5 kHz, and where necessary, 50 kHz of ^1H decoupling was applied. ^1H - ^{15}N CP experiments optimized for signal intensity used a contact time of 3 ms. ^1H - ^{15}N D-HMQC experiments used a recoupling time of 200 μs . Typical recycle delays for these experiments were 4 s for ^1H , 10 s for ^{15}N and 2 s for ^{31}P , however delays ranging from 0.2 to 500 s were used to identify species with unusual relaxation times.

4.3 Results & Discussion

4.3.1 Phosphorus-doped Graphene (PG and PG-O)

Both PG and PG-O demonstrate a typical graphitic sheet-like morphology in the SEM images seen in **Figure 4.1**. EDX analysis does not show a detectable presence of oxygen in PG, and shows that more phosphorus atoms are present in PG compared to PG-O as is seen in **Table 4.1**. High resolution XPS spectra of the P 2p edge for

both these samples are shown in **Figure 4.2**. These spectra have a markedly low signal-to-noise ratio, likely due to the low level of elemental doping in these samples. Given the poor signal intensity and resolution, there is significant uncertainty in the binding energies and relative amounts of each species, but a tentative signal assignment is as follows: elemental phosphorous (ca. 129.6 eV), graphitic phosphorous (ca. 131 eV) and oxidized graphitic phosphorous (ca. 132.5 eV). The splitting of the simulated peaks (shown as solid and dashed lines) results from taking into account the orbital splitting between $2p_{3/2}$ and $2p_{1/2}$ states.

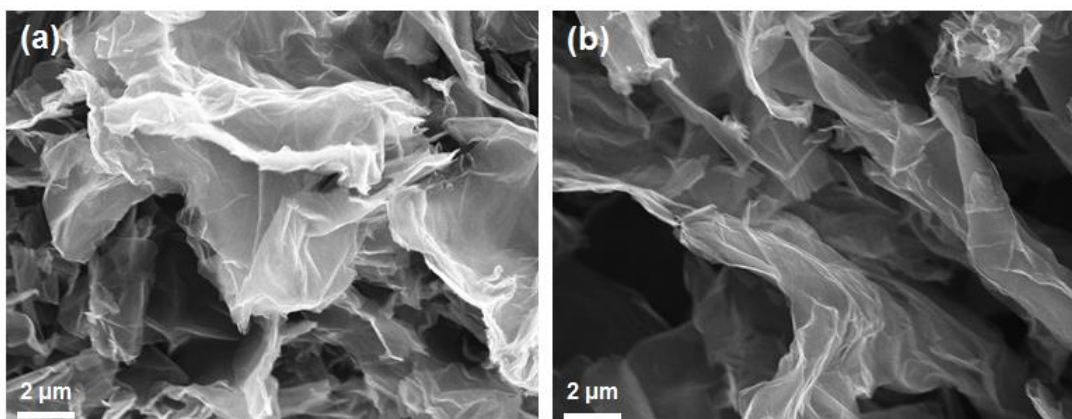


Figure 4.1: SEM images of A) PG-O and B) PG.

Interestingly, the XPS spectrum of PG-O also includes intensity at energies consistent with a high-oxidation-state phosphorous species, such as phosphorus pentoxide (P_2O_5) and/or orthophosphoric acid (H_3PO_4); which could be attributed to spontaneous reactions of existing white phosphorous under exposure to air and humidity. The proportion of the two oxygen-free P species (elemental and graphitic) in PG is higher than that of PG-O (79% vs 69% of total signal), indicating that the reductive environment created

by hydrogen at 1000 °C purifies the sample and removes any residual high oxidation state phosphorous species in PG.

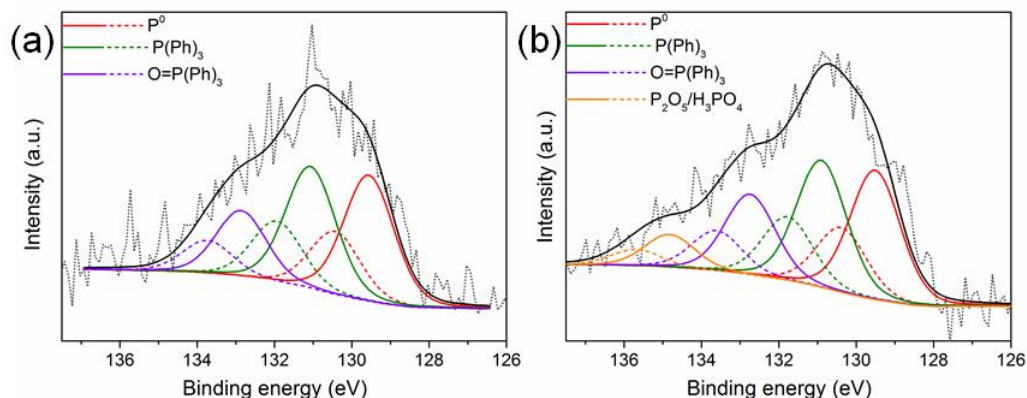


Figure 4.2: High Resolution P 2p-edge XPS spectra for A)PG and B)PG-O (N.B. here the label P(Ph)₃ refers to graphitic phosphorus).

ssNMR spectroscopy is introduced as a method of refining the XPS data given that the resolution is likely to be better in many cases, there are various spectral editing tools, and the technique reports on the overall composition of the sample rather than just the surface. ³¹P Hahn-echo spectra for PG and PG-O are shown in **Figure 4.3**. Both spectra are dominated by a similar feature: a ca. 45 kHz-broad resonance centred about 200 ppm. Similar to a previously reported ³¹P ssNMR spectrum of graphitic material, the extremely unusual breadth of this peak is attributed to a wide array of slightly different chemical environments expected to be found in the graphitic sheet and represents graphitic phosphorus (i.e. a PPh₃-like environment). The ³¹P Hahn-echo spectrum of PG shows a weaker signal for a similar number of scans compared to PG-O (due to an increased amount of insulating Teflon powder to facilitate data acquisition), but reflects graphitic P atoms complementary to those observed in PG.

The narrower peaks seen in the 30 to 0 ppm range in both spectra in **Figure 4.3** represent less than 2% of the total signal intensity, and are likely to be caused by small

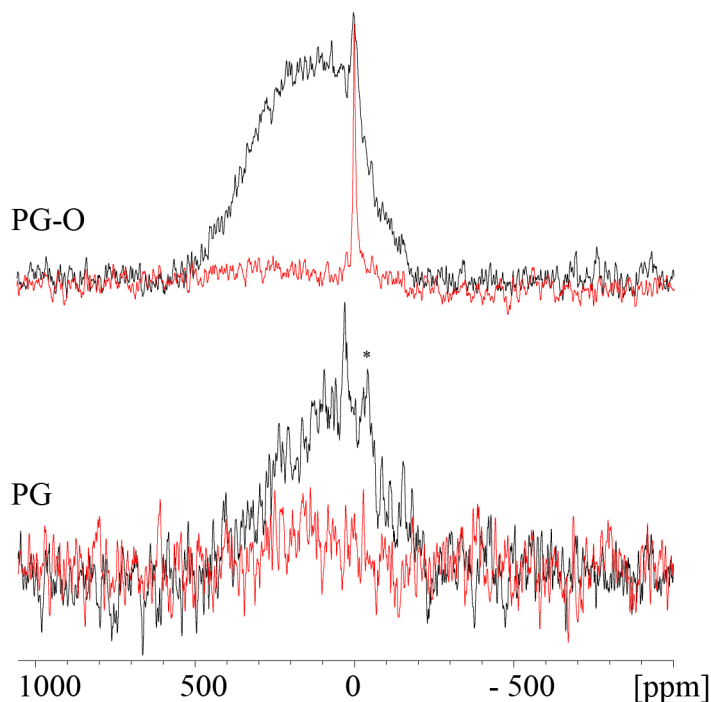


Figure 4.3: ^{31}P Hahn-echo (black) and ^1H - ^{31}P CPMAS (red) ssNMR spectra of PG-O and PG, collected at 7.0 T with an MAS rate of 20 kHz (23.5 ppm on this scale). Asterisks denote spinning sidebands. CPMAS signal intensity indicates phosphorus sites near in space to protons.

amounts of side products. Peaks in this shift range generally represent polyphosphate or polyorthophosphate species at different levels of hydration. ^{33}H - ^{31}P CPMAS spectra (shown in **Figure 4.3** in red) show a signal which matches the narrow peak in the direct spectrum only, indicating a short ^1H - ^{31}P internuclear distance and that the phosphate species in PG-O is likely either highly hydrated or a polyorthophosphate. The fact that no cross polarization occurs to the extremely broad peak is consistent with its assignment as a graphitic phosphorus environment, where protons would be remote. The sharp peaks in the PG spectrum are not seen the ^1H - ^{31}P CPMAS experiment, indicating a proton-deficient environment, likely caused by removal of residual graphene-surface alcohol groups in the reductive H_2 environment introduced at the end of the synthesis. These results highlight the complimentary nature of NMR and XPS in the study of bulk and surface composition even with extremely low amounts of sample.

It should be noted here that the two spectroscopies report on different locations in the sample: the XPS method is surface sensitive, while NMR spectra observe the overall composition. While the XPS data implies a relatively impure sample, where oxygenated and elemental phosphorous compose large parts of the spectrum, the NMR study demonstrates that past the surface, the composition is more homogeneous. There is only a few percent of oxygenated polyphosphates in the bulk material. The exact amount of elemental phosphorous is harder to ascertain, but it is reasonable to assume that if that amount were comparable to the amount of graphitic phosphorus, the observed line shape would be broader and more asymmetric. It is therefore estimated that the amount of elemental phosphorus in the sample is between 1 and 20%, which is in agreement with the XPS analysis. ^{31}P NMR spectra of the white and black allotropes of phosphorous yield sharp, easily detected peaks, while the (crystalline) violet and (disordered) red allotropes yield ca. 100 ppm broad peaks that would be difficult to separate from the broad one of the graphitic phosphorous if present in small amounts. Notably, a previous NMR study found violet or red phosphorous NMR peaks were visible above the graphitic signature in a doped graphene.^{34, 35} The first ^{31}P NMR spectrum of a P-doped graphene was recently reported and is generally in agreement with the present study.³³ However, the previously reported material was synthesized via an alternate route that aimed at providing much higher dopant levels, but resulted in a material with orders of magnitude more impurities than the material synthesized here. The present study shows that lower dopant levels produce more homogeneous samples, and that the analysis methods presented here would be useful in determining maximum doping levels. In particular, it appears to be important to use ssNMR to track the amount of oxygenated phosphorous compounds in the overall material, rather than the XPS observation of the surface composition. The benefits of a reliable synthesis method producing a homoge-

neous product are obvious, and analysis by both XPS and ssNMR is key to observing and controlling the nature of these complicated materials, and for implementing them in practical applications.

4.3.2 Phosphorus and Nitrogen-doped Carbon Nanotubes

SEM and TEM images of PNCNTs are shown in **Figure 4.4**. The length of PNCNTs from SEM is around 30 μm . The bamboo-like structure, which is characteristic of NCNTs, is clearly seen in the TEM images of the PNCNTs. Interestingly, there appear to be two types of tubes in **Figure 4.4B**, one with narrow channels and very thick walls (center and right), and a second type with wider channels (left side of image). This phenomenon was also recently observed by Nicolls et al.³⁶ Furthermore, the carbon planes are not perfectly parallel and have varying interplane distances, which are greater than those of standard sp^2 carbons and likely indicate disorder in the carbon lattice caused by the presence of heteroatoms.

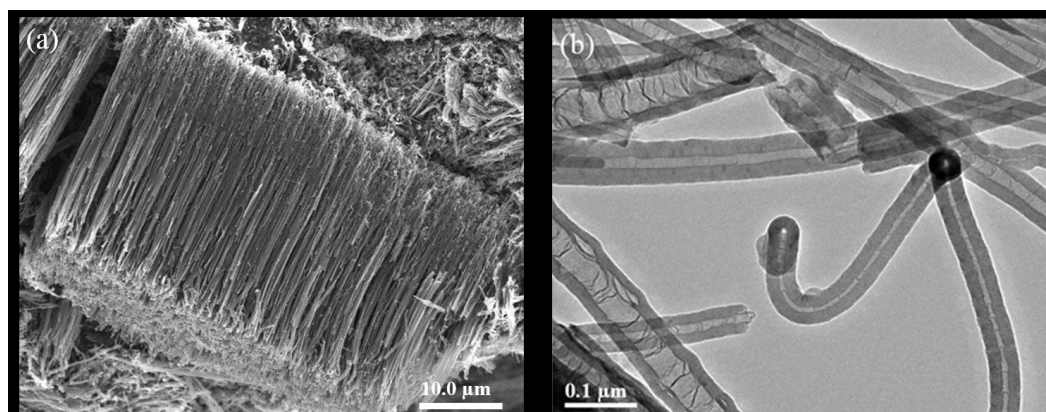


Figure 4.4: A) SEM and B) TEM of PNCNTs.

High-resolution N 1s and P 2p edge spectra for PNCNTs are shown in **Figure 4.5**. As shown in **Figure 4.5A**, there are two peaks within the N 1s signal. The peak centered at 398.1 eV corresponds to pyridinic N and the peak at 400.8 eV corresponds to graphitic

N. A high-resolution P 2p peak from the PNCNT sample is shown in **Figure 4.5B**. The peak centered 130.2 eV can be assigned to elemental phosphorus, while that at 132.5 eV corresponds to a P(Ph)₃-like bonding environment.

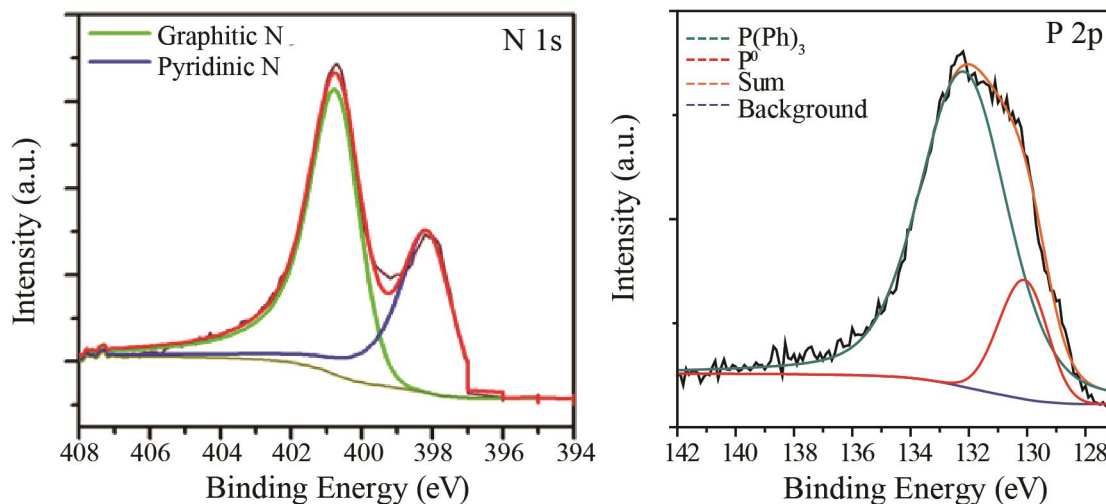


Figure 4.5: High Resolution A) N 1s-edge and B) P 2p-edge XPS spectra of PNCNTs.

Figure 4.6 shows a ³¹P echo spectrum of PNCNTs which is similar to the ³¹P spectrum collected for PG (as can be seen in a comparison in **Figure 4.7**). One broad peak is observed, centred at 250 ppm, and is assigned to graphitic phosphorus built into the walls of the CNTs. Similarly to PG and PG-O, no white or black elemental phosphorous is present, though there may be small amount of unresolved signal from disordered elemental phosphorous at 80 ppm. In contrast to the doped graphenes, the ³¹P NMR spectrum of PNCNTs does not support the presence of significant amounts of phosphate in the sample. Again, it should be noted that the XPS analysis may report elemental phosphorous and phosphate groups at the surface, while the NMR analysis shows that there is little of these impurities across the entire bulk of the sample. Categorization of these two observations is somewhat complicated by the poor resolution of the XPS spectrum. It is clear that in the many cases where XPS may be ambiguous, ssNMR can be used to verify any interpretations.

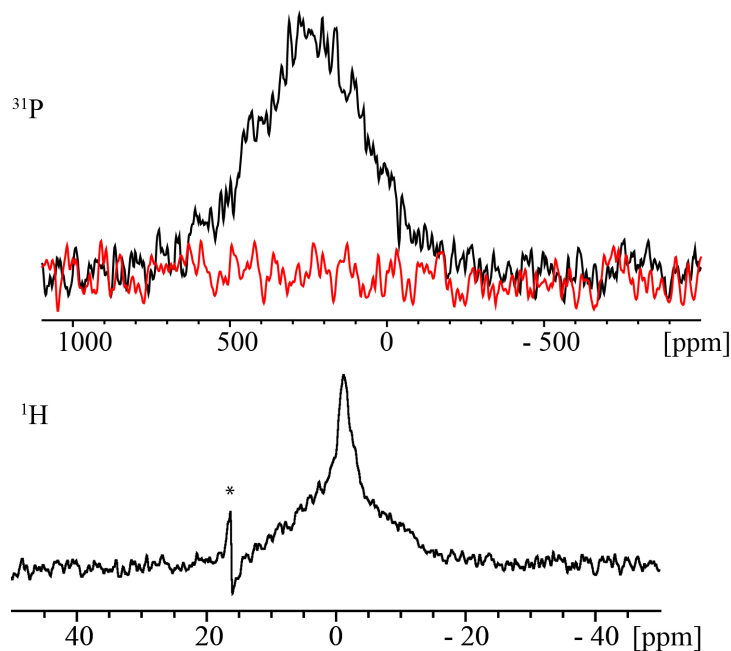


Figure 4.6: ^{31}P Hahn-echo (black, top) ^1H - ^{31}P CPMAS (red) and ^1H Hahn-echo (bottom) ssNMR spectra of PNCNTs collected at 7.4 T with an MAS rate of 20 kHz. The asterisk marks a transmitter artefact.

Perhaps most importantly, there is a difference in ^{31}P chemical shift between the dopant sites in the nanotubes and graphene sheets. This difference is likely related to differences in the band gap between the two materials, because of the well-known relationship between empty and full orbital energy spacing and the chemical shift.³⁷ The presence of a band structure analogous to that of a small band gap semiconductor or metal is hinted at by rapid ^{31}P spin-lattice (T_1) and spin-spin (T_2) relaxation rates, with rate constants on the order of a few milliseconds in both PNCNTs and PG. This result also serves to further demonstrate that the P dopant atoms are directly connected with the carbon materials, as there must be some source of fluctuating magnetic field (in this case, conduction electrons) to induce ^{31}P relaxation rates that are much faster than those found in insulating, diamagnetic materials. The apparent sensitivity of NMR to the band structure, via chemical shift changes and relaxation rates, suggests that this technique is well suited to the study of carbon materials doped for catalytic applications,

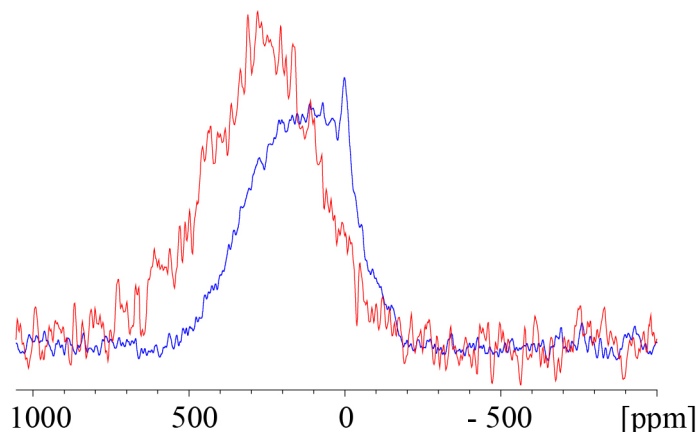


Figure 4.7: ^{31}P Hahn-echo spectra of PG-O (blue) and PNCNTs (red). The phosphorus sites are similar, but the chemical shift is clearly affected by changes in energy gaps in the band structure.

as this behaviour is undoubtedly related to the shape of the band surface and energy gaps.

Also shown in **Figure 4.6** are the ^1H echo and ^1H - ^{31}P CPMAS spectra of PNCNTs. An unusually weak ^1H signal in this material, coupled with the negative ppm shift seen in the main narrow peak at -1.3 ppm indicates this signal is caused by a small amount of (likely ambient) water adsorbed onto the CNT surfaces, shifted due to interactions with the ring currents of circulating π -electrons.³⁸⁻⁴⁰ The broader signal spanning from 10 to -10 ppm may be caused by carbon-bonded protons at the edges of nanotubes. The lack of any signal in the CP spectrum indicates that whatever protons are present are not near in space to the tube-wall phosphorus site (cf. N-doped graphene below).

4.3.3 Nitrogen-doped Graphene (NG)

Figure 4.8 shows an SEM image of NG displaying the expected sheet-like graphene morphology. The N 1s edge high-resolution XPS spectra of NG before and after treatment in ammonia are shown in **Figure 4.9**, apparently displaying peaks corresponding to graphitic (401.5 eV) and pyridinic (398.7 eV) nitrogen sites. The spectra are also

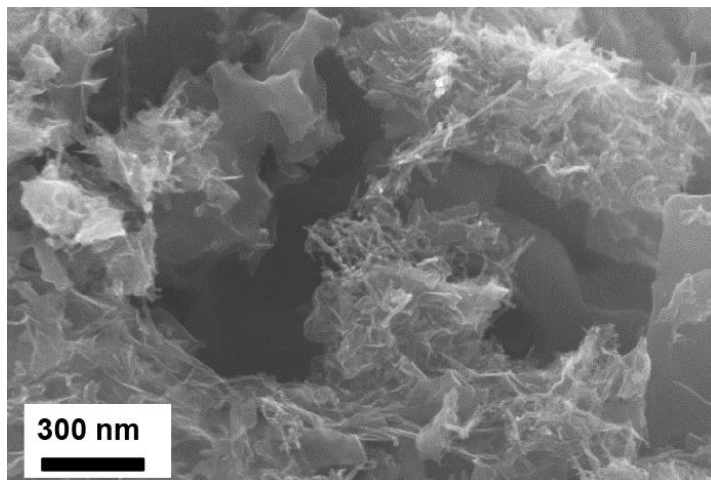


Figure 4.8: SEM image of NG.

consistent with the presence of some pyrrolic (400.2 eV) sites, though the low resolution makes this difficult to ascertain. Disregarding these potential sites, it seems that ammonia treatment increases the intensity of nitrogen signals for pyridinic and graphitic nitrogen. The graphitic to pyridinic nitrogen ratio for the samples before and after ammonia step were 1.2 and 1.8, respectively. Interestingly, the ratio of graphitic to pyridinic nitrogen is higher in the PNCNTs mentioned above, which suggests that the presence of the phosphorus atoms may play a role in promoting the formation of graphitic nitrogen species during doping.

Figure 4.10 shows a ^{15}N Hahn-echo NMR spectrum of ^{15}N -labelled NG (the NMR sample was not treated with ammonia). The spectrum displays two main features: a tall narrower peak centred about 172 ppm, and a broad feature spanning from 330 to 210 ppm at a ratio of about 1.3:1. A ^{15}N spectrum of graphene made by chemical reduction of graphene oxide with ^{15}N -labeled hydrazine has been reported by Ruoff et al., and shows a single nitrogen site at roughly 190 ppm. This resonance was attributed to edge-based pyrazole groups generated during the reduction process, as a side product of

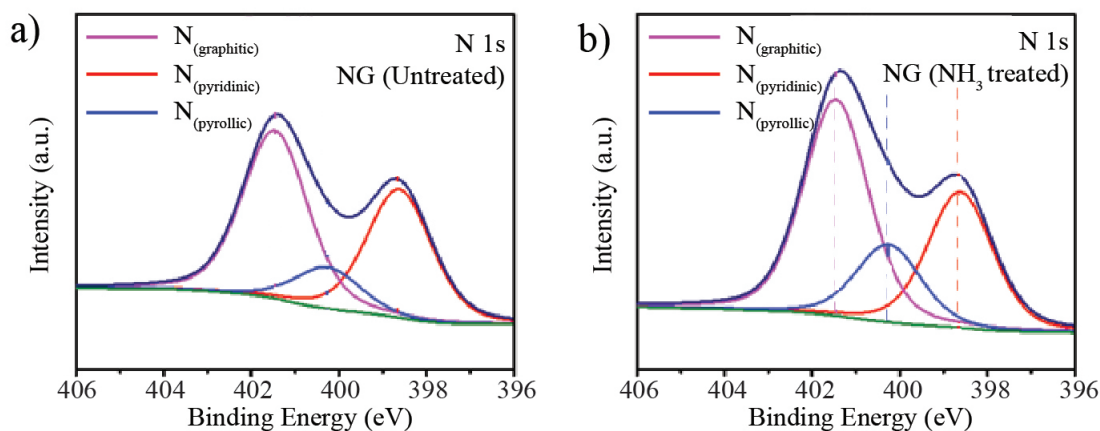


Figure 4.9: N 1s-edge XPS spectra of NG A) before and B) after high-temperature treatment with ammonia.

the chemical reduction of graphene oxide with hydrazine originally intended to produce graphene sheets.⁴¹

The ^{15}N chemical shifts observed in the material presented here are different than those observed by Ruoff et al., and the chemical environments are therefore quite different than the edge-terminating pyrazole groups. Also shown in **Figure 4.10** is a ^1H Hahn-echo NMR spectrum of NG including background suppression. Two sites are immediately apparent: at 0 and -2.7 ppm (the 7.2 ppm peak observed via D-HMQC is obscured by the 6.5 ppm peak due probe background). The low frequency peaks can be amplified or attenuated through humidification and dehumidification, and so they are assigned to water molecules which are adsorbed onto the graphitic sheets under the influence of a ring-current shift to lower-than-expected chemical shifts.^{38, 42–44}

A ^1H - ^{15}N dipolar heteronuclear multiple quantum coherence (D-HMQC) NMR spectrum, shown in **Figure 4.11A**, was collected to probe the existence of correlations between proton and nitrogen sites.⁴⁵ In broad terms, any correlation between ^1H and ^{15}N sites indicates these sites are near in space to one another and may be bonded together.

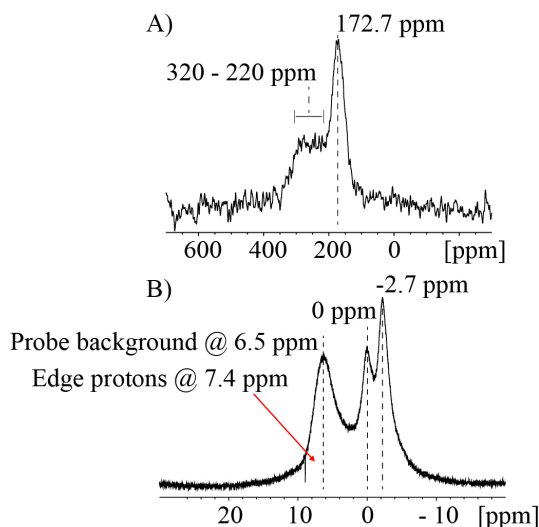


Figure 4.10: A) ^{15}N Hahn-echo and B) ^1H Hahn-echo ssNMR spectra of ^{15}N -labelled NG collected at 11.7 T with an MAS rate of 15 kHz.

The only correlation evident from this 2D spectrum links together a ^{15}N site at 145.7 ppm with a ^1H site at 7.2 ppm. The heteronuclear correlation experiment reveals that there are actually two ^{15}N resonances in the 120-200 ppm region: one from a site that is near a proton and one from a site that is not. **Figure 4.11B** illustrates this point and further confirms it via comparison of direct and two proton-excited ^{15}N NMR spectra (slice of 2D HMQC and 1D ^1H - ^{15}N CP). Only the direct ^{15}N spectrum is quantitative, and so this low-frequency, proton-correlated site is present at a smaller amount than the other two sites.

A recent study by Wang et al. investigated the likely ^{15}N chemical shifts for graphitic nitrogen via a first-principles computational analysis.⁴⁶ Their analysis was modeled as a single, relaxed (i.e. geometry optimized) graphene sheet in a vacuum, and was sensitive to changes in chemical environment and bandgap introduced by defects. Comparing this experimental data to the computational analysis by Wang et al., the high-frequency feature is assigned to pyridine-like nitrogen centers localized mainly along the zigzag and armchair edges of graphene sheets bonded to aprotic, sp^2 -hybridized carbons. In partic-

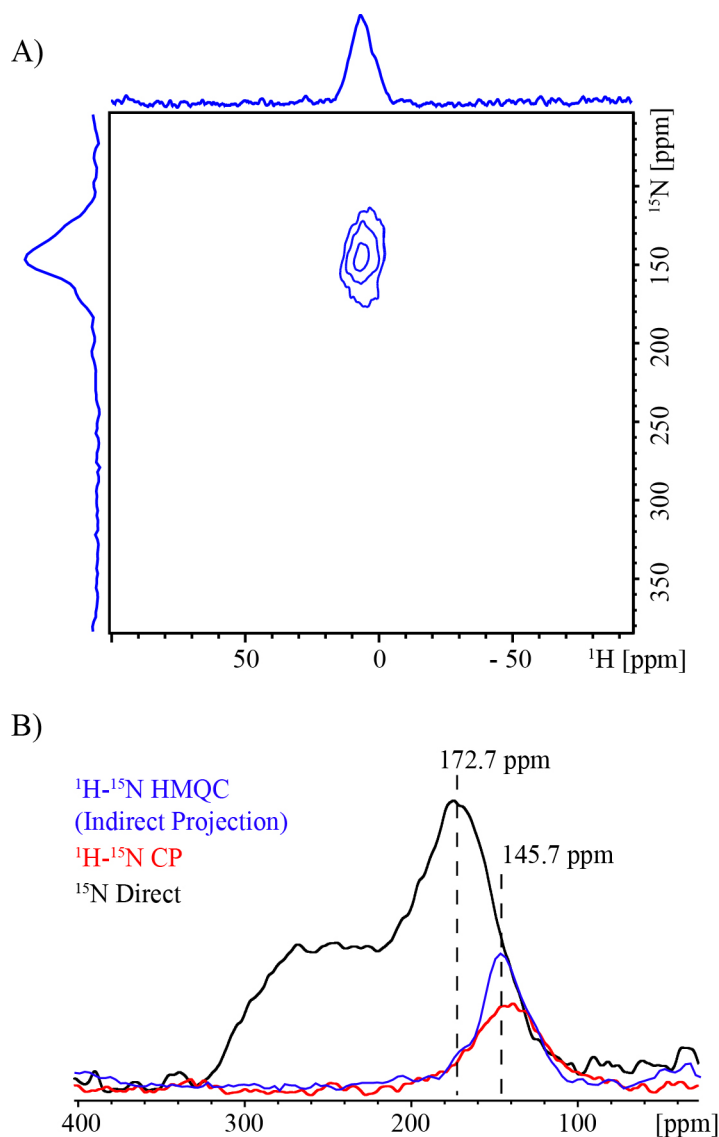


Figure 4.11: A) ^1H - ^{15}N D-HMQC 2D ssNMR spectrum of NG collected at 11.7 T with an MAS rate of 20 kHz. B) ^{15}N Hahn-echo and ^1H - ^{15}N CP (both collected at 20.0 T with an MAS rate of 30 and 15 kHz, respectively) spectra of NG compared with the indirect projection of a ^1H - ^{15}N 2D D-HMQC ssNMR spectrum.

ular, pyridinic sites near vacancy defects in the sheet satisfy both the chemical shift and aprotic environment consistent with the NMR spectrum. The proton-correlated nitrogen centers of the 145.7 ppm peak are in excellent agreement with calculated chemical shifts for z^{edge-1} nitrogen sites, which bridge two carbon rings at the sheet edges (where the nearby sheet edge necessitates C-H or C-OH termination groups that supply the N,H proximity observed via NMR). Without ^1H - ^{15}N correlation experiments, the peak

at 172 ppm might be erroneously assigned to a variety of protonated sites whose calculated chemical shifts are in approximate agreement. The nearest aprotic match sites are graphitic, either replacing a carbon atom in the normal graphene sheet or as part of a Stone-Wales or vacancy defects.⁴⁷ Finally, we note that more distant ^{15}N chemical shifts predicted for pyrrolic sites implies there is no significant amount of such environments present. However, the poor resolution of the surface-sensing XPS spectrum in that region prevents definitive conclusions about whether such sites are present at the surface despite contributing little to the overall composition. Additionally, we note that, to our knowledge, this is the first reported NMR observation of graphitic nitrogen sites, as opposed to edge-terminating pyrazole groups.⁴¹

Dopant ^{15}N Chemical Shifts:

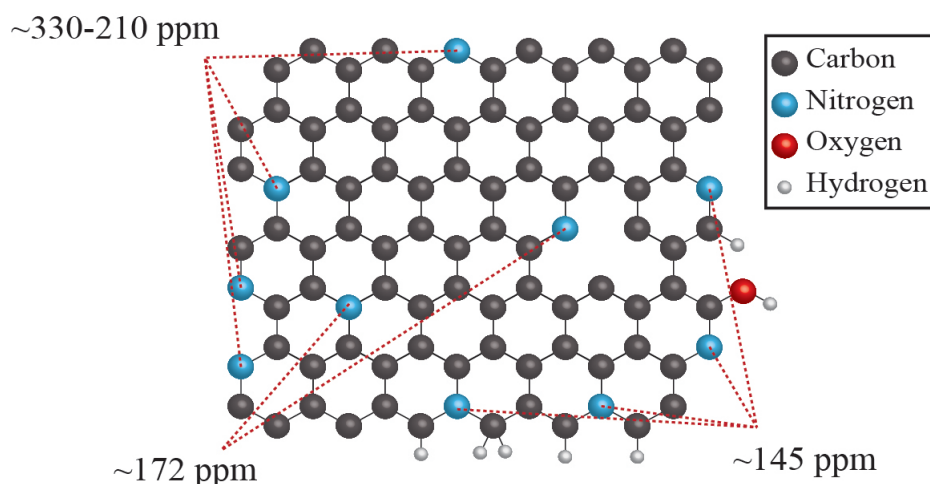


Figure 4.12: An illustration of a hypothetical graphene sheet with the nitrogen centers elucidated in this study. The chemical shifts of dopant nitrogen atoms are effected by nearby dopant sites due to band-gap changes, and so this particular sheet only serves illustrative purposes. Unnecessary protons are omitted.

An illustrated N-doped graphene sheet highlighting the N-dopant sites observed in this study is presented in **Figure 4.12**. Our ^{15}N results on nitrogen-doped graphene show this synthesis method produces relatively homogeneous N-sites i.e. roughly equal amounts of graphitic and pyridinic sites. This ssNMR result correlates with the XPS

analysis in **Figure 4.9**, though there is less resolution in the latter type of spectrum. The relationship between atomic structure and function can now be probed directly without worrying about side reactions and inactive or counteractive dopant sites. If there is a relationship between catalytic activity and site distribution, ssNMR is shown to be a valuable tool in discovering and probing it.

4.4 Conclusions

The chemical environment of dopant atoms in graphene sheets have been experimentally probed through ssNMR and XPS. A CVD based method using TPP as phosphorus and carbon source produces homogeneous, graphitic phosphorus sites with a high degree of specificity. Mechanisms of doping and physical behaviour of this material, especially as it compares to graphene, can be made reliably with this model. Similarly, a CVD method with aniline as the precursor produced graphene doped with a roughly equal proportion of edge-based and defect-based N-sites. To our knowledge, this is the first reported experimental ^{15}N ssNMR spectrum of NG, and it matches recently published simulations data well. The phosphorus sites of a polydoped CNT sample were also studied. ^{31}P spectroscopy resembles that found in PG, with a downfield shift likely attributable to the difference in band gap between these materials. It is shown that the application of the extreme sensitivity and selectivity of ssNMR to the study of modified graphitic materials is a challenging but revealing method of analysis.

References

- [1] Carrette, L.; Friedrich, K. A.; Stimming, U. *ChemPhysChem* **2000**, (1), 162–193.
- [2] Carrette, L.; Friedrich, K.; Stimming, U. *Fuel Cells* **2001**, 1(1), 5–39.
- [3] Goodenough, J. B.; Park, K.-S. *J. Am. Chem. Soc.* **2013**, 135(4), 1167–1176.
- [4] Jacobson, M. Z.; Delucchi, M. A. *Energy Policy* **2011**, 39(3), 1154–1169.
- [5] Winter, M.; Brodd, R. J. *Chem. Rev.* **2004**, 10(104), 4245–4270.
- [6] Bockris, J. O.; Veziroglu, T. N. *Int. J. Hydrogen Ener.* **2007**, 32(12), 1605–1610.
- [7] Connolly, D.; Lund, H.; Mathiesen, B. *Renew. Sust. Ener. Rev.* **2016**, 60, 1634–1653.
- [8] Lauber, V.; Jacobsson, S. *Environ. Innov. Soc. Trans.* **2016**, 18, 147–163.
- [9] Nizami, A.; Shahzad, K.; Rehan, M.; Ouda, O.; Khan, M.; Ismail, I.; Almeelbi, T.; Basahi, J.; Demirbas, A. *Appl. Ener.* **2017**, 186, 189–196.
- [10] Andor, M.; Voss, A. *Resour. Ener. Econ.* **2016**, 45, 144–158.
- [11] Qiao, J.; Xu, L.; Ding, L.; Zhang, L.; Baker, R.; Dai, X.; Zhang, J. *Appl. Catal. B* **2012**, 125, 197–205.
- [12] Susac, D.; Sode, A.; Zhu, L.; Wong, P.; Teo, M.; Bizzotto, D.; Mitchell, K.; Parsons, R.; Campbell, S. *J. Phys. Chem. B* **2006**, 110(22), 10762–10770.
- [13] Xu, L.; Pan, G.; Shi, X.; Zou, C.; Zhou, Y.; Luo, G.; Chen, G. *Electrochimica Acta* **2015**, 177, 57–64.
- [14] Gong, K.; Du, F.; Xia, Z.; Durstock, M.; Dai, L. *Science* **2009**, 323(5915), 760–764.
- [15] Cruz-Silva, E.; Lopez-Urias, F.; Munoz-Sandoval, E.; Sumpter, B. G.; Terrones, H.; Charlier, J.-C.; Meunier, V.; Terrones, M. *ACS Nano* **2009**, 3(7), 1913–1921.
- [16] Czerw, R.; Terrones, M.; Charlier, J.-C.; Blase, X.; Foley, B.; Kamalakaran, R.; Grobert, N.; Terrones, H.; Tekleab, D.; Ajayan, P. *Nano Lett.* **2001**, 1(9), 457–460.
- [17] Zhang, H.-J.; Yuan, X.; Sun, L.; Yang, J.; Ma, Z.-F.; Shao, Z. *Electrochimica Acta* **2012**, 77, 324–329.
- [18] Ma, X.; Ning, G.; Qi, C.; Xu, C.; Gao, J. *ACS Appl. Mater. Interfac.* **2014**, 6(16), 14415–14422.
- [19] Alam, T. M.; Friedmann, T.; Schultz, P. A.; Sebastiani, D. *Phys. Rev. B* **2003**, 67(24), 245309.
- [20] Cai, W.; Piner, R. D.; Stadermann, F. J.; Park, S.; Shaibat, M. A.; Ishii, Y.; Yang, D.; Velamakanni, A.; An, S. J.; Stoller, M. *Science* **2008**, 321(5897), 1815–1817.
- [21] Blanc, F.; Leskes, M.; Grey, C. P. *Acc. Chem. Res.* **2013**, 46(9), 1952–1963.

- [22] Liu, T.; Leskes, M.; Yu, W.; Moore, A. J.; Zhou, L.; Bayley, P. M.; Kim, G.; Grey, C. P. *Science* **2015**, *350*(6260), 530–533.
- [23] Leskes, M.; Kim, G.; Liu, T.; Michan, A. L.; Aussenac, F.; Dorffer, P.; Paul, S.; Grey, C. P. *J. Phys. Chem. Lett.* **2017**, *8*(5), 1078–1085.
- [24] MacIntosh, A. R.; Harris, K. J.; Goward, G. R. *Chem. Mater.* **2015**, *28*(1), 360–367.
- [25] Harris, K. J.; Bugnet, M.; Naguib, M.; Barsoum, M. W.; Goward, G. R. *J. Phys. Chem. C* **2015**, *119*(24), 13713–13720.
- [26] Harris, K. J.; Reeve, Z. E.; Wang, D.; Li, X.; Sun, X.; Goward, G. R. *Chem. Mater.* **2015**, *27*(9), 3299–3305.
- [27] Usachov, D.; Vilkov, O.; Gruneis, A.; Haberer, D.; Fedorov, A.; Adamchuk, V.; Preobrajenski, A.; Dudin, P.; Barinov, A.; Oehzelt, M.; others. *Nano Lett.* **2011**, *11*(12), 5401–5407.
- [28] Wang, H.; Maiyalagan, T.; Wang, X. *ACS Catal.* **2012**, *2*(5), 781–794.
- [29] Liu, H.; Liu, Y.; Zhu, D. *J. Mater. Chem.* **2011**, *21*(10), 3335–3345.
- [30] Hummers Jr, W. S.; Offeman, R. E. *J. Am. Chem. Soc.* **1958**, *80*(6), 1339–1339.
- [31] Rumble, J.; Bickham, D.; Powell, C. *Surf. Interf. Anal.* **1992**, *19*(1-12), 241–246.
- [32] Bertani, P.; Raya, J.; Bechinger, B. *Sol. State Nuc. Magn. Res.* **2014**, *61*, 15–18.
- [33] Matthews, P. D.; King, T. C.; Glass, H.; Magusin, P. C.; Tustin, G. J.; Brown, P. A.; Cormack, J. A.; García-Rodríguez, R.; Leskes, M.; Dutton, S. E.; others. *RSC Adv.* **2016**, *6*(67), 62140–62145.
- [34] Bytchkov, A.; Fayon, F.; Massiot, D.; Hennet, L.; Price, D. L. *Phys. Chem. Chem. Phys.* **2010**, *12*(7), 1535–1542.
- [35] Lange, S.; Schmidt, P.; Nilges, T. *Inorg. Chem.* **2007**, *46*(10), 4028–4035.
- [36] Nicholls, R. J.; Aslam, Z.; Sarahan, M. C.; Sanchez, A. M.; Dillon, F.; Koós, A. A.; Nellist, P. D.; Grobert, N. *Phys. Chem. Chem. Phys.* **2015**, *17*(3), 2137–2142.
- [37] Ramsey, N. F. *Phys. Rev.* **1950**, *78*(6), 699.
- [38] Harris, R. K.; Thompson, T. V.; Norman, P. R.; Pottage, C.; Trethewey, A. N. *J. Chem. Soc., Faraday Trans.* **1995**, *91*(12), 1795–1799.
- [39] Harris, R. K.; Thompson, T. V.; Norman, P. R.; Pottage, C. *J. Chem. Soc., Faraday Trans.* **1996**, *92*(14), 2615–2618.
- [40] Harris, R.; Thompson, T.; Forshaw, P.; Foley, N.; Thomas, K.; Norman, P.; Pottage, C. *Carbon* **1996**, *34*(10), 1275–1279.
- [41] Park, S.; Hu, Y.; Hwang, J. O.; Lee, E.-S.; Casabianca, L. B.; Cai, W.; Potts, J. R.; Ha, H.-W.; Chen, S.; Oh, J.; others. *Nature Comm.* **2012**, *3*, 638.

- [42] Harris, R. K.; Thompson, T. V.; Norman, P. R.; Pottage, C. *Carbon* **1999**, *37*(9), 1425–1430.
- [43] Ouriadov, A. V.; MacGregor, R. P.; Balcom, B. J. *J. Mag. Res.* **2004**, *169*(1), 174 – 186.
- [44] Pachauri, R. K.; Meyer, L. A. *IPCC* **2014**, (1), 360–367.
- [45] Gan, Z. *Journal of Magnetic Resonance* **2007**, *184*(1), 39–43.
- [46] Wang, X.; Hou, Z.; Ikeda, T.; Terakura, K. *J. Phys. Chem. C* **2014**, *118*(25), 13929–13935.
- [47] Stone, A. J.; Wales, D. J. *Chem. Phys. Lett.* **1986**, *128*(5), 501–503.

5 — The Effects of Temperature and Relative Humidity on Proton Conductivity in Composite SPEEK - Functionalized Graphite Polymer Electrolyte Membranes

This chapter is a reformatted version of an article which, at the time of this writing, is in preparation for submission to *ECS Transactions* for publication. The co-authors were Maria Maqsood, Kristopher Harris, and Gillian Goward. M.M. was responsible for most of the synthesis of precursor materials and casting of the doped membrane samples, as well as some of the electrochemical analysis. The author was responsible for the remaining synthetic work and electrochemical analysis, as well as the solid-state NMR (ssNMR) characterization and analysis, and preparation of the manuscript. Ionomeric sulfonated polyether ether ketone (SPEEK) membranes were doped with functionalized graphenes, and the proton conductivity of these composite membranes was measured at fuel cell operational temperatures and percent relative humidities (%RH). The differences in proton conductivity between pure SPEEK membranes and composites with different dopants and doping levels at varied conditions were investigated through high-field ^1H ssNMR. It was found that high-speed MAS was able to dehydrate membranes under water-saturated conditions, and so lower %RH conditions were better able to produce reliable ssNMR results. The addition of graphitic dopants appeared to have an overall detrimental effect on the bulk proton conductivity of membranes, while concurrently these doped membranes had a broadened operational temperature window.

5.1 Introduction

Hydrogen fuel cell (FC) technology represents part of a solution to the world's energy crisis. These energy application systems are used in automotive, military, and bulk power industries to provide reliable and high-density energy, consuming hydrogen gas and producing water as a by-product. Provided that the hydrogen fuel is sourced from an environmentally neutral process, FC technology represents a viable, completely green alternative to fossil fuels. While many iterations of FCs have been developed over the past century, one of the most sophisticated and ubiquitous is the polymer electrolyte membrane FC (PEM-FC). The device has a number of complicated components which must all work well together, but ionomeric membrane performance holds a disproportionate amount of responsibility for fuel cell efficiency. Ionomer is present in both electrodes as well as being the main constituent of the PEM, and ionomer proton conductivity, σ , at varied environmental conditions is a highly studied parameter.

NafionTM, a fluorinated sulfonic acid polymer material, is the current industry benchmark, with remarkably high proton conductivity (0.1 - 1 S/cm) under a specific, narrow set of circumstances (100% relative humidity, ca. 80 °C).¹⁻³ Higher temperatures than these would be kinetically favourable to the electrochemical processes in the electrodes and would theoretically increase performance, however the retention of water at these temperatures becomes a serious issue. Water loss causes hydrophilic channels within the material to collapse, causing a catastrophic drop in proton conductivity. NafionTM is also expensive and difficult to produce. Many alternative ionomer materials are under investigation as a replacement for NafionTM, improving on its performance at a wider range of conditions. One candidate, sulfonated poly ether ether ketone (SPEEK), displays

similar hydrophilic channel formation and somewhat less impressive proton conductivity under differing conditions, and crucially is less expensive.

As a result, SPEEK is commonly used as a base material for studying the effect of dopant addition to the PEM layer on proton conductivity and operational condition robustness. The addition of small amounts of electrochemically inactive material has been shown to increase proton conductivity and to shift the optimal operational range window of ionomer materials, in order to allow for better proton conductivity at high temperatures (for generally increased fuel cell performance) as well as lower temperatures (e.g. for cold-start automotive applications, etc.).⁴⁻⁶ This phenomenon is not exclusive to SPEEK: composite membranes of NafionTM and silica particles showed materially improved proton conductivity over pure NafionTM, attributed to an extended hydrogen bond network involving the ionomer, silica surface hydroxide groups, and proton-conducting water.⁷ Composites of NafionTM with SPEEK and graphene oxide (GO) showed nearly a 50% increase in proton conductivity over a pure membrane under the same conditions, however composition did seem to reduce the physical robustness of the membranes.⁸

Graphene oxide and its functionalized analogues are garnering significant attention in the research of energy storage systems; ion batteries and supercapacitors in addition to fuel cells.⁹⁻¹³ Compressed sheets of GO have shown intrinsic proton conductivity, however only in the plane of the graphitic sheets. Protons are likely conducted through a Grotthus-type mechanism through rigidly hydrogen bonded water layers sandwiched between GO sheets. Functionalization of GO with acidic functional groups produces functionalized GO (FGO) species such as the sulfonated GOs (SGOs). SGOs have shown an increased ability to exchange protons with solvent, and show shorter inter-layer spacings when dried.¹⁴ Sulfonated GO (SGO) has displayed proton conductivity

enhancing behaviour in a number of different ionomer matrices, including NafionTM, sulfonated polyimide, SPEEK and others.^{13, 15-17} While increased proton conductivity upon doping ionomers is well observed in the literature, it is poorly explained. One promising method of analysis potentially able to explain these phenomena is solid-state nuclear magnetic resonance spectroscopy, thanks to its extreme chemical site specificity and its ability to resolve only slightly different chemical environments.

ssNMR has been used successfully to monitor and characterize ion dynamics in energy storage solids routinely in the preceding decades. Lithium ion mobility in battery electrode materials is a well-trodden area of investigation, where ssNMR has been used to identify unexpected ion-hopping pathways in, by way of a recent example, crystalline Li_2SnO_3 , helping to explain its previously curious electrochemical performance.¹⁸ Many similar examples of the use of ssNMR to characterize ion-hopping rates and pathways for the purpose of identifying promising battery electrode materials are available in recent literature.¹⁹⁻²² Likewise, ionomeric materials can be well-characterized through ssNMR, however these polymers generally are not crystalline, and so more sophisticated experiments are required to produce useful results. Exploiting dipolar coupling between acidic protons has been used to characterize and compare the conductivity of a number of proton-conducting solid acids.²³ Fluorine coupling can be used with remarkable precision to discriminate between mobile and stationary phases within the same ionomer.²⁴ Where possible, simple 1D ^1H ssNMR spectroscopy can be used to watch for acid - water peak coalescence, which is linked intricately to water uptake and proton conductivity.²⁵

The goal of this study was to synthesize SPEEK membranes with varying wt% of GO and propylsulfonic GO (PGO), containing dopant levels of 0.1 - 5 %. The proton conductivity of these composite membranes was recorded at fuel cell operational conditions, ranging from 50 - 90 °C and 50 - 100 %RH. ^1H ssNMR was also used to in-

investigate the proton environments in the membrane samples under the same conditions. Differences in the bulk proton conductivity, water uptake, and / or optimal operational window between composite membranes and pure SPEEK under similar conditions were rationalized using the results of the ^1H ssNMR analysis.

5.2 Experimental

5.2.1 Membrane & Dopant Synthesis

Poly Ether Ether Ketone (PEEK) was obtained from Victrex[®]. Sulfuric acid (98%), Graphite powder (<20 μm , synthetic), dimethyl sulfoxide (99.9 %, anhydrous), sodium nitrate (>97%), potassium persulfate (98%), phosphorus pentoxide (98%), and 1,3-propanesultone (98 %) were purchased from Millipore-Sigma[®]. Potassium permanganate (99%) was purchased from Caledon Laboratories Ltd. Hydrogen peroxide (30%) was purchased from Fischer Chemical[®]. All chemicals were used as received.

Batches of SPEEK membranes with different degrees of sulfonation were synthesized using a previously reported procedure.²⁶ PEEK was dried at 110 °C for 24 hours. The dried PEEK chips were dissolved in H_2SO_4 at a mass ratio of 1 : 27.6 and stirred vigorously at 50 °C for between 16 hours and 10 days, with longer reaction times producing SPEEK solutions with a higher degree of sulfonation. The solution was added drop-wise to cold deionized water to induce polymerization. The adhesive, web-like polymer was rinsed with more cold deionized water until the run-off was measured to be pH neutral. The polymer was then dried at 70 °C for 24 hours. The SPEEK was soaked in 1M H_2SO_4 for acidification, then rinsed with deionized water until the run-off was pH neutral and dried at 70 °C for 24 hours.

Graphene oxide (GO) was synthesized using a multi-step modified Hummer's oxidation method.^{27, 28} Graphite powder (4 g), $K_2S_2O_8$ (2 g) and P_2O_5 (2 g) were added to concentrated sulfuric acid (12 mL) and heated to 80 °C for 2 hours while stirring. The mixture was vacuum-filtered and washed with deionized water, methanol, and ethanol sequentially, and the product was dried at 40 °C overnight. The black solids were ground to a powder, then suspended in concentrated H_2SO_4 (100 mL) and cooled to 0 °C. $KMnO_4$ (14.9 g) was added very slowly, ensuring the reaction mixture's temperature did not exceed 20 °C. The mixture was heated to 35 °C and stirred vigorously for 2 hours. After cooling to 0 °C, H_2O_2 (11.8 mL, 30%) in deionized water (160 mL) were added slowly, and the mixture was stirred for a further 1 hour. The mixture was centrifuged for 10 minutes at 4000 rpm and the liquid phase discarded. The solid was then re-suspended in 100 mL deionized water and re-centrifuged, discarding the liquid phase and repeating a total of three times. The sample procedure was carried out once more each with 100 mL ethanol and methanol. The resulting GO solid was dried in vacuo at 40 °C overnight.

Using GO as a starting material, propylsulfonic graphene oxide (PGO) was synthesized following a modified literature procedure.²⁹ 1,3-propanesultone (1.5 g) was added to a suspension of GO in toluene (300 mL @ 2.5 g/mL) which had been sonicated for 4 hours. A 24 hour reflux period followed. Work-up by centrifugation, washing in 50% ethanol/water and drying at <100 °C produced the finished PGO sample. The sample was held in vacuo at 80 °C overnight.

5.2.2 Membrane Casting & Treatment

SPEEK - graphene composite membranes were drop-cast from solutions in DMSO. A minimal amount of solvent was used in order to make the casting solution as viscous as

possible to produce membranes with a uniform thickness with reduced dopant settling during the casting process. Membranes with dopant levels from 0.1 to 5 wt% were synthesized. Appropriate amounts of SPEEK and GO or PGO were mixed with minimal amounts of DMSO. The SPEEK mixture was stirred vigorously to dissolve the polymer, while the dopant mixture was sonicated for 2 hours. The dopant solution was added to the SPEEK solution, and the mixture was stirred for 1 hour. The viscous casting solution was drop-cast onto glass microscope slides which were heated to 80 °C in vacuo overnight, after which the membranes were collected. Pure SPEEK membranes were also produced using a similar procedure without the addition of dopant material.

In order to remove residual DMSO and re-acidify the membranes, they were treated according to the following cleaning procedure. The membranes were stirred vigorously in a 3 % H₂O₂ solution for 1 hour. This process was repeated using deionized water, changing out the water a total of 4 times. Finally, the membranes were stirred in a 1M H₂SO₄, and rinsed with deionized water until the run-off was pH neutral. The samples were then dried at 70 °C in vacuo overnight. Where necessary, the dried membranes were humidified in a Dongguan Lixian Scientific Instrument Company[®] HZ-2006 environmental test chamber at 60 °C at a fixed percent relative humidity (%RH) ranging from 50 - 100 % for 2 hours.

5.2.3 Characterization

ssNMR spectra were collected on Bruker Avance 300 and 850 MHz spectrometers using 1.9 or 4 mm MAS rotors spinning at 10 or 40 kHz. ¹H spectra were referenced to adamantane at 1.85 ppm. Typically, hard pulses were calibrated to produce a nutation frequency of 62.5 kHz, and where necessary, 50 kHz of tppm ¹H decoupling was applied. Variable temperature (VT) ssNMR was performed at temperatures ranging from 30 to

80 °C. Baseline-correcting Hahn echo experiments were performed using echo times ranging between 25 and 100 μ s. Membrane samples were packed into MAS rotors and treated at 60 °C at varied %RH to characterize the materials under fuel cell operating conditions.

Electrochemical impedance spectroscopy (EIS) was performed using a Gamry Reference 600 potentiostat using an in-plane 4 electrode conductivity test cell. Membrane samples were cut into strips measuring approximately .5 x 4 cm and fixed within the test cell. The cell was placed in an environmental test chamber and equilibrated at condition for 2 hours before tests were run. Potentiostatic EIS curves were collected in triplicate using AC carrier frequencies between 10^1 and 10^5 Hz.

The percentage water uptake (WU%) was determined by comparing dry and humidified masses of the membrane samples. Membranes were dried at 70 °C in vacuo overnight, and their dry masses, (m_{dry}), were recorded. The samples were then held at 60 °C and the specified %RH for 2 hours, after which their wet masses, (m_{wet}), were recorded. WU% was calculated from these measurements according to the following equation:

$$WU\% = \frac{(m_{wet} - m_{dry})}{m_{dry}} \times 100 \quad (5.1)$$

5.3 Results & Discussion

5.3.1 SPEEK Degree of Sulfonation

The degree of sulfonation (DoS) of SPEEK can have a marked effect on the membrane's performance as a proton conductor. Near-full sulfonation levels are possible by stirring PEEK in H₂SO₄ for extended periods of time (i.e. 10+ days) or by mixing and

stirring at elevated temperatures. However, SPEEK membranes with ca. 100% sulfonation are not necessarily optimal for fuel cell incorporation, as at higher temperatures and %RH these membranes may begin to self-dissolve from precipitation of H_2SO_4 . The DoS of the membranes synthesized in this study were measured using ^1H solution-state NMR. Samples were dissolved in DMSO with trace amounts of TMS used as an internal chemical shift standard. Spectra were recorded using a two-channel solution state probe in a 9.4 T Bruker Avance II magnet. A 500 MHz carrier frequency was used to apply 45° pulses with a nutation frequency of 100 kHz. A recycle delay of 4 seconds was found to relax all relevant signals sufficiently for quantitative analysis of the spectra, and 16 transients were recorded to provide a sufficient signal to noise ratio. The results of this analysis, along with a sample spectrum and structural model of SPEEK with site assignments, are shown in **Figure 5.1**.

SPEEK DoS is calculated from the integrated intensity of the assigned peaks according to the following equation:

$$DoS = \frac{H_A}{(H_B + H_{B'} + H_C + H_{C'} + H_D + H_{D'} + H_E + H_{E'}) + (2 \times H_A)} \times 100 \quad (5.2)$$

Where H_x represents the relative intensity of peak x . Membrane samples which were stirred in H_2SO_4 for times of 1, 4 and 8 days showed DoS values of 38%, 62 %, and 80%, respectively. Considering its proton conductivity and relative stability at higher temperatures and %RH, the 80% sulfonated SPEEK was used as the polymer matrix for all composite membranes in this study.

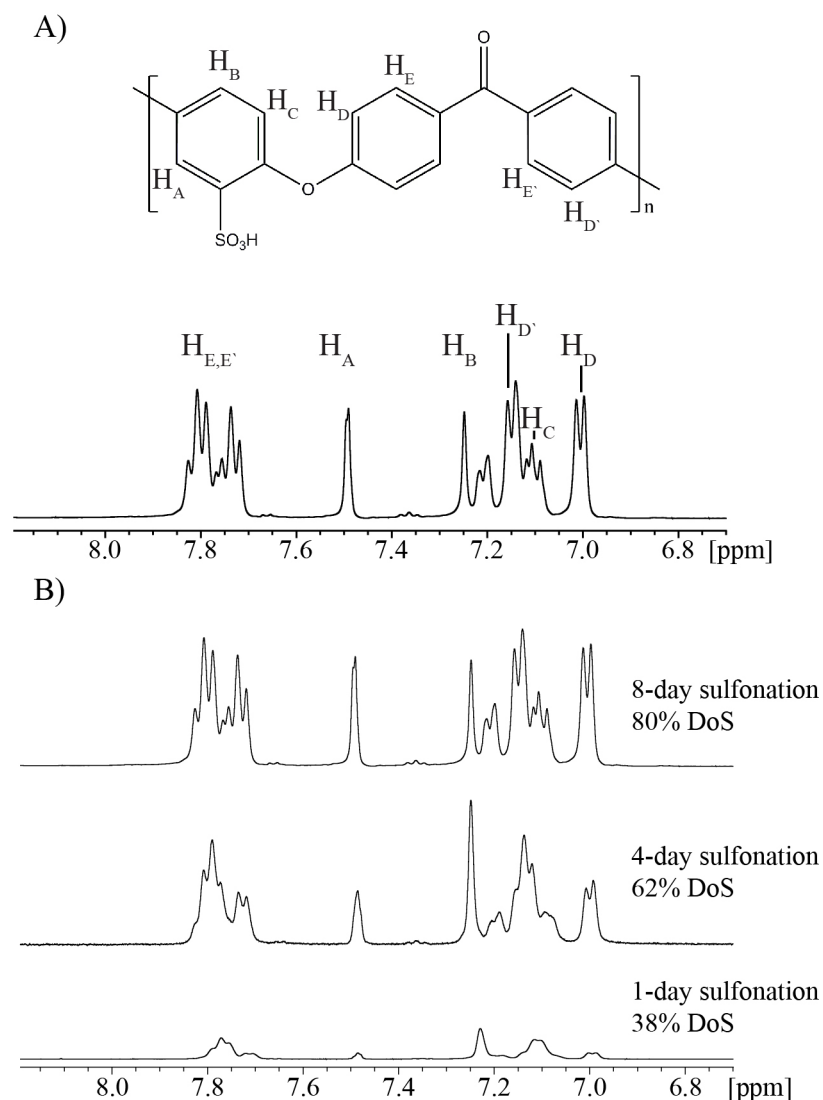


Figure 5.1: A) Sample ^1H solution NMR spectrum of SPEEK, with structural model and peak assignments. B) ^1H solution NMR spectra of SPEEK samples sulfonated for increasing times, with calculated DoS.

5.3.2 Low Temperature, High %RH Conditions

The first half of this study was aimed at characterizing SPEEK composites at saturated (i.e. 100 %RH) to investigate these materials where proton mobility would be at its highest. Unlike NafionTM, at higher temperatures SPEEK membranes tend to liquefy when saturated, and so lower temperatures were used during the measurements presented in this section as a necessity. SPEEK, as well as composites with 0.1, 1 and

5 wt% GO and PGO, were tested through EIS and ^1H ssNMR, and the results of this analysis are presented in the following section.

5.3.2.1 EIS at Operational Conditions

The proton conductivity of SPEEK composite membranes with GO and PGO at variable temperatures are shown in **Figure 5.2**. At these environmental conditions, there is a clear improvement in proton conductivity when certain loadings of dopant are used. The GO-SPEEK composites, whose EIS results are shown in **Figure 5.2A** show ca. four times the proton conductivity across the 30 - 50 °C range than pure SPEEK for the 0.1 and 1 wt% composites. The 5 wt% composite, however, has a proton conductivity very similar to the pure SPEEK membrane. It is possible that, for the GO dopant at higher concentrations, the positive effects of increased hydrogen bonding with water seen in the lower wt% composites is being near-perfectly offset by blocking, or preventing the formation of, proton conducting hydrophilic channels in the ionomer matrix. Within error, the proton conductivities of the 0.1 and 1 wt% seem to match, and no clear trend is noted relating the conductivity of either improved material to the ambient temperature when fully hydrated.

Figure 5.2B shows the temperature response (between 30 and 50 °C) of proton conductivity for SPEEK-PGO composites of 0.1, 1, and 5 wt%. A smaller increase in proton conductivity is seen when compared to the GO composites, certain composites measuring between 2 and 3 times the proton conductivity of pure SPEEK membranes. A similar pattern emerges to that seen for the GO composites, where dopant levels of 5% show no improvement in proton conductivity, likely due to similar reasons as those mentioned above. It was recently described that the interlayer spacing in GO is wider than in PGO, and that acidic proton exchange between water and PGO is remarkably

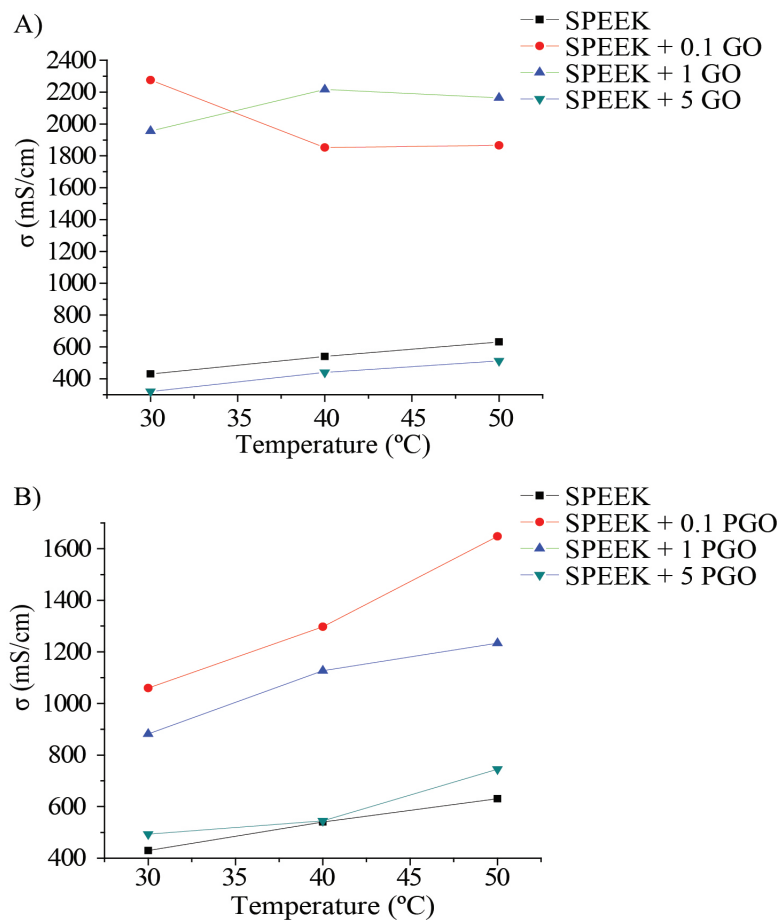


Figure 5.2: Proton conductivity (σ in S/cm) as a response to increasing temperature measured by EIS for A) SPEEK-GO and B) SPEEK-PGO composites.

slow.¹⁴ These results are echoed in the observations here: an increased layer spacing in GO implies the dopant is able to carry more water into the composite, and shorter layer spacings, coupled with poor proton exchange, in PGO would lead to a diminished water carrying and proton-exchanging ability in a composite under similar circumstances.

5.3.2.2 ^1H ssNMR at Operational Conditions

Figure 5.3 shows ^1H ssNMR spectra of SPEEK under different conditions. Under dehydrated conditions, the spectra show two main features: a sharp peak at ca. 8.2 ppm representing acidic protons and a broad peak at ca. 5.8 ppm representing the aromatic protons of the PEEK backbone. Upon hydration, the acidic water peak shifts to ca. 6

ppm and intensifies due to the increased presence of water. The change in chemical shift is attributed to coalescence with a more liquid water-like phase, and is associated with improved water uptake and proton conductivity. The aromatic peak is still visible, now obscured by the intense acidic peak. After roughly 16 hours of MAS, a new ^1H spectrum shows the acid water peak has attenuated and shifted to slightly higher frequency, i.e. closer to a dehydrated state. This may serve as evidence that in-rotor dehydration is occurring, as a result of increased rotor temperatures due to friction from MAS or to centrifugal forces ‘squeezing’ water from the polymer.

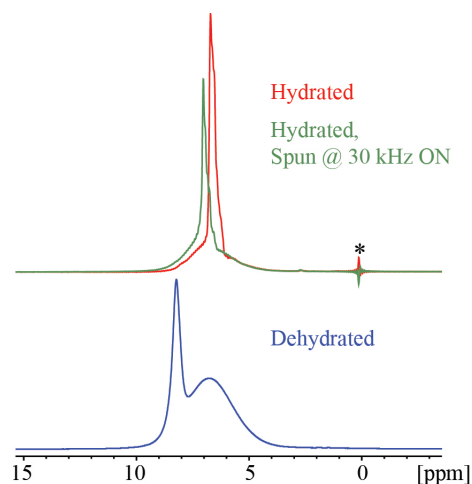


Figure 5.3: ^1H Hahn echo spectra for SPEEK under dehydrated and saturated conditions (20.0 T, 30 kHz MAS).

Variable temperature (VT) ^1H spectra of SPEEK-GO composites showed a similar response to both hydration and long-term MAS. As an example, the VT ^1H spectra of SPEEK 1 wt% GO composite membrane is shown in **Figure 5.4**. The dried sample shows the expected broad, aromatic peak from its backbone hydrogen sites, while its acidic peak seems now to consist of two (or more) sites, centred between 7.9 and 7.7 ppm. The small amount of doping, and the mismatched chemical shift, mean that the extra site is likely not caused by the dopant itself, but rather new, slightly different sites for acidic protons in the bulk polymer matrix created due to the presence of the dopant.

Peaks in SPEEK ^1H spectra between 9 and 6 ppm are routinely assigned to acidic protons in different chemical environments, sometimes being correlated to membrane wetness (λ , the ratio of water molecules to acidic sites) or water uptake.³⁰

Hydrating the membrane causes the familiar shift of the acidic proton site peak to lower frequency, landing at ca 6.9 ppm in this case as seen in **Figure 5.4A**. As temperature increases this resonance shifts minimally towards higher frequency, but a much larger shift is seen after holding the membrane at a maximum temperature of 60 °C overnight. The overnight spectrum resembles very closely the dehydrated spectrum from the start of the VT study, and cooling the sample back to 30 °C shows that significant hysteresis has occurred (see **Figure 5.4B**), most likely due to permanent water loss within the rotor due to rapid MAS at elevated temperature.

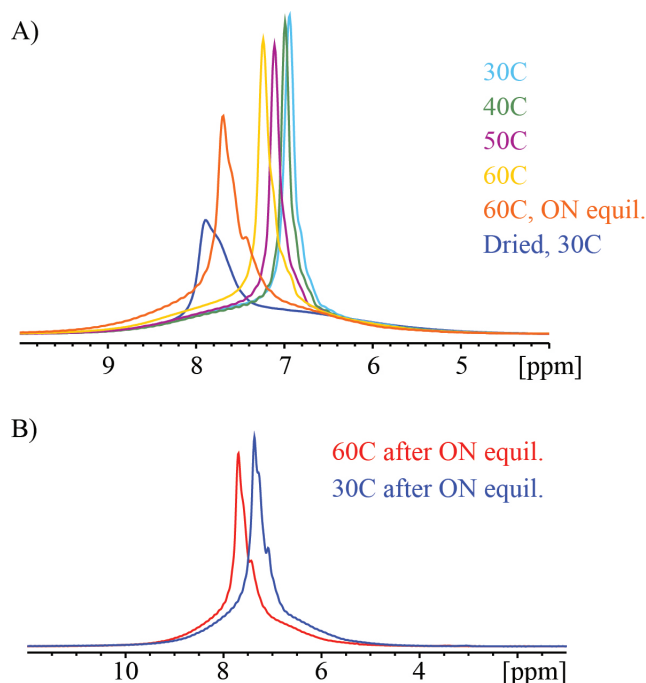


Figure 5.4: A) VT ^1H Hahn echo spectra of SPEEK-1 wt% GO composite membrane. B) A comparison of ^1H spectra of SPEEK-1 wt% GO composite at 60 and 30 °C after overnight high temperature MAS (20.0 T, 30 kHz MAS).

Considering that the water content of fully hydrated membranes was clearly changing during VT analysis, an attempt was made to examine the temperature response of

dried membranes and membrane composites. For clarity of comparison, pure SPEEK membranes as well as the high performance (1 wt%) and low performance (5 wt%) composites were the focus of this part of the study.

Figure 5.5 shows the ^1H VT spectra of SPEEK and its composites with GO and PGO under dehydrated conditions. The relatively sharp peak at ca. 2.5 ppm seen in these spectra is assigned to residual DMSO from the casting process. In an attempt to monitor changes to the mobility of the acid site protons absent the chemical shift-changing coalescence with water available under hydrated conditions, the width at half-maximum intensity (full width at half height, FWHH) is measured for the acidic peak, the results also being included in **Figure 5.5**. Peak width is directly related to the spin-spin relaxation rate in the rotating frame (T_2^*), which decreases with site mobility causing broader peaks, and so this metric may serve to identify composites with higher than usual acid site mobility in the relatively stationary dehydrated state.

The acid site line width analysis shown in **Figure 5.5A** for pure SPEEK shows a significant increase (ca. 30 %) at higher temperatures, counter to the intuition that higher temperatures would increase site mobility. It is possible that this observation is due to water loss caused by increased temperatures or MAS. Considering the poor site resolution, however, it is also possible that there is no significant change in the line width over this temperature range, and the measured difference comes from difficulty in modelling two poorly resolved sites.

Figure 5.5B shows that the acid site line widths of dehydrated SPEEK-GO composites are markedly different from those of pure SPEEK. This is particularly evident at lower temperatures, where composite acid site lines are significantly broader. Proton conductivity under these conditions is likely to be poor in any case, and so this broadening likely would not be caused by a change in proton mobility. Rather, the broadening

may be due to sample inhomogeneity due to the presence of GO dopants. Proton sites near in space to dopants would experience slightly different relaxation thanks to the nearby presence of foreign, electronically conductive material, causing a broadening of the range of similar chemical shift environments. A slight downward trend in line width is seen at higher temperatures, especially apparent in the 5 wt% GO spectrum. This likely is due, at least in part, to the experimental error mentioned above, but increased water presence with dopant addition may allow for greater water retention at higher temperatures and MAS rates, allowing the dynamics of the acid site under these conditions to display more clearly the expected change in mobility. The line width analysis results for PGO composites seen in **Figure 5.5C** show the largest line widths in this study: the width of the acid site in the 5 wt% PGO composite being between 4 and 6 times wider than that of pure SPEEK under varying conditions. As is evident from the spectra themselves, the intensity of the acid site is very low, likely exacerbating the difficulty in the modelling process of this site. The 1 wt% composite spectrum shows the expected response to VT line width analysis. In general the acid site is broader due to inhomogeneity, and the site narrows at increasing temperature due to increased mobility, made possible by improved water retention at higher temperatures due to doping.

A clear correlation between dehydrated acid site mobility and proton conductivity at higher %RH is not present in these samples. The dehydrated spectra do not seem to accurately represent how the same material will perform when saturated with water, while hydrated samples become dehydrated during analysis due to elevated temperature or MAS. The amount of water in the membrane samples must be carefully controlled in order to extract useful EIS and ssNMR results from these materials.

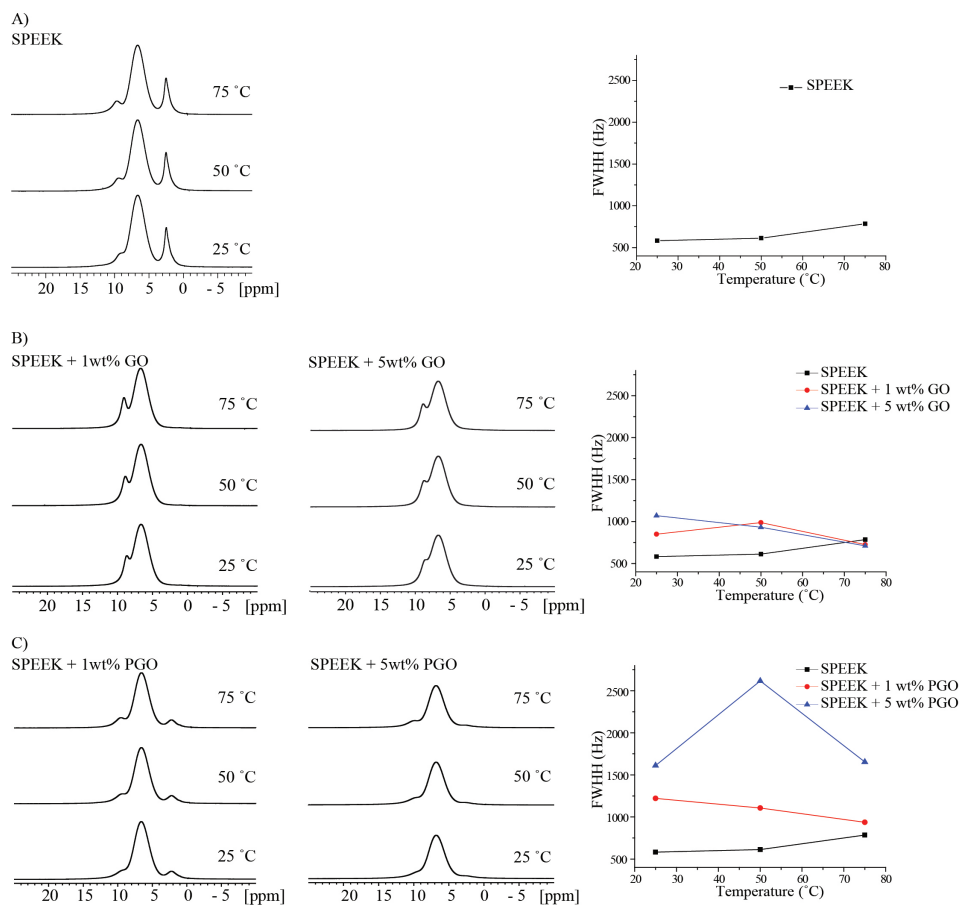


Figure 5.5: VT ^1H Hahn echo spectra and acidic peak line width responses to increasing temperature for dehydrated A) SPEEK, B) SPEEK-GO composites, and C) SPEEK-PGO composites (20.0 T, 40 kHz MAS).

5.3.3 High Temperature, Low %RH Conditions

The second half of this investigation involved applying EIS and ^1H ssNMR to SPEEK and its composites with GO and PGO under lower %RH conditions (i.e. 70 - 90 %RH) in an attempt to solve the issues of excess hydration observed in the previous half of the study. Higher temperatures were also used for this investigation where possible, as it was observed that the composite membranes would retain their solid phase at higher temperatures when the %RH was low. Membranes with 1 and 2.5 wt% dopant were generally used in this study. Samples which showed measurable proton conductivity are focussed on primarily here: there were several measurements at low %RH where

conductivity was too low to measure, and certain high temperature / %RH measurements where self-dissolution became apparent, and these cases are only mentioned as necessary for the sake of clarity.

5.3.3.1 EIS at Operational Conditions

Figure 5.6 shows the response of proton conductivity to increasing temperatures for SPEEK and composites made with GO and PGO. In all cases but one, proton conductivity was only measurable at 90 %RH, the exception being the 1 wt% PGO sample, which showed measurable (albeit comparatively low) proton conductivity at certain temperatures and 80 %RH. Below this operational range, it is likely that not enough water has been absorbed into the polymer matrix (doped or pure), and so the hydrophilic channels which conduct protons are not sufficiently inflated with water to provide a membrane-wide ion conduction network. Higher temperatures also caused a loss of measurable conductivity in many samples, either due to the baking out of water or due to the onset of sulfuric acid precipitation and membrane degradation. These cases are recorded as having 0 conductivity (i.e. immeasurable) for the sake of figure continuity.

Pure SPEEK appears to have a rather narrow operational window at 90 %RH, only displaying conductivity between 60 and 70 °C. The slightly lower conductivity seen at higher temperature, coupled with the survival of the solid membrane after testing, would seem to indicate that the lack of conductivity at higher temperatures is primarily due to water loss, indicating that pure SPEEK is a poor retainer of water under these conditions. Doping with GO causes significant changes in both the magnitude of proton conductivity and effective temperature range of the composite membranes. The 1 wt% GO composite showed a significant decrease in overall conductivity compared to the pure membrane,

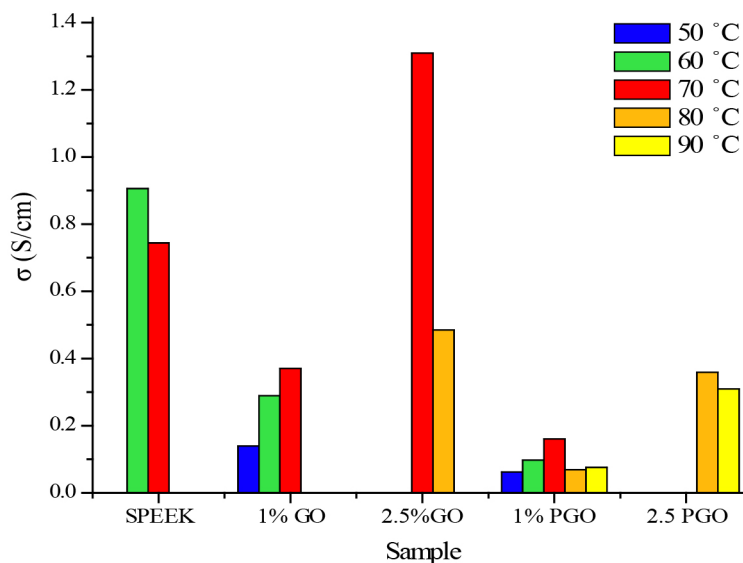


Figure 5.6: Proton conductivities (σ in S/cm) measured with EIS at increasing temperatures for SPEEK and SPEEK-GO and -PGO composites at 90 %RH.

however conductivity was measurable over a broader temperature window. The 2.5 wt% membrane showed significantly higher conductivity than the pure membrane at certain temperatures, and the operational window was shifted to higher temperatures. Neither of these membranes self-dissolved at higher temperatures, and so closing of the hydrophilic channels due to water loss is proposed as the reason for the loss of conductivity at higher temperatures.

A similar pattern is noted for the SPEEK-PGO composite membranes regarding a change in the operational window of these materials for proton conductivity. This is particularly evident for the 1wt% PGO composite, which showed measurable proton conductivity from 50 - 90 °C at 90 %RH and very low conductivity even at 80 %RH. The reduction in bulk conductivity when compared to pure SPEEK may be the result of a negative effect the presence of dopant material has on the casting process: the formation of contiguous, non-terminating hydrophilic channels is somehow reduced in the presence of graphitic dopants. The formation process of SPEEK and other ionomer membrane materials is a point of significant research, and the success of the casting

process is known to be very sensitive to many experimental parameters (i.e. casting surface, solution composition, particle size of dopants, etc.).^{31, 32} It is unsurprising, then, that an innocuous difference in the casting formula could have major effects on the performance of the cast membrane. Once again, the higher concentration 2.5 wt% composite membrane shows increased performance over the pure membrane at higher temperatures.

Overall the addition of dopants has a negative effect on overall proton conductivity; a likely consequence of the addition of dopants to the casting solution causing poor formation of hydrophilic channels in the polymer matrix. Even so handicapped, the composite membranes show a remarkable ability to change the operational range of these membranes at unsaturated conditions. The 1 wt% composites show a significantly broadened temperature window (especially in the case of the PGO composite). 2.5 wt% composites show measurable conductivity at higher temperature, likely due to a proliferation of the hydrogen bonding network within composite membranes between ionomer, water, and dopant, leading to an increased ability to retain water at high temperatures.

5.3.3.2 ¹H ssNMR at Operational Conditions

¹H Hahn-echo spectra of SPEEK and its composites, treated at 90 %RH and collected at VT, are shown in **Figure 5.7**. At high field and a relatively high MAS rate, the spectra show a number of extra sites when compared to the spectra in **Figure 5.3**. The broad aromatic peak now shows resolution between separate aromatic protons, as the MAS rate at this field was sufficient to reduce the dipolar coupling between proton sites in the backbone. The 30 °C spectrum for pure SPEEK seen in **Figure 5.7A** shows a number of proton sites spanning between 2 and 8 ppm. The most intense peak, at ca. 5.7 ppm

in the 30 °C spectrum, shifts significantly to higher frequency at elevated temperatures, landing at ca. 6.6 ppm when heated to 80 °C. It is fair to assume, considering its chemical shift mobility, that this peak represents acidic protons, while the other peaks, which shift only slightly with increasing temperature, represent structural aromatic protons. The poor resolution between these sites precludes a proper site assignment, however selective deuteration or more complex decoupling methods may assist with that goal. Very little hysteresis is seen after the sample is heated to 80 °C and brought back down to ambient conditions, indicating little or no water loss through the course of the VT experiment. However, there is little spectroscopic difference evident in these 1D spectra between the low and high temperature conditions (where the membrane is ion-insulating according to EIS) and the 60 - 70 °C samples, which possess measurable proton conductivity.

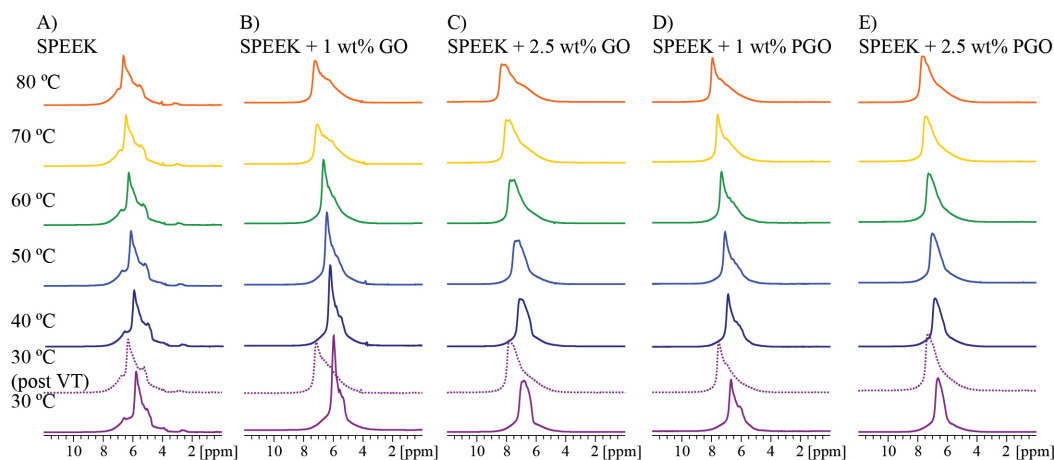


Figure 5.7: VT ^1H Hahn echo spectra of A) SPEEK, B) SPEEK-1wt% GO, C) SPEEK-2.5wt% GO, D) SPEEK-1wt% PGO, and E) SPEEK-2.5wt% PGO (20.0 T, 40 kHz MAS). Temperature is consistently colour-coded, from low (30 °C, violet) through medium (60 °C, green) to high (80 °C, red), while the dotted violet spectra were taken at 30 °C after the VT run to check for permanent changes.

A similar trend is noted for the VT spectra stacks of composite membranes shown in **Figure 5.7B-E**: the most intense peak in the 30 °C spectrum is also the most mobile as a response to increasing temperature, and little hysteresis is seen after the VT run, indicating a heightened ability to retain water. An exception is the 1% GO composite,

which has an unusually large acidic proton peak in the low temperature spectra which does not re-intensify after the VT experiments. It is possible that the severe hysteresis seen in the saturated VT runs (*vide supra*) came mainly from highly labile water, which may be the most significant contributor to the proton conductivity seen in the high %RH measurements in the previous section. It seems clear now that high temperature MAS (i.e. 40 kHz MAS rate in a 1.9 mm diameter rotor) has a measurable dehydrating effect on these materials. Even under lower %RH conditions, this means that the ion dynamics at operational conditions would be difficult to deconvolve from effects of MAS centrifugal high temperature water loss. Different reactions to MAS are noted using a larger rotor and spinning at a lower MAS rate (*vide infra*).

The ambient temperature (30 °C) ^1H Hahn echo spectra of SPEEK and its composites treated at conditions between 70 - 90 %RH are compared in **Figure 5.8**. Spectra recorded both before and after the VT run are shown in order to clarify the effect of high temperature MAS on water within the samples. Pure SPEEK treated at 70 %RH shows at least four acidic sites ranging from 7.2 to 6.4, indicating that at this temperature and hydration level these sites are too chemically isolated to perform rapid exchange and cause site coalescence. As %RH is increased, the individual site resolution is lost, and the main acidic peak shifts to lower frequencies as the acidic protons spend more time in a liquid water-like state. The small peaks seen in the 90 %RH spectrum at ca. 6.7 and 5.2 ppm may represent aromatic protons in the PEEK backbone, visible due to very high mobility and MAS rate causing a reduction in dipolar coupling (NB: the broad, low intensity resonance seen in nearly all spectra in **Figure 5.8** is assigned to immobile aromatic protons in the backbone). The spectra recorded after the VT analysis of SPEEK happen to show only moderate changes compared to their pre-VT spectra. Site resolution in the 70 %RH sample is lost after high temperature treatment, but the

bulk of the now poorly resolved site manifold have not shifted much on the ppm scale. Similar observations can be made of the spectra for higher %RH treated SPEEK membranes: the 90 %RH spectra matching nearly identically before and after the VT run. This would seem to indicate that, for pure SPEEK membranes, water loss is minimal during high MAS VT runs when the samples are not saturated with water, which stands in contrast to the results in **Figure 5.4** for saturated samples.

SPEEK-GO composites with 1 and 2.5 dopant wt% are also compared before and after VT runs through ^1H Hahn echo spectra in **Figure 5.8**, and a similar trend is noted to that found in pure SPEEK. The sharp acidic peak at ca. 6.6 ppm seen in the 70 %RH spectrum of the 1 wt% GO sample before VT treatment shifts towards a more water-like state as humidification is increased, landing at 6.0 ppm at 90 %RH. Additional peaks seen in these spectra are likely caused by chemically isolated acidic sites (in the case of the intense peaks in the 70 and 80 %RH spectra) or mobile aromatic backbone protons (in the 90 %RH spectrum). Increasing the GO dopant concentration serves to broaden all peaks significantly as a result of increased sample inhomogeneity, and so the spectra exhibit poorer site resolution for the 2.5 wt% sample. The post-VT spectra show very clearly that significant water loss occurs for these samples during high temperature MAS. The same loss in site resolution is noted here that was observed for the pure SPEEK sample, and in addition the main acidic water peak shifts to higher frequencies, from 6.0 to 7.2 ppm in the most extreme case. This high frequency shift indicates that a loss of water is leading to slower acid - water exchange and reduced site coalescence between acid and liquid water sites. This effect seems less severe in samples treated at lower %RH, matching with the observations noted for saturated samples in the previous section.

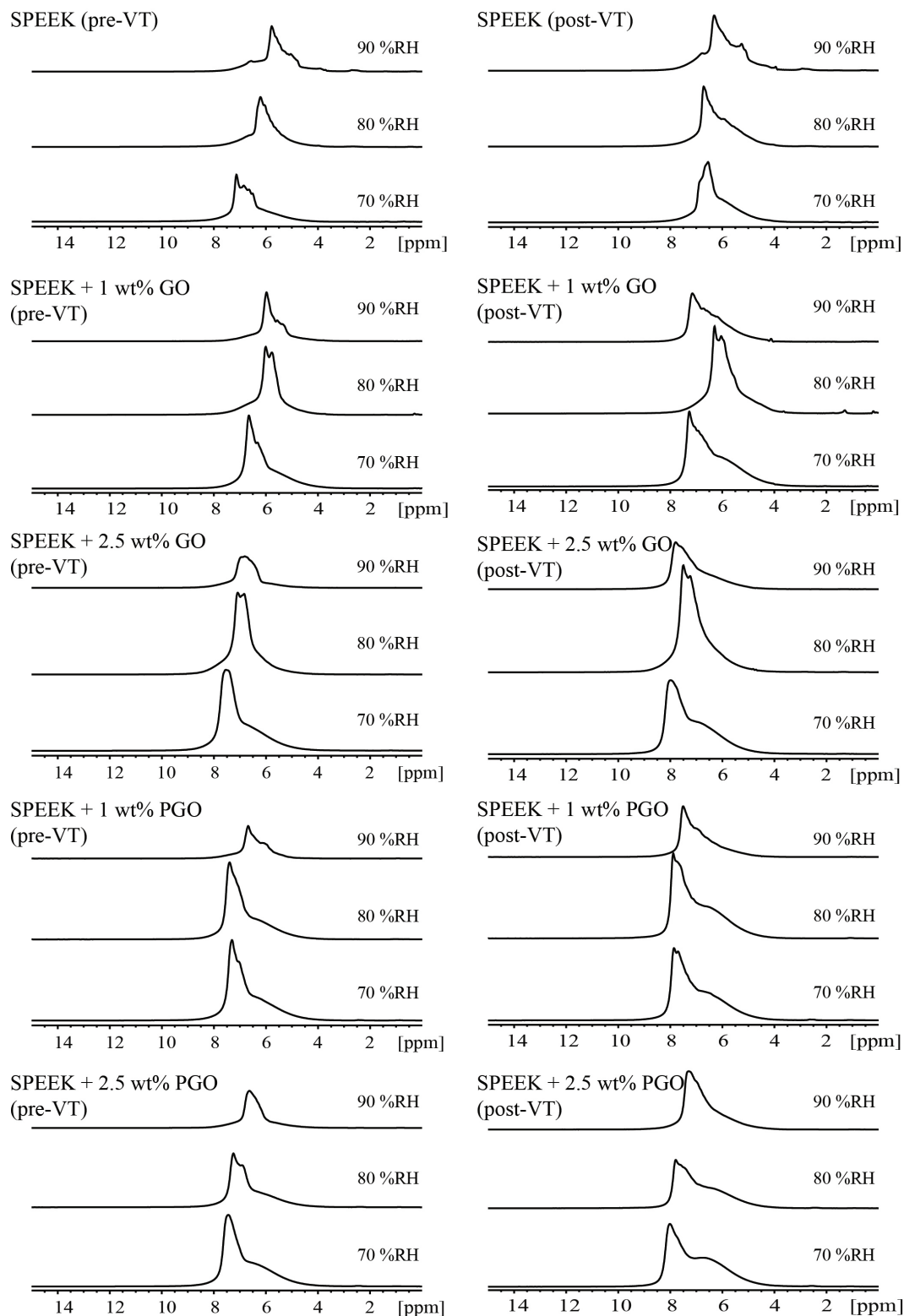


Figure 5.8: ^1H Hahn echo spectra of SPEEK and its composites with GO and PGO treated between 70 and 90 %RH, before and after the VT analysis shown in **Figure 5.7** (20.0 T, 40 kHz MAS).

An interesting departure from the norm is noted for the spectra of SPEEK-PGO composites, where acidic groups are present in the dopant material. The same acidic water sites are noted in the pre-VT ^1H spectra, where multiple isolated sites may be present at lower %RH (e.g. at 7.0 and 7.4 ppm in the 70 %RH spectrum of the 1 wt% PGO sample) and resolved aromatic backbone sites are evident at higher %RH (e.g. at 6.0 ppm in the 70 %RH spectrum of the 1 wt% PGO sample). With an increased dopant concentration, site resolution is once again negatively effected due to sample inhomogeneity. While further loss of site resolution is noted after the VT run, the main acidic peak in the higher %RH samples does not shift to higher frequency (relative to the lower %RH samples) as it did for the GO composites. For example, the difference in the chemical shift of the main acidic peak for the pre-VT 1 wt% GO samples between samples treated at 70 and 90 %RH is -0.75 ppm, compared to a shift of -0.15 ppm for the same peaks post-VT treatment. The shift between the same sites for the 1 wt% PGO samples is -0.5 ppm pre-VT and -0.55 post-VT. This would seem to indicate that the acidic groups in the PGO dopant serve to bolster the hydrogen-bonding network within the membrane, allowing it to retain significantly more water under high temperature and fast MAS. This observation helps to explain the ability of these dopants to increase the operational temperature range of composite membranes to higher temperatures, where better reaction kinetics are available, without baking out the water necessary to conduct protons on a macroscopic scale.

5.3.3.3 Low MAS rate ^1H ssNMR

In an effort to reduce the complexity of the ^1H spectra of these materials, high-temperature spectra were collected at 90 %RH conditions, the results of which are shown in **Figure 5.9**. Spectra were collected in a 7.0 T field with a 10 kHz MAS rate. In all

spectra, the fine structure afforded by the rapid MAS rate and higher field used previously is reduced significantly. The spectrum for pure SPEEK shows multiple, poorly resolved proton sites from ca. 6.8 to 6.4 ppm, all of which likely represent acidic water in different ionomer environments. A high-frequency shoulder at ca 7.1 ppm may represent anhydrous or poorly hydrated ionomer acid sites. A sample spectrum of PEEK is included in **Figure 5.9**, which consists of a weak, broad signal centred about 6.0 ppm, which is assigned to the backbone aromatic proton manifold. The difference in ^1H signal intensity between PEEK and its sulfonated form shows that the majority of signal intensity in spectra of SPEEK and its composites can be safely assigned to water - acid site coalescences. ^1H Hahn echo spectra of SPEEK composite, also shown in **Figure 5.9**, all show a loss in acid site resolution compared to pure SPEEK, possibly due to sample inhomogeneity.

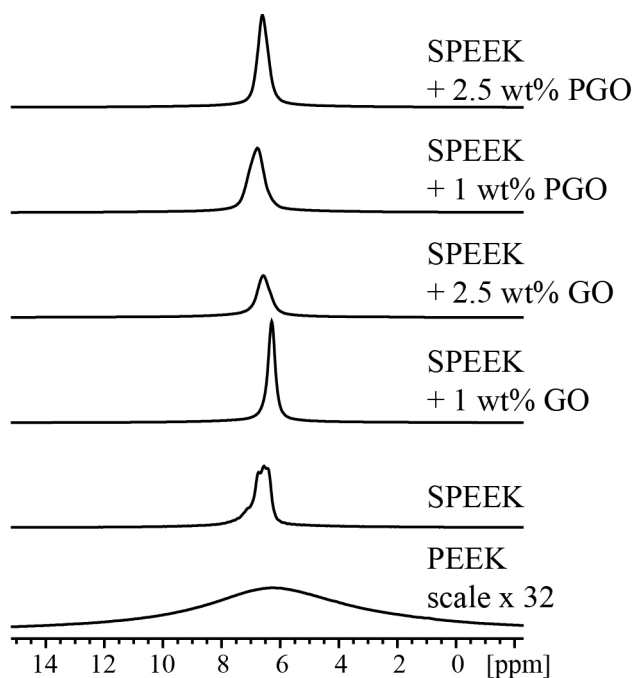


Figure 5.9: ^1H Hahn echo spectra of SPEEK and its composites with GO and PGO treated at 60 °C at 90 %RH at low field and MAS rate (7.0 T, 10 kHz MAS)

The peak centres span a small range from 6.75 to 6.25 ppm, with FWHHs between ca. 100 and 200 Hz. All of these resonances can be reasonably assigned to the acidic site in SPEEK, however samples at this temperature did not show appreciable proton conductivity through EIS. Higher temperatures could easily be achieved through VT ssNMR, and this would likely be a productive step forward, but concerns quickly arise regarding water loss at these elevated temperatures as we observed in the previous section.

5.3.4 WU%

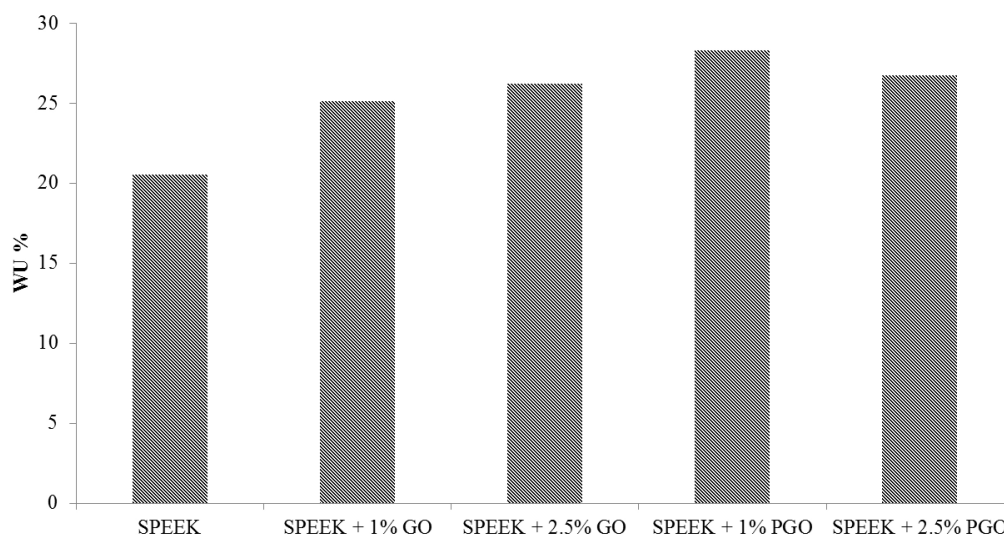


Figure 5.10: Water uptake percentages (WU%) for SPEEK and its composites with GO and PGO after treatment at 60 °C at 90 %RH.

Figure 5.10 shows the results of the water uptake experiments performed on SPEEK and its composite membranes containing GO and PGO. The WU% values for pure SPEEK, and composites with 1 wt% GO, 2.5 wt% GO, 1 wt% PGO, and 2.5 wt% PGO were 20.5, 25.1, 26.2, 28.3, and 26.7 %, respectively. The addition of dopant materials with acidic or hydrogen bonding surface groups appears to have a marked positive effect on membrane water uptake in all cases. No clear correlation between

the amount of dopant added and the increase in WU% can be drawn from this data: the trend seems to correlate directly in the case of GO and indirectly in the case of PGO dopants, however this observation could be due to the small wt% range under investigation. Higher WU% also correlated with improved proton conductivity at lower ambient %RH (vide supra). These results echo previous studies, where an improvement in the hydrogen bonding network between ionomer matrix, water, and dopant material hydrogen bond donors / acceptors leads to an increased ability of the material to hold onto water.^{7, 33, 34} Increasing dopant concentration in an attempt to further this effect would eventually lead to a contiguous electron-conducting (rather than ion conducting) pathway through the membrane, making the material unusable in a PEM-FC as the electrolyte. Electronically conductive ionomer composites may find use in the catalyst layers of a fuel cell, however, and so high wt% composites are not necessarily useless.

5.4 Conclusion

Composite membranes of SPEEK and varying wt% of GO and PGO were synthesized and analysed through EIS and ssNMR under a wide array of environmental conditions. When fully saturated with water, composite membranes displayed significantly higher proton conductivity than pure SPEEK membranes at certain dopant loadings, but it was noted that higher dopant concentrations caused reduced conductivities, likely due to interference with the formation of hydrophilic channels in the polymer matrix. It was also noticed that severe water loss was occurring during high temperature and high MAS ¹H ssNMR spectral acquisition, and so any dynamics information interpreted from these experiments may have been influenced by the effect of water leaving the membrane. EIS measurements taken at 90 %RH show that the addition of dopant materials may have a

moderately negative effect on overall proton conductivity, while broadening the effective range (with respect to temperature and humidity) over which proton conductivity can be recorded. This is likely due to an increased ability of composite membranes to retain water as a result of increased hydrogen bonding between liquid-like water, surface acid / hydroxide groups in the dopant, and acidic groups in the polymer matrix. Low-humidity ^1H NMR of composite membranes shows less severe water loss as a result of high temperature MAS, but indicates that dopants with acidic groups are more able to retain water for their parent ionomer matrices than those without, perhaps indicating that a stronger hydrogen bonding network is present in acidic dopant samples.

References

- [1] Mauritz, K. A.; Moore, R. B. *Chem. Rev.* **2004**, *104*(10), 4535–4586.
- [2] Zawodzinski, T. A.; Derouin, C.; Radzinski, S.; Sherman, R. J.; Smith, V. T.; Springer, T. E.; Gottesfeld, S. *J. Electrochem. Soc.* **1993**, *140*(4), 1041–1047.
- [3] Sone, Y.; Ekdunge, P.; Simonsson, D. *J. Electrochem. Soc.* **1996**, *143*(4), 1254–1259.
- [4] Savadogo, O. *J. Power Sourc.* **2004**, *127*(1-2), 135–161.
- [5] Sambandam, S.; Ramani, V. *J. Power Sourc.* **2007**, *170*(2), 259–267.
- [6] Peighambaroust, S.; Rowshanzamir, S.; Amjadi, M. *Int. J. Hydrogen. Ener.* **2010**, *35*(17), 9349–9384.
- [7] Ye, G.; Hayden, C.; Goward, G. *Macromolecules* **2007**, *40*(5), 1529–1537.
- [8] Mishra, A. K.; Kim, N. H.; Jung, D.; Lee, J. H. *J. Memb. Sci.* **2014**, *458*, 128–135.
- [9] Qu, B.; Ma, C.; Ji, G.; Xu, C.; Xu, J.; Meng, Y. S.; Wang, T.; Lee, J. Y. *Adv. Mater.* **2014**, *26*(23), 3854–3859.
- [10] Lee, J. K.; Smith, K. B.; Hayner, C. M.; Kung, H. H. *Chem. Comm.* **2010**, *46*(12), 2025–2027.
- [11] Li, Y.; Sheng, K.; Yuan, W.; Shi, G. *Chem. Comm.* **2013**, *49*(3), 291–293.
- [12] Eda, G.; Fanchini, G.; Chhowalla, M. *Nature Nanotech.* **2008**, *3*(5), 270.
- [13] Tateishi, H.; Hatakeyama, K.; Ogata, C.; Gezuhara, K.; Kuroda, J.; Funatsu, A.; Koinuma, M.; Taniguchi, T.; Hayami, S.; Matsumoto, Y. *J. Electrochem. Soc.* **2013**, *160*(11), F1175–F1178.
- [14] MacIntosh, A. R.; Harris, K. J.; Goward, G. R. *Chem. Mater.* **2015**, *28*(1), 360–367.
- [15] Cao, Y.-C.; Xu, C.; Wu, X.; Wang, X.; Xing, L.; Scott, K. *J. Power Sourc.* **2011**, *196*(20), 8377–8382.
- [16] Jiang, Z.; Zhao, X.; Manthiram, A. *Int. J. Hydrogen Energ.* **2013**, *38*(14), 5875–5884.
- [17] Tseng, C.-Y.; Ye, Y.-S.; Cheng, M.-Y.; Kao, K.-Y.; Shen, W.-C.; Rick, J.; Chen, J.-C.; Hwang, B.-J. *Adv. Ener. Mat.* **2011**, *1*(6), 1220–1224.
- [18] Langer, J.; Smiley, D.; Bain, A.; Goward, G.; Wilkening, M. *J. Phys. Chem. C* **2016**, *120*(6), 3130–3138.
- [19] Smiley, D. L.; Davis, L. J.; Goward, G. R. *J. Phys. Chem. C* **2013**, *117*(46), 24181–24188.
- [20] Smiley, D. L.; Goward, G. R. *Chem. Mater.* **2016**, *28*(21), 7645–7656.

- [21] Reeve, Z. E.; Pauric, A. D.; Harris, K. J.; Goward, G. R. *J. Phys. Chem. C* **2015**, *119*(48), 26840–26848.
- [22] Key, B.; Morcrette, M.; Tarascon, J.-M.; Grey, C. P. *J. Am. Chem. Soc.* **2010**, *133*(3), 503–512.
- [23] De Almeida, N. E.; Harris, K. J.; Samoson, A.; Goward, G. R. *J. Phys. Chem. C* **2016**, *120*(36), 19961–19969.
- [24] Yan, Z. B.; Brouwer, D. H.; Goward, G. R. *Macromolecules* **2016**, *49*(19), 7331–7339.
- [25] Ye, G.; Janzen, N.; Goward, G. *Macromolecules* **2006**, *39*(9), 3283–3290.
- [26] De Almeida, N.; Goward, G. *ECS Trans.* **2014**, *64*(3), 425–432.
- [27] Hummers Jr, W. S.; Offeman, R. E. *J. Am. Chem. Soc.* **1958**, *80*(6), 1339–1339.
- [28] Oger, N.; Lin, Y. F.; Labrugère, C.; Le Grogneq, E.; Rataboul, F.; Felpin, F.-X. *Carbon* **2016**, *96*, 342–350.
- [29] Wang, Y.; Yang, D.; Zheng, X.; Jiang, Z.; Li, J. *J. Power Sourc.* **2008**, *183*(2), 454–463.
- [30] Xing, P.; Robertson, G. P.; Guiver, M. D.; Mikhailenko, S. D.; Wang, K.; Kaliaguine, S. *J. Memb. Sci.* **2004**, *229*(1-2), 95–106.
- [31] Holdcroft, S. *Chem. Mater.* **2013**, *26*(1), 381–393.
- [32] De Almeida, N. E.; Paul, D. K.; Karan, K.; Goward, G. R. *J. Phys. Chem. C* **2015**, *119*(3), 1280–1285.
- [33] Zuo, C.; Dorris, S.; Balachandran, U.; Liu, M. *Chem. Mater.* **2006**, *18*(19), 4647–4650.
- [34] Seland, F.; Berning, T.; Børresen, B.; Tunold, R. *J. Power Sourc.* **2006**, *160*(1), 27–36.

6 — Natural Abundance NMR Spectroscopy of Nitrogen-Doped Carbon Black

This chapter presents as-yet unpublished work done in cooperation with an industry collaborator in Burnaby, BC, Canada. Starting materials and various nitrogen-doped carbon black samples were provided by this collaborator and their team. Post-doping treatment, NMR spectroscopy, and spectral analysis were performed by the author. In an attempt to explore the positive influence of nitrogen doping on the effective lifetime of carbon-supported platinum catalysts used in automotive hydrogen fuel cell systems, solid-state NMR was employed to probe the difference (if any) between doped catalyst supports made from different carbon and nitrogen sources. ^1H spectroscopy showed a variety of sites present in the doped samples; some likely from residual starting material but others from novel sites within the doped catalyst supports. Double-quantum and 2D ^1H experiments were used to examine the structure of these catalysts, while ^{13}C CPMG experiments (see **Chapter 2**) revealed subtle differences in the nuclear relaxation rates of these materials, potentially related to their electronic conductivity. The results of the ssNMR analysis were insufficient to provide an unambiguous picture of the dopant sites within these carbon black samples; this was due in equal parts to the lack of isotopically labelled dopants, the effects of electronic induction and ring current shifts on data acquisition and analysis, and the broad array of different ^{13}C chemical shift environments present in the carbon black itself. While the data is still interesting spectroscopically, suggestions are made at the end of this chapter to expand upon the

lessons learned through this study to produce more useful results from similar samples in the future.

6.1 Introduction

Fuel cells are a burgeoning class of energy storage and application devices which produce useful currents via an electrochemical reaction which irreversibly consumes at least one reagent. There are many forms of fuel cells, which require different fuels and exploit different reactions, and all of them are complicated, delicate structures with multiple interconnected parts.¹⁻⁵ For instance, the polymer electrolyte membrane fuel cell (PEM-FC) stack, used in automotive applications and arguably the most successful form of the technology, is made of multiple cells, each featuring two gas diffusion layers (GDLs), current collectors, and catalyst coated membranes (CCMs), one for each electrode, as well as the titular PEM. One particularly important component is the CCM.⁶⁻⁸ This layer is responsible for adsorbing the fuel or oxidant gases ($\text{H}_2(\text{g})$ and $\text{O}_2(\text{g})$, respectively) from the GDLs, housing the hydrogen oxidation and oxygen reduction half-cell reactions (HOR and ORR), shuttling protons to and from the PEM layer, and transmitting electrons produced and consumed during the HOR and ORR to the current collectors for conductance through the working circuit.

To perform these functions simultaneously, the CCM is comprised largely of a carbon support with catalytic platinum nanoparticles, with a relatively small (ca. 10 wt.%) amount of ionomer, the same material which wholly makes up the PEM.⁹⁻¹¹ The nature of the interface between these materials is extremely important to fuel cell performance, since the interfaces between the three components of these layers represent compounding resistances to electrochemical performance. For example the amount of ionomer in

the CCM must be low and homogeneous, since a thick ionomer layer may cause high $\text{H}_2(\text{g})$ and $\text{O}_2(\text{g})$ gas diffusion resistance, blocking these reagents from reaching reactive sites in the catalyst. Too thin an ionomer layer, however, can have detrimental effects on H^+ conductivity between the CCM and PEM. The porosity and hydrophilicity / hydrophobicity of the carbon support can have a large effect on gas diffusion and reaction kinetics, also contributing to overall fuel cell efficiency. The catalytic platinum nanoparticle surfaces can have strong interactions with the ionomer, especially under dry conditions, and the level of metal oxidation can limit catalytic performance as well. All of these parameters may also be affected by how the CCM components interact with the solvent system used in the casting process, and so the properties of the casting solution (ionomer, catalyst + support, and solvent, referred to as the catalyst 'ink') are similarly relevant.¹²⁻¹⁵ With so many moving parts, and where subtle interactions can have significant effects on the CCM, it is unsurprising that this layer has many potential points of failure, and a significant amount of work has been done to address these issues.

Perhaps one of the most well studied of these problems is that of platinum catalyst poisoning and degradation. The activity of the catalyst, especially in the cathode layer where the kinetically less-favourable ORR occurs, has a dominant effect on fuel cell electrochemical efficiency compared to all other modifiable parameters.¹⁶⁻¹⁸ The platinum nanoparticles also interact with ionomer sulfonate groups in the CCM, particularly when the catalyst support is hydrophobic, which can have important effects on ionomer layer thickness and gas permeability.¹⁹ At the optimal environmental conditions for proton conductivity for NafionTM (the industry PEM conductivity benchmark), performance decreases are seen over time due platinum surface poisoning by carbon monoxide, a common $\text{H}_2(\text{g})$ fuel contaminant.²⁰⁻²³ Pt dissolution may occur during fuel cell discharge as well; platinum may migrate from the CCM to PEM where it no longer properly cat-

alyzes the HOR and ORR.²⁴⁻²⁷ These issues have a significant negative effect on fuel cell lifetime, and so a large volume of work has been committed to replacing platinum with a less expensive, more resistant metal or non-metal catalyst, or to stabilize and protect catalytic platinum in the CCM for extended usage.

One tactic used to increase platinum useful lifetime is to modify the carbon catalyst support through nitrogen doping. As mentioned in **Chapter 4** of this thesis, the systematic insertion of nitrogen atoms into the carbon catalyst support is generally achieved through pyrolysis of mixed carbon and nitrogen sources, or by treatment of carbon supports with nitrogen-containing gasses in a chemical vapour deposition-like process. The morphological effects of nitrogen doping have been well characterized through electron microscopy and X-ray spectroscopy, but the precise molecular-scale nature of the dopant sites and their interaction with the catalytic platinum surfaces is still under investigation.²⁸⁻³¹ It has been hypothesized that nitrogen doping introduces structural defects which are better anchors for platinum nanoparticles, helping to stave off dislodging and dissolution. Nitrogen dopant sites are also believed to promote the growth of smaller platinum nanoparticles, increasing the catalytic surface area per gram of platinum, and improving the electronic structure of the catalyst particles to further improve performance.³²⁻³⁴ For these reasons, the structure of these dopant sites, as well as the mechanisms for their formation, are important research avenues.

Solid-state nuclear magnetic resonance (ssNMR) spectroscopy has been successfully employed in similar situations to answer questions about atomic scale structure and dynamics. Despite the challenges associated with analyzing conductive materials in a strong magnetic field, ssNMR has been used to elucidate structure in graphene oxide, covalently modified graphene, and doped graphene / CNTs with extreme specificity.³⁵⁻³⁷ In the case of nitrogen doped graphene, the nitrogen dopant sites seem like an ideal

target for ssNMR analysis, however nearly all the nitrogen atoms on earth (99.636 %) exist as the ^{14}N isotope. This isotope is highly unreceptive to NMR analysis: it is a spin 1 nucleus which produces extremely broad signals due to quadrupolar internuclear interactions. In all but the simplest cases ^{14}N ssNMR is a disadvantageous analytical method, and where possible doping with ^{15}N enriched nitrogen sources is recommended. ^{15}N is not quadrupolar ($I = \frac{1}{2}$), and ^{15}N spectral lines tend to be relatively narrow and well resolved. This characteristic of ^{15}N was exploited in **Chapter 4** of this thesis, where a ^{15}N -doped precursor was used to produce N-doped graphene which was highly amenable to ssNMR analysis, producing informative spectra which accurately characterized dopant sites within this extremely relevant but uncooperative sample. Isotopic labelling of nitrogen precursors can quickly become expensive though, and so indirect ssNMR methods of analysis (i.e. using ^1H , ^{13}C , and other, more receptive nuclei) are in high demand for the study of these industrially relevant materials.

The purpose of this study was to analyze a number of nitrogen-doped carbon black samples, synthesized through pyrolysis of mixtures of various organic carbon and nitrogen sources, through ssNMR without resorting to expensive ^{15}N labelling. Multinuclear and multidimensional pulse sequences, focussing mainly on ^1H and ^{13}C , were used to analyze the reagents and products in these syntheses in an attempt to rationalize a synthesis mechanism and dopant site structure. Changes in spin-lattice and spin-spin (T_1 and T_2 , respectively) relaxation times can be used to monitor changes in the band gap structure of the carbon support, which has proven to be sensitive to doping as well. Through these means, ssNMR can be developed as an analytical tool for the study of highly amorphous, carbon based doped materials for the improvement of fuel cell-relevant catalysis at a low cost.

6.2 Experimental

6.2.1 Nitrogen Doping of Carbon Black Samples

Nitrogen-doped carbon black samples were generated through a proprietary method of thermal decomposition of nitrogen dopants in the presence of carbon supports. What follows is a generalized process, omitting important details for confidentiality purposes. Two carbon supports, Denka Black (oxidized small acetylene black, or OSAB) and Black Pearl carbon (BPC), and two dopants, melamine and 1-ethyl-3-methylimidazolium dicyanamide (EMIM-DCA, an ionic liquid, referred to as IL) were used to generate a total of four samples for this study. These samples are identified by both their carbon and nitrogen sources, labelled as follows: Denka black & melamine (D+M), Denka black & ionic liquid (D+IL), Black Pearl & melamine (BP+M), and Black Pearl & ionic liquid (BP+IL). The carbon supports were first dried under a stream of $N_2(g)$ at $300\text{ }^\circ\text{C}$ for > 16 hours. The dried carbon source was then mixed with the nitrogen dopant. Melamine and carbon were ball milled together for one hour, while ionic liquid and carbon were mixed together to form a thick slurry.

The carbon / dopant mixtures were transferred into ceramic crucibles within a tube furnace. The furnace was then sealed, evacuated, and refilled with $N_2(g)$, after which a constant flow rate of 0.3 L/min of $N_2(g)$ was applied to the sample. The temperature of the furnace was raised to $700\text{ }^\circ\text{C}$ at a rate of $5\text{ }^\circ\text{C/min}$, and held at maximum temperature for three hours. The material was then cooled to room temperature under ambient conditions, and ground into a fine powder with a mortar and pestle. Where necessary, the samples were dried in vacuo again at temperatures up to $120\text{ }^\circ\text{C}$ in order to remove adsorbed water or other volatile impurities.

6.2.2 Analysis

ssNMR spectra were collected on a Bruker Avance 500 spectrometer with a 2.5 mm H-X MAS solid state probe. Inductive effects in the electronically conductive samples were strong enough to cause difficulty in sample spinning and in tuning / matching the probe, so when necessary the samples were diluted with Teflon powder. ^1H and ^{13}C spectra were referenced to adamantane at 1.85 ppm and 38.5 ppm (high-frequency peak), respectively.

Thermogravimetric analysis was performed at a heating rate of 5-10 $^{\circ}\text{C}/\text{minute}$ in Argon using a TA instruments Q50 thermogravimetric analyzer.

6.3 Results & Discussion

Thermogravimetric analysis (TGA) was used to test the stability of the carbon supports at high temperature. The TGA curves for Denka (D) and Black Pearl (BP) carbon are shown in **Figure 6.1**. The curve for BP carbon shows little or no weight losses up to over 900 $^{\circ}\text{C}$, indicating that this material is stable at the pyrolysis temperatures used for nitrogen doping and that the material does not adsorb a significant amount of atmospheric water. D carbon is also stable up to higher-than-pyrolysis temperatures, however a weight loss of ca. 15 % is observed at roughly 100 $^{\circ}\text{C}$, likely to be caused by the removal of adsorbed water, indicating that the material is significantly hygroscopic before nitrogen doping. **Figure 6.1** also shows TGA curves comparing the carbon supports with their N-doped analogues: BP+M, BP+IL and D+IL (the curve for D+M was clearly anomalous, and is omitted). The doped samples show no uptake of atmospheric water; this is particularly evident for D+IL, which likely had its residual water removed by the pyrolysis process. The dotted lines seen in **Figure 6.1B and C** show that BP+M and

BP+IL begin to degrade ca. 50 and 150 °C lower than their pristine starting material, and D+IL begins to degrade ca. 100 °C earlier than D-Carbon. This propensity for all doped samples to degrade at slightly lower temperatures than the pristine carbon supports likely indicates the presence of expected ‘defect’ (i.e. nitrogen dopant) sites within the graphite structures.

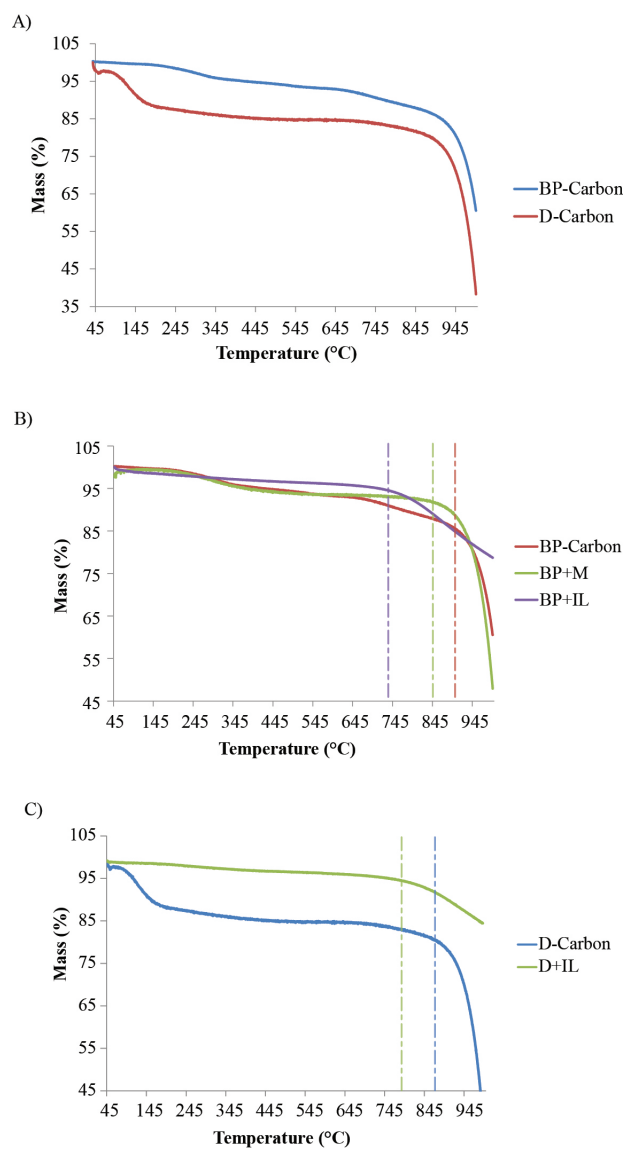


Figure 6.1: Thermogravimetric analysis (TGA) curves for carbon black precursors and N-doped samples. The curve for the D+M sample is omitted.

6.3.1 ^1H ssNMR Analysis

^1H Hahn-echo ssNMR spectra for as-received and dehydrated D-carbon and BP-carbon are shown in **Figure 6.2**. The as-received spectra both show a number of proton sites are present in this material, resulting in a highly overlapping manifold of peaks which is difficult to accurately deconvolve. Adding to the difficulty is the presence of significant ring current shifts due to the proximity of these proton sites to circulating π electrons within the graphitic sheets.³⁸⁻⁴⁰ The spectrum of as-received BP-carbon shows at least two sharp peaks at ca. -4.5 and -7 ppm, while the spectrum for D-carbon shows a very broad peak centred at ca. -8 ppm. Due to their chemical shift, and the fact that these sites are attenuated significantly by the dehydration process, it is evident these peaks represent adsorbed atmospheric water or solvents from their synthesis or post-synthesis washing. The amounts of these non-structural proton sites are significantly higher in D-carbon than in BP-carbon, matching closely with the conclusions produced by the TGA data. Both samples, however, have a peak at 6.5 - 7 ppm, which remains present even after heating in vacuo. It is likely this peak represents protons at the edges or defect sites of graphene-like sheets within the graphitic supports. Other possibilities include the presence of -OH groups or tightly hydrogen bonded water or solvent localized at the edges of graphitic sheets, explaining their higher than usual chemical shift. Dehydration does not seem to remove all of the non-structural protons from the carbon supports; BP-carbon is left with a significant amount of signal intensity between 0 and -10 ppm, and the broad, low-frequency signal seen in D-carbon is attenuated <50% by the dehydration process, an expected result reflecting the extremely high surface area and porosity of these carbon supports.

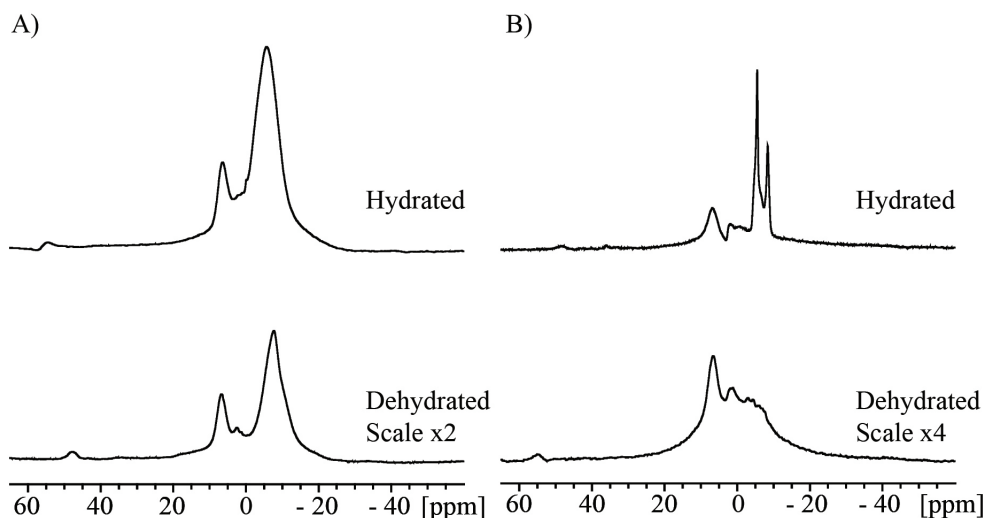


Figure 6.2: ^1H Hahn echo NMR spectra of A) D-carbon and B) BP-carbon, both as-received (hydrated) and after heating above $120\text{ }^\circ\text{C}$ in vacuo for 16 hours (dehydrated). Spectra taken at 11.7 T, 24 kHz MAS rate.

Figure 6.3 shows the ^1H Hahn-echo ssNMR spectra of dehydrated N-doped carbon samples. As-received samples of doped carbons were similar to the carbon supports, in that their spectra showed a number of proton sites from 5 to -10 ppm which likely arose from adsorbed water and were easily removed by heating in vacuo. The samples doped with melamine, D+M and BP+M, both predominantly feature the same high frequency peak shown by their carbon support precursors, centred at ca. 7 ppm. The peak broadens and changes its chemical shift very slightly upon N-doping, which may indicate a number of different responses to the process. The introduction of amine-bonded protons, for instance those belonging to dopant pyridinium or primary / secondary amine sites, would conceivably produce a proton peak in the same area as the carbon support structural proton at ca. 7 ppm, which would explain the broadening and shifting seen in the doped sample spectra. Heteroatomic doping of graphitic material is known to significantly effect the electronic band gap and conductivity of the carbon material as well as T_1 and T_2 relaxation times in similar cases, which could also explain this small change in the proton spectra. The N-doped samples produced with ionic liquid (BP+IL and D+IL)

also feature the structural proton site at ca. 7 ppm, but also feature a large broad signal spanning 30 ppm, particularly evident in the spectrum for BP+IL.

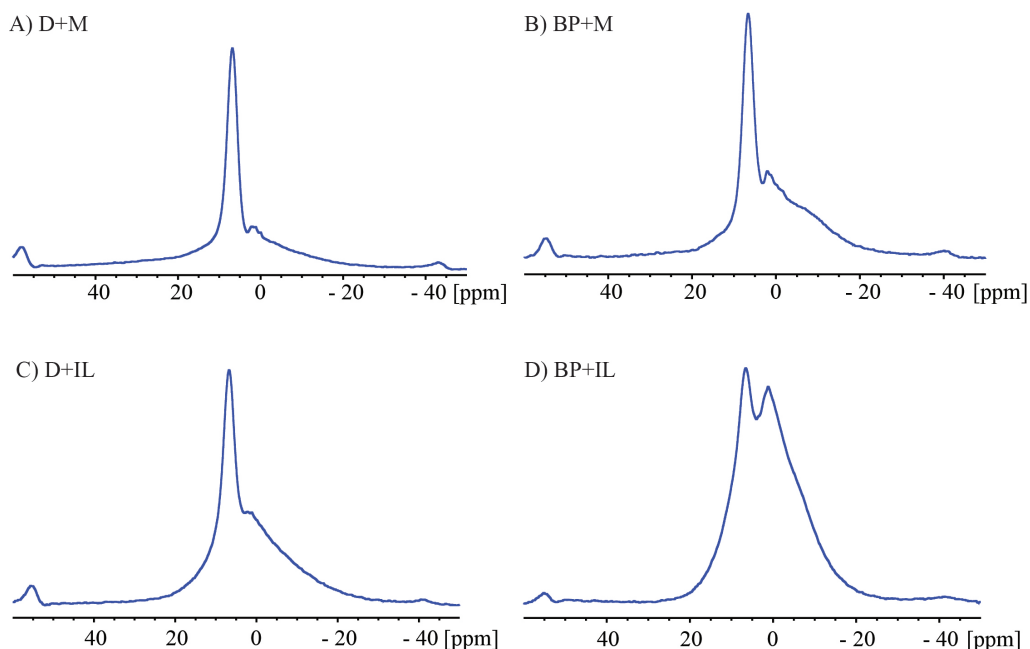


Figure 6.3: ^1H Hahn echo NMR spectra of dehydrated N-doped carbon black samples. A) Denka Black + Melamine, B) Black Pearls + Melamine, C) Denka Black + ionic liquid, D) Black Pearls + ionic liquid. Spectra taken at 11.7 T, 24 kHz MAS rate.

At this point it is safe to assume that the persistent ^1H signal found in all N-doped carbons is structural, and not caused by adsorbed solvents. The breadth of this signal and its location on the chemical shift scale (ca. 1550 Hz broad, between 6.8 and 6.6 ppm in all four cases), however, both make a positive assignment of this site non-trivial. The site is present in the starting carbon support material, so it is possible that no new structural protons are introduced by the doping processes used here. Protons nearby to nitrogen dopant sites in graphene have produced simulated and experimental peaks with proton shifts in the 7.4 to 6.5 ppm range, meaning that any newly-installed proton sites may have their signals obscured by the starting material peak.⁴¹

2D ^1H exchange spectroscopy (EXSY) spectra for starting materials and N-doped samples using long mixing times are shown in **Figure 6.4**, alongside stacks of 1D Back-

to-Back (BaBa) spectra with increasing recoupling times. The EXSY spectra are used to identify chemical exchange between protons sites, and longer mixing times were used in an attempt to visualize even very slow exchange. By contrast, the BaBa experiments are used to detect relatively weak homonuclear dipolar coupling in the kHz range. These two experiments are used here to measure the strength of the dipolar coupling that each proton site experiences (BaBa), as well as to identify any chemical proton exchange or magnetization exchange through the Nuclear Overhauser effect (EXSY). Both BP-carbon and D-carbon show their non-structural proton signals are still visible even out to recoupling times of 0.2 ms, while the structural proton site attenuates at shorter recoupling times. This observation is particularly clear in D-carbon. The structural proton sites within the starting materials show weaker couplings than the non-structural ones: this is shown by the attenuation of the structural site signal at short recoupling times and the persistence of the non-structural site signal at longer recoupling times. One explanation for this observation is that the structural site represents protons at the edges of graphite-like sheets, which are few and far between, while the non-structural proton sites represent solvent (likely water) which is concentrated in the pores of the carbon black. Plots of the integrated intensities of peaks from the BaBa experiments are shown in **Appendix Figure 1**. The undoped carbon signals, assigned to surface-adsorbed solvent species, were integrated from the 0 - -20 ppm region, while the structural signals from the doped samples were integrated from 20 - 0 ppm. The intensities at short recoupling times vary significantly, with undoped samples displaying more intense BaBa signals in general. Curiously, both samples doped with IL showed relatively higher signal intensity than those doped with melamine, perhaps indicating that these species are more mobile and not fully incorporated into the graphitic sheets of the carbon backbone. After ca.125 μ s, the BaBa intensities of all samples, doped or not, are nearly equivalent.

Oscillations in site intensity as recoupling times increase are likely due to problems with phasing the spectra, or the presence of multiple sites with different dipolar couplings.

The 2D EXSY spectra for the starting materials do not show any cross-peaks, indicating that no chemical exchange is observed between structural and non-structural protons, as expected by the relatively low chemical reactivity of sp^2 carbon-bound protons under normal conditions. There may be chemical or magnetic exchange between non-structural species at this temperature, but the signal-to-noise ratio (SNR) is too low to resolve individual cross-peaks between these sites. Some physisorbed solvent may be stationary and concentrated enough to exchange magnetization in the time scale of these EXSY experiments, and this may be the cause of the small off-diagonal signal intensity. These results are expected, since the structural protons in porous carbon are sparse, isolated, and not acidic. The stronger dipolar coupling seen in BP-carbon, as evidenced by the signal intensity at longer BaBa recoupling times, may indicate an increased concentration of structural protons around defect sites or pore edges. Functionally speaking, increased structural proton coupling may indicate smaller graphitic sheets, an increased number of pores, and increased surface area.

2D ^1H EXSY and BaBa stacks for the doped carbon samples are also shown in **Figure 6.4**. The EXSY spectra of all four modified samples do not show significant cross-peaks between any sites, while off-diagonal intensity may again be the result of concentrated adsorbed solvent interacting magnetically with solvent or structural proton sites. The BaBa experiments show that signals at positive ppm (i.e. structural sites) survive the double quantum filter out to relatively long recoupling times, while those at lower ppm shifts (i.e. adsorbed solvent) tend to attenuate more quickly. This is further evidence that the starting carbon black materials were better ordered and more able to trap solvent and keep it trapped, while the modified samples allow for much more mobile

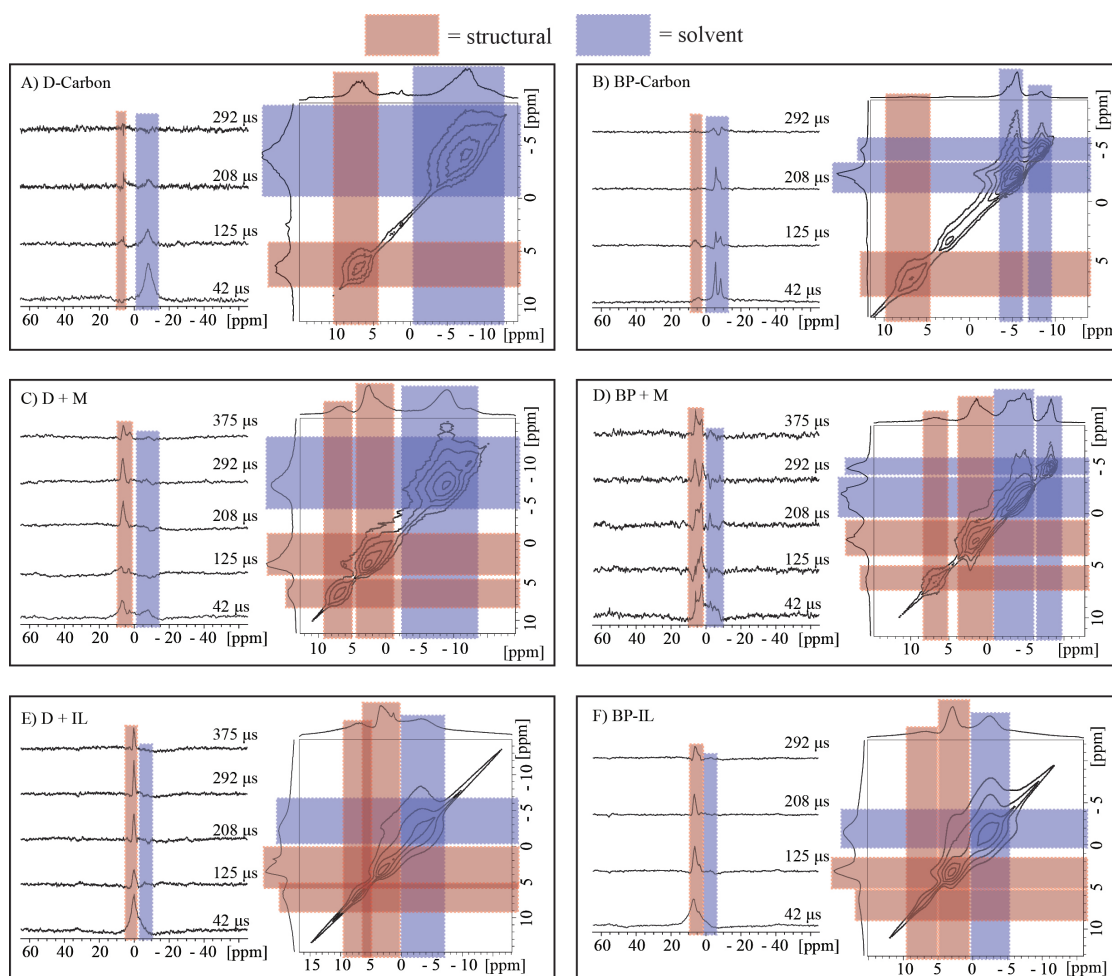


Figure 6.4: ^1H Back-to-Back (left) spectral stacks with ascending recoupling times (noted) and ^1H 2D EXSY spectra with mixing times of 10 ms for A) D-carbon, B) BP-carbon, C) Denka Black + Melamine D) Black Pearls + Melamine, E) Denka Black + ionic liquid, and F) Black Pearls + ionic liquid. Spectra taken at 11.7 T, 24 kHz MAS rate.

solvent molecules, evidenced by weaker dipolar coupling. This observation may be a result of a structural change in the graphitic sheets of the carbon black host, introduced by in-sheet heteroatomic nitrogen doping. The fact that the structural proton site is persistent at long recoupling times in the BaBa experiment indicates that the protons represented by this site are immobile and closely clustered together. This could be due to local concentrations of dopant sites around graphitic sheet defects or edges. Functionally speaking the BaBa results indicate an increased amount of structural protons which are near in space to one another, pointing towards dopant-site localized defects or decreased

sheet size from the doping process. The low SNR seen at long recoupling times in the BP+M sample may indicate that this combination produces fewer (or potentially more isolated) proton sites. The samples made with IL precursor have particularly high SNR at longer recoupling times which could conversely indicate that this dopant produces a greater number of dopant sites. The absence of cross-peaks in any of the EXSY spectra for doped samples indicates that these structural proton sites are non-acidic; an assertion supported by the BaBa spectra, in that a mobile proton would experience weak dipolar coupling and likely not produce a signal.

Without a positive assignment for these protons it is difficult to identify what functional groups (nitrogen based or otherwise) are present in these dopant sites, but considering their chemical shifts and the starting materials used, some possibilities are shown in **Figure 6.5**.

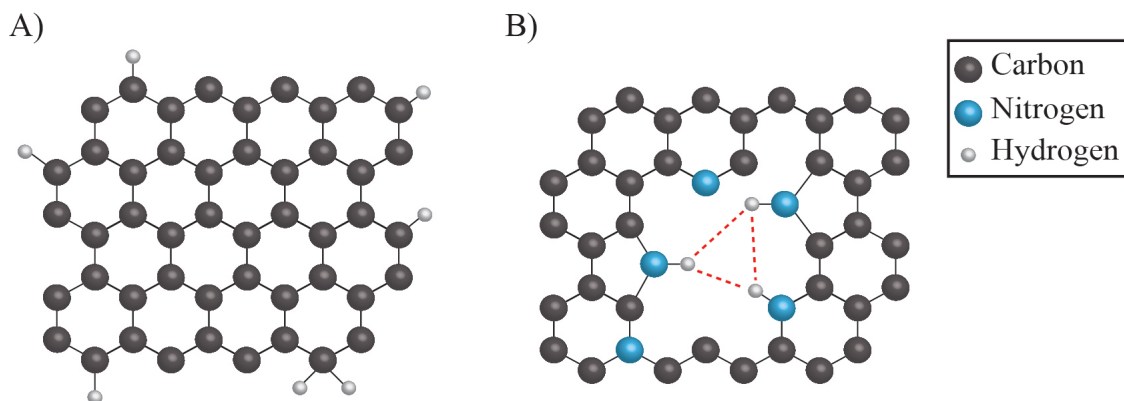


Figure 6.5: Illustrations of proton environments potentially found in carbon black and N-doped carbon samples which could produce the DQF spectra found in **Figure 6.4**. A) Edge based structural protons which are well isolated from one another and do not experience significant homonuclear dipolar coupling. B) Defect site dopant-based protons, as part of pyrrole or pyridinium groups, which are clustered together and close enough to experience dipolar coupling.

6.3.2 ^{13}C ssNMR Analysis

Direct ^{13}C spectra for D-carbon, BP-carbon and their N-doped analogues are shown in **Figure 6.6**. The Carr-Purcell-Meiboom-Gill (CPMG) signal enhancement technique was used in order to obtain a decent SNR in a reasonable amount of time. The CPMG sequence relies on a train of 180° pulses to impel magnetization to remain in the detectable x-y plane, and as such is severely effected by changes in the spin-spin relaxation times (T_2 and T_2^*). To keep the rapidly dephasing magnetizations coherent, this pulse train must be rotor-synchronized, i.e. each pulse-delay block in the train must fit within an integer multiple of the MAS rate. The CPMG pulse sequence is instructively illustrated in **Appendix Figure 2**. Individual echo times are limited by the T_2^* relaxation time of the sample, while the total echo time is limited by T_2 , both of which are extremely sensitive to electronic band gap, and therefore the structure and number of dopant sites in nitrogen-doped graphene.

Figure 6.6A shows that the ^{13}C spectra for D-carbon and BP-carbon are quite similar. Indeed, both samples produce a signal which is similar to any material consisting of mostly sp^2 -hybridized carbon atoms, including several examples in the preceding chapters of this thesis. The optimal SNR enhancement for these samples was obtained using a 500-pulse echo train at an echo time of 3.33 ms, for a remarkably long total acquisition time of roughly 3 seconds. This indicates extremely slow T_2 relaxation, which is to be expected for a largely homogeneous sample without impurities or defects, i.e., where there are little chances for spin exchange between spin systems. The lower SNR seen in the spectrum for D-carbon may indicate that this sample is less ordered or pure than BP-carbon. The difference in SNR between these two samples despite identical experimental parameters and nearly equal sample sizes are attributed to differences in

electronic band gap structure and conductivity, caused by a differing number of defects or impurities, noted to have a strong effect on NMR relaxation parameters.⁴² Calculated T_2 values are shown in **Table 6.1**. The measured T_2 values for the two starting carbon materials are 11.0 ms for D-carbon and 42.7 ms for BP-carbon. The broad signal spans from 160 to 80 ppm, centred roughly at 120 ppm. This site represents a wide array of nearly identical sp^2 -hybridized carbon sites expected from carbon black samples.

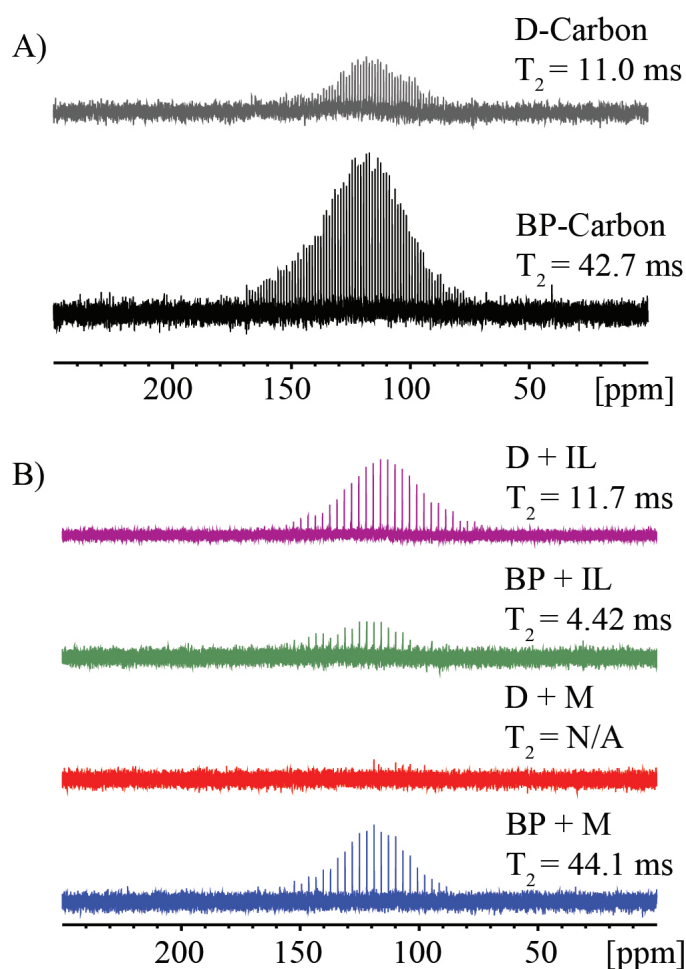


Figure 6.6: ^{13}C direct CPMG spectra for A) D- and BP-carbon black starting materials and B) N-doped derivatives. Spectra taken at 11.7 T, 15 kHz MAS rate.

Figure 6.6B shows ^{13}C CPMG spectra for BP+M, BP+IL, D+M, and D+IL. The same experimental parameters which produced the starting material spectra in **6A** provided no signal from the doped samples, again indicating a significant change

Table 6.1: Calculated T_2 relaxation rates for carbon black starting materials and doped samples.

Sample	T_2 (ms)	Standard Error (ms)
D-Carbon	11.0	1.15
BP-Carbon	42.7	11.7
D + IL	11.7	1.55
BP + IL	4.42	0.73
BP + M	44.1	45.6

to band gap and graphitic sheet structure upon N-doping. The reported spectra were obtained using a 200-pulse echo train at an echo time of 1.3 ms, for a total acquisition time of roughly 0.5 seconds. The T_2 s for the doped samples were 11.7 ms (D+IL), 4.42 ms (BP+IL), and 44.1 ms (BP+M). The low SNR in the spectrum for D+M precluded modelling of the FID and calculation of its T_2 under these experimental parameters. The fits for all samples where CPMG intensities were recordable are shown in **Appendix Figure 3**.

Nitrogen doping with IL has a markedly different effect on the T_2 values of D- and BP-carbon. D+IL has a nearly identical T_2 to D-carbon (11.7 and 11.0 ms, respectively). The fact that the same experimental parameters did not produce comparable signal between the D-carbon and D+IL CPMG experiments, while the calculated T_2 s of these materials are so similar, indicates that the D+IL signal was decaying much faster over the course of a single echo within the CPMG echo train, i.e. the T_2^* values of these materials must be significantly different, and thus signal losses are due to rapid T_2^* relaxation. Doping BP-carbon with IL causes a reduction in T_2 of roughly 60%. This significant change seems to indicate a major impact on the band gap structure of BP-carbon upon doping with IL, possibly indicating a higher degree of doping success and/or more defect sites compared to D+IL.

The effect of melamine doping on the relaxation properties of D- and BP-carbon are even more pronounced. Obviously, without an actual calculated T_2 for D+M it is difficult to conclude that the failure of the CPMG experiment under these conditions is due to D+M having a significantly different T_2 or T_2^* , or due to another experimental failure. Either of the first two cases would indicate changes to the band gap structure of D-carbon and potentially indicate doping success, as in the case of BP+IL. The T_2 of BP+M is similar to that of BP-carbon, but an important detail is that the goodness of fit of the curve which produced this value was less than that which produced the other reported T_2 values (see **Appendix Figure 3**). This may indicate the significant presence of more than one ^{13}C site represented by the broad BP+M signal. Multiple sites being represented by the same FID may not be in phase, and so the intensities recorded at each FID within the CPMG echo train, which were used to model the exponential decay curve that produced the reported T_2 s, may have been changed by the incoherent phases of multiple sites. If this is the root of the poorly modelled data, this could serve as evidence of new carbon sites introduced by the doping process with this particular combination of carbon black and doping agent. This would be a useful diagnostic tool, since different starting material / doping agent combinations do not seem to significantly effect the shape of the broad peak from sp^2 -hybridized carbon sites in terms of breadth or chemical shift. It is likely that the level of doping is low enough that, without selective isotopic labelling, it would be unlikely to notice any differences or newly introduced sites (e.g. those carbon sites bonded to nitrogen dopant centres).

6.4 Conclusions

Samples of nitrogen-doped carbon black were synthesized via pyrolysis of two carbon black precursors mixed with two nitrogen-containing small organic molecules, and the nature of the introduced dopant sites was investigated through ssNMR. Direct ^1H spectra of the parent carbon materials as well as the doped samples revealed a high frequency site which persisted after heating in vacuo, attributed to edge- or defect-based protons attached to sp^3 -hybridized tertiary or secondary carbons, separating it from sites at lower frequency which were attributed to atmospheric water or leftover solvents from the pyrolysis process, which were removed by the process. ^1H double quantum filtered spectra supported this assertion, indicating that the low frequency peaks represented dense collections of water in the starting materials which were largely removed by the high-temperature N-doping process. The high-frequency structural site is apparently sparsely populated and isolated from similar sites in the starting material; however this is not true of the structural sites in the doped samples, which may be clustered and near in space to one another based on the strength of their homonuclear dipolar coupling. 2D EXSY spectra did not show any chemical or magnetic exchange between sites at long mixing times and room temperature, in either the parent or doped samples, indicating that individual proton sites are well isolated from others. Differences in the ^{13}C T_2 relaxation properties between starting material carbons and doped samples seem to indicate particular doping success for the BP+IL, D+M, and BP+M sample. ^{13}C CPMG and T_2 measurements could be useful as a diagnostic tool to detect the presence of new carbon sites after doping, where, without ^{15}N labelling and at low dopant levels, direct evidence of new carbon sites would be difficult to produce.

6.5 Suggestions for Future Work

The work presented in this chapter clearly shows that there are interesting spectroscopic differences between N-doped carbon samples produced with different carbon and nitrogen sources. The differences are subtle, and the amount of dopant introduced is very low, but the ability to produce useful results from these uncooperative materials through ssNMR is clear. With expanded resources (e.g. larger sample volumes, or ^{15}N labelled samples), a number of further investigations would have likely led to an even clearer picture of the environment around the nitrogen sites in the N-doped samples, leading to an unambiguous rationalization of the platinum-stabilizing ability of these materials. The following sections will detail next steps which could achieve these goals.

6.5.1 Isotopic Labelling

The simplest way to improve the quality of the conclusions made by this study would be to produce isotopically labelled samples. The relatively simple and inexpensive practice of exchanging protons for deuterons is not expected to provide significant information: there are already very few protons in this material to speak of, and 2D EXSY studies suggest that the structural protons are not acidic, and therefore are unlikely to exchange with deuterons. Using labelled N-doping agents, however, would be a worthwhile course of action. A recent simulations-based paper by Wang et al. provides an idea of the expected ^{15}N chemical shifts in an N-doped graphitic material, and By using ^{15}N -labelled sources installed nitrogen dopant sites could be accurately assigned, and with the concurrent boost in signal intensity it may be possible to perform correlation studies between ^{15}N sites and nearby ^1H and ^{13}C spins, further describing these sites.⁴¹ This method was used successfully in **Chapter 5** of this thesis, where ^{15}N la-

bellung was used to identify the nature of multiple ^{15}N sites in nitrogen-doped graphene through chemical shift resolution, and ^1H - ^{15}N correlations were used to resolve nearly indistinguishable ^1H sites. These accomplishments would not have been possible without ^{15}N labelling. ^{13}C labelling of the carbon atoms within the N-dopants may also be a wise choice, potentially allowing for some resolution to arise from the broad ^{13}C signals shown in the spectra above.

6.5.2 Variable Temperature Studies

The most intuitive next step in these studies, absent the possibility of isotopic labelling, would be to repeat the double quantum filtered experiments (i.e. ^1H BaBa and EXSY) at additional temperatures. Since all the studies shown here were done at ambient conditions, there is likely a significant amount of important data to be retrieved through variable temperature spectroscopy. Recollecting spectra at lower temperature would likely allow for the detection of even weaker dipolar couplings between structural sites, potentially allowing for correlations between different structural sites, (e.g. between two proton sites across a 'defect' pore) to be resolved. Heightened temperatures, conversely, may increase local mobility enough to significantly lengthen T_2 relaxation times and sharpen the signals, resulting in increased resolution. Ideally this would allow resolution between the starting material edge-based proton sites and any new proton sites introduced by the doping process, since their signals are so convoluted in the ambient-temperature spectra above.

6.5.3 Alternative Nuclei, Experiments, Targets

In this study the spectroscopic analysis was limited to ^1H and ^{13}C experiments, but it is reasonable to assume that expanding to other nuclei may provide useful information.

As disadvantageous as it is, ^{14}N spectroscopy has been successfully applied in the past to identify the nature of nitrogen sites.^{43, 44} Considering the enormous breadth of most ^{14}N signals, this method of analysis would only work on feasible time scales if the SNR could be enhanced through cross-polarization from a nearby abundant spin system (e.g. protons from a pyridinium-like dopant site). It is also likely that natural abundance ^{14}N spectroscopy would only be elucidative if there are a small number of well defined sites, which may not be likely in the present samples. Another method of enhancing SNR would be to employ dynamic nuclear polarization (DNP). Hundreds- and thousands-fold signal enhancements are not uncommon with DNP, however the method requires the determination of a suitable polarizing agent, which has proven difficult for electronically conductive materials like carbon black, not to mention a significant investment in special instrumentation.⁴⁵⁻⁴⁷ The use of gaseous NMR probe molecules may also be an interesting avenue for this project. The structures of highly porous materials, such as zeolites and metal-organic frameworks (MOFs), are routinely investigated through the NMR spectroscopy of molecules physisorbed into their repeating pore and channel networks.⁴⁸⁻⁵⁰ Carbon Black does not show any significant 3D crystal symmetry, however it does possess extremely high surface area, and the N-dopant sites are thought to create defect pores and catalytic centres, which would conceivably change the NMR properties of a suitable probe molecule.

6.6 Appendix

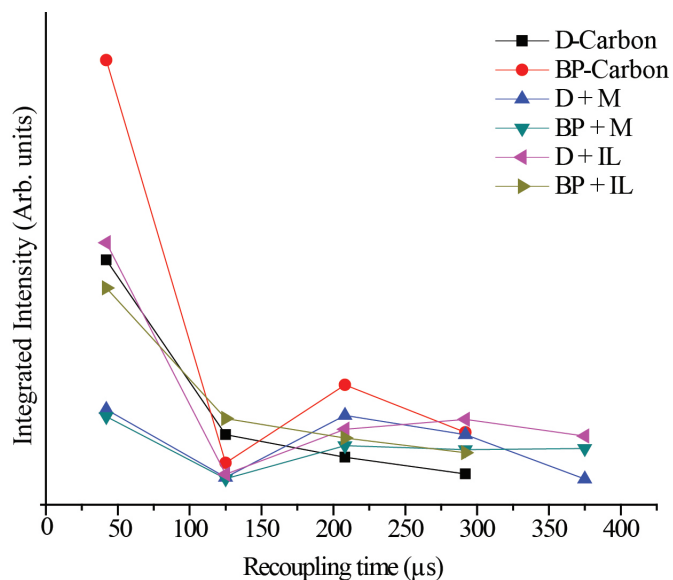


Figure 6.1: A plot of the integrated intensities of peaks in the BaBa experiments from Figure 4.

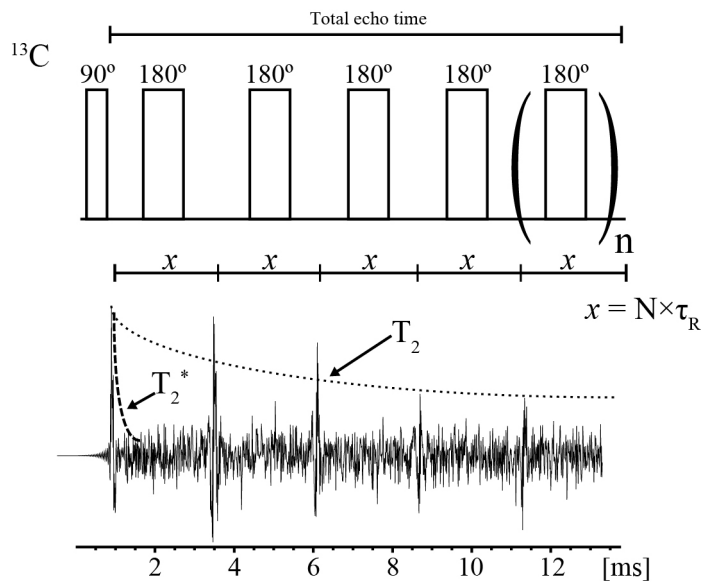


Figure 6.2: A schematic of the CPMG pulse sequence along with sample FID, with relevant timings and extractable relaxation measurables highlighted.

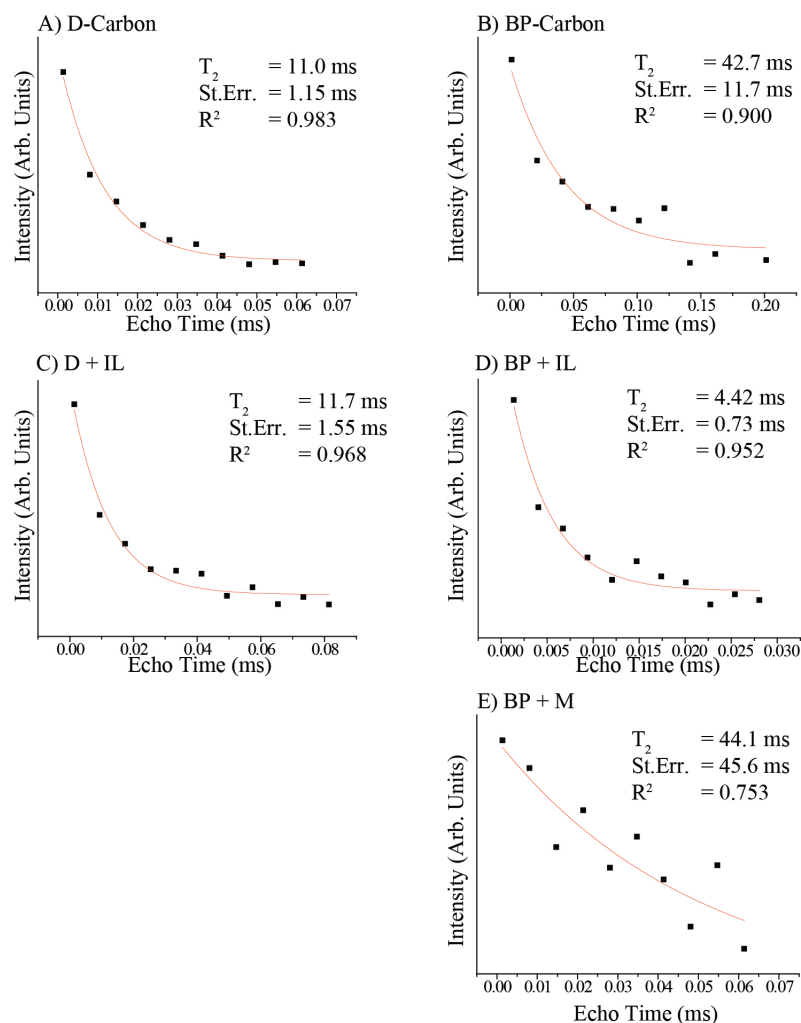


Figure 6.3: Fits of T_2 measurement data for A) D-Carbon, B) BP-Carbon, C) D + IL, D) BP + IL, and E) BP + M samples, with noted standard errors and R^2 values. Note the especially poor fit seen in plot E.

References

- [1] Carrette, L.; Friedrich, K. A.; Stimming, U. *ChemPhysChem* **2000**, (1), 162–193.
- [2] Carrette, L.; Friedrich, K.; Stimming, U. *Fuel Cells* **2001**, 1(1), 5–39.
- [3] Dyer, C. K. *J. Power Sources* **2002**, 106(1), 31–34.
- [4] Hoogers, G. *Fuel Cell Technology Handbook*; CRC Press, **2014**.
- [5] Larminie, J.; Dicks, A.; McDonald, M. *Fuel Cell Systems Explained*; John Wiley & Sons, **2008**.
- [6] Eikerling, M. *J. Electrochem. Soc.* **2006**, 153(3), E58–E70.
- [7] Holdcroft, S. *Chem. Mater.* **2013**, 26(1), 381–393.

- [8] Wu, J.; Yuan, X. Z.; Martin, J. J.; Wang, H.; Zhang, J.; Shen, J.; Wu, S.; Merida, W. *Journal of Power Sources* **2008**, *184*(1), 104 – 119.
- [9] Marr, C.; Li, X. *J. Power Sourc.* **1999**, *77*(1), 17–27.
- [10] Zhang, J. *PEM Fuel Cell Electrocatalysts and Catalyst Layers: Fundamentals and Applications*; Springer Science & Business Media, 2008.
- [11] Wilson, M. S.; Gottesfeld, S. *J. Appl. Electrochem.* **1992**, *22*(1), 1–7.
- [12] Switzer, E. E.; Olson, T. S.; Datye, A. K.; Atanassov, P.; Hibbs, M. R.; Fujimoto, C.; Cornelius, C. J. *Electrochim. Acta* **2010**, *55*(9), 3404–3408.
- [13] Jordan, L.; Shukla, A.; Behrsing, T.; Avery, N.; Muddle, B.; Forsyth, M. *J. Power Sourc.* **2000**, *86*(1), 250–254.
- [14] Kim, J.-H.; Ha, H. Y.; Oh, I.-H.; Hong, S.-A.; Lee, H.-I. *J. Power Sourc.* **2004**, *135*(1), 29–35.
- [15] Haug, A. T.; White, R. E.; Weidner, J. W.; Huang, W.; Shi, S.; Stoner, T.; Rana, N. *J. Electrochem. Soc.* **2002**, *149*(3), A280–A287.
- [16] Lee, M.; Uchida, M.; Yano, H.; Tryk, D. A.; Uchida, H.; Watanabe, M. *Electrochimica Acta* **2010**, *55*(28), 8504–8512.
- [17] Song, S.; Zhou, W.; Zhou, Z.; Jiang, L.; Sun, G.; Xin, Q.; Leontidis, V.; Kontou, S.; Tsiakaras, P. *Int. J. Hydrogen Ener.* **2005**, *30*(9), 995–1001.
- [18] Colón-Mercado, H. R.; Popov, B. N. *J. Power Sourc.* **2006**, *155*(2), 253–263.
- [19] Subbaraman, R.; Strmcnik, D.; Stamenkovic, V.; Markovic, N. M. *J. Phys. Chem. C* **2010**, *114*(18), 8414–8422.
- [20] Gottesfeld, S.; Pafford, J. *J. Electrochem. Soc.* **1988**, *135*(10), 2651–2652.
- [21] Wagner, N.; Gülzow, E. *J. Power Sourc.* **2004**, *127*(1), 341–347.
- [22] Oetjen, H.-F.; Schmidt, V.; Stimming, U.; Trila, F. *J. Electrochem. Soc.* **1996**, *143*(12), 3838–3842.
- [23] Baschuk, J.; Li, X. *Int. J. Ener. Res.* **2003**, *27*(12), 1095–1116.
- [24] Bi, W.; Fuller, T. F. *J. Power Sourc.* **2008**, *178*(1), 188–196.
- [25] Shao, Y.; Yin, G.; Gao, Y. *J. Power Sourc.* **2007**, *171*(2), 558–566.
- [26] Bi, W.; Gray, G. E.; Fuller, T. F. *Electrochem. Sol. State Lett.* **2007**, *10*(5), B101–B104.
- [27] Huang, S.-Y.; Ganesan, P.; Park, S.; Popov, B. N. *J. Am. Chem. Soc.* **2009**, *131*(39), 13898–13899.
- [28] Zhou, Y.; Pasquarelli, R.; Holme, T.; Berry, J.; Ginley, D.; O’Hayre, R. *J. Mater. Chem.* **2009**, *19*(42), 7830–7838.

- [29] Saha, M. S.; Li, R.; Sun, X.; Ye, S. *Electrochem. Comm.* **2009**, *11*(2), 438–441.
- [30] Higgins, D. C.; Meza, D.; Chen, Z. *J. Phys. Chem. C* **2010**, *114*(50), 21982–21988.
- [31] Morozan, A.; Joussetme, B.; Palacin, S. *Ener. Environ. Sci.* **2011**, *4*(4), 1238–1254.
- [32] Wang, H.; Maiyalagan, T.; Wang, X. *ACS Catal.* **2012**, *2*(5), 781–794.
- [33] Zhu, J.; He, G.; Liang, L.; Wan, Q.; Shen, P. K. *Electrochim. Acta* **2015**, *158*, 374–382.
- [34] Huang, H.; Ye, G.; Yang, S.; Fei, H.; Tiwary, C. S.; Gong, Y.; Vajtai, R.; Tour, J. M.; Wang, X.; Ajayan, P. M. *J. Mater. Chem. A* **2015**, *3*(39), 19696–19701.
- [35] Cai, W.; Piner, R. D.; Stadermann, F. J.; Park, S.; Shaibat, M. A.; Ishii, Y.; Yang, D.; Velamakanni, A.; An, S. J.; Stoller, M. *Science* **2008**, *321*(5897), 1815–1817.
- [36] MacIntosh, A. R.; Harris, K. J.; Goward, G. R. *Chem. Mater.* **2015**, *28*(1), 360–367.
- [37] Matthews, P. D.; King, T. C.; Glass, H.; Magusin, P. C.; Tustin, G. J.; Brown, P. A.; Cormack, J. A.; García-Rodríguez, R.; Leskes, M.; Dutton, S. E.; others. *RSC Adv.* **2016**, *6*(67), 62140–62145.
- [38] Harris, R.; Thompson, T.; Forshaw, P.; Foley, N.; Thomas, K.; Norman, P.; Pottage, C. *Carbon* **1996**, *34*(10), 1275–1279.
- [39] Harris, R. K.; Thompson, T. V.; Norman, P. R.; Pottage, C. *J. Chem. Soc., Faraday Trans.* **1996**, *92*(14), 2615–2618.
- [40] Harris, R. K.; Thompson, T. V.; Norman, P. R.; Pottage, C.; Trethewey, A. N. *J. Chem. Soc., Faraday Trans.* **1995**, *91*(12), 1795–1799.
- [41] Wang, X.; Hou, Z.; Ikeda, T.; Terakura, K. *J. Phys. Chem. C* **2014**, *118*(25), 13929–13935.
- [42] Ramsey, N. F. *Phys. Rev.* **1950**, *78*(6), 699.
- [43] Stark, R.; Haberkorn, R.; Griffin, R. *J. Chem. Phys.* **1978**, *68*(4), 1996–1997.
- [44] Jeschke, G.; Jansen, M. *Angew. Chem. Int. Ed.* **1998**, *37*(9), 1282–1283.
- [45] Matsuki, Y.; Takahashi, H.; Ueda, K.; Idehara, T.; Ogawa, I.; Toda, M.; Akutsu, H.; Fujiwara, T. *Phys. Chem. Chem. Phys.* **2010**, *12*(22), 5799–5803.
- [46] Rossini, A. J.; Zagdoun, A.; Lelli, M.; Canivet, J.; Aguado, S.; Ouari, O.; Tordo, P.; Rosay, M.; Maas, W. E.; Copéret, C. *Angew. Chem.* **2012**, *124*(1), 127–131.
- [47] Lesage, A.; Lelli, M.; Gajan, D.; Caporini, M. A.; Vitzthum, V.; Miéville, P.; Alauzun, J.; Roussey, A.; Thieuleux, C.; Mehdi, A.; others. *J. Am. Chem. Soc.* **2010**, *132*(44), 15459–15461.
- [48] Sánchez-Sánchez, M.; Blasco, T. *Chem. Comm.* **2000**, (6), 491–492.
- [49] Xu, J.; Terskikh, V. V.; Huang, Y. *J. Phys. Chem. Lett.* **2012**, *4*(1), 7–11.
- [50] Babonneau, F.; Yeung, L.; Steunou, N.; Gervais, C.; Ramila, A.; Vallet-Regi, M. *J. Sol-Gel Sci. Technol.* **2004**, *31*(1), 219–223.

7 — Conclusion

The results of the work completed in this thesis are described in this chapter. It will begin with a summary of each of the main body chapters of the thesis. An analysis of the main impact of the thesis and suggestions for future work are then offered.

7.1 Summary

The focus of this thesis was to apply solid-state nuclear magnetic resonance (ssNMR) techniques to the study of graphene-based materials. As is mentioned in a number of preceding chapters, specifically **Chapter 2**, these materials present several challenges for unambiguous analysis through ssNMR. First, they are often electronically conductive, especially when they are not heteroatomically doped or covalently modified with functional groups, i.e. when the sp^2 hybridized network of carbon atoms is intact. Within a strong magnetic field this results in significant induced local currents, which then produce opposing local magnetic fields, making a number of requirements for spectral acquisition (tuning, matching, sample spinning, etc.) more difficult or impossible. Delocalized and / or unpaired electrons, such as those present in paramagnetic impurities from the synthesis process of some of these samples, can also alter nuclear relaxation parameters, causing severe signal broadening and chemical shift variability. Further increasing signal broadness is the fact that these materials are non-stoichiometric, and each chemically identical carbon nucleus in a graphene sheet, for example, is not in a magnetically

identical environment due to slight changes in bond angles, internuclear distances, etc. Nevertheless, considering the wealth of knowledge available through ssNMR analysis, the following attempts were made to overcome these challenges.

Chapter 3 describes the synthesis and analysis of a number of covalently modified graphitic samples through ^1H and ^{13}C ssNMR. The samples were produced via a condensation reaction between the hydroxide groups in graphene oxide (GO) and either sultone rings or methoxy groups, forming a small library of sulfonic acid-functionalized graphene samples. ^1H - ^{13}C cross-polarized ssNMR experiments were used to verify the presence of hydroxide and epoxide groups in the parent GO material, and to resolve signals from the alkyl chain carbon atoms in the acidic groups at remarkably high resolution. It was noted that functionalization progress could be monitored through ssNMR, and that the presence of newly installed acidic groups could cause the reduction of remaining oxygen-based functional groups in GO. The level of functionalization was measured through elemental analyses, suggesting that there was one acidic group for every 13 x 13 carbon atom square in the graphene sheet. Curiously, it was noted that the functionalized graphenes did not readily exchange their acidic protons with protons or deuterons in solution, even at increased temperatures or under acidic conditions. This led to the suggestion that the functionalized graphenes were bound together tightly in sheet stacks, which was supported by a collapse of interlayer spacing upon functionalization shown through powder X-ray diffraction. It had been noted that functionalized graphenes were protonically conductive, and that their addition in small quantities to ionomeric proton conductive materials improved their proton conductivity: an important parameter for the performance of proton exchange membrane fuel cells. The results of this project suggest that only the functional groups at the periphery of sheet stacks interact with acidic

proton and ionomer host moieties, and that increasing surface area through improved delamination or reduced sheet size, would be advantageous.

Chapter 4 details a ssNMR study of samples of graphene and carbon nanotubes which have been doped with phosphorus and nitrogen. The samples under investigation were nitrogen-doped graphene (NG), phosphorus-doped graphene (PG), and nitrogen and phosphorus co-doped carbon nanotubes (PNCNTs). The samples were synthesized using a variety of deposition and solvothermal methods and contained dopant levels lower than 5 at% in total. This low doping level, coupled with the difficulties of applying ssNMR to conductive and amorphous samples, meant that spectral acquisition and interpretation was even less trivial than usual. The phosphorus sites in PG and PNCNTs were found to be quite similar to one another; both samples produced a ^{31}P spectrum mainly featuring a single broad peak centred at roughly 200 ppm with extremely short (ms) relaxation times. This combination of fast relaxation and high chemical shift is highly unusual, and was used to identify the phosphorus site as being within a magnetically turbulent environment, such as the graphitic sheet or CNT walls. These results were used to resolve the considerable ambiguity found in the results of a P 2p-edge X-ray photoelectron spectroscopy study, and are also supported by previous ^{31}P ssNMR results. The results of work by Leskes et al. showed that, while the level of phosphorus doping achieved in their samples was significantly higher (ca. 20 at%), most of that phosphorus was in the form of elemental phosphorus and phosphate oligomers: by-products of the doping process. ssNMR was used to prove that the synthesis methods employed here produce much purer samples of P-doped graphene and CNTs with homogeneous dopant sites. The nitrogen centres in PNCNTs were not probed directly since they were formed using naturally abundant precursor materials, considering the low chance of success for a meaningful ^{14}N ssNMR analysis. The NG sample, however,

was synthesized using ^{15}N labelled aniline, and so ^{15}N ssNMR was applied to identify the nature of the nitrogen dopant sites in NG. Two distinct populations of nitrogen dopant sites were revealed in significant proportions by direct ^{15}N spectroscopy; one pyridinic and one graphitic. Through the use of ^1H - ^{15}N correlation spectroscopy, resolution was achieved between two nearly identical nitrogen dopant sites. A slight change in chemical shift was used to separate edge based dopant sites which were either near in space to or isolated from edge based protons. This study successfully used relatively simple pulse sequences and isotopic labelling to verify and clarify XPS results, confirmed a synthesis route to pure heterodoped carbons, and displayed the remarkable chemical resolution possible through ssNMR. It is hoped that these results will encourage materials scientists to explore ssNMR as a more commonplace method of analysis in the future.

Chapter 5 presents a study of the effect of ambient temperature and humidity conditions on the electrochemical performance and ^1H ssNMR spectroscopy of SPEEK membranes, compared to membranes which have been doped with small amounts of graphitic additives. Membranes consisting of an 80% sulfonated PEEK matrix with between 0.1 and 5 wt% GO or propylsulfonic GO (PGO) were cast and treated at environmental conditions ranging from 50 - 90 °C and 50 - 100 %RH during measurement of their proton conductivity through electrochemical impedance spectroscopy (EIS) using a 4-electrode test cell. These conditions were also used to equilibrate the samples in-rotor to measure their variable temperature (VT) ^1H ssNMR spectroscopy in an effort to match changes in proton conductivity or operational range with NMR measurables. When fully saturated with water, composite membranes displayed significantly higher proton conductivity than pure SPEEK membranes at certain dopant loadings, but it was noted that higher dopant concentrations caused reduced conductivities, likely due to interference with the formation of hydrophilic channels in the polymer matrix. Proton

conductivity measurements taken at 90 %RH show that the addition of dopant materials may have a moderately negative effect on overall proton conductivity, while broadening the effective range (with respect to temperature and humidity) over which proton conductivity can be recorded. This is likely due to an increased ability of composite membranes to retain water as a result of increased hydrogen bonding between liquid-like water, surface acid / hydroxide groups in the dopant, and acidic groups in the polymer matrix. It was found that, especially for highly hydrated samples, MAS coupled with high temperatures caused significant water losses over the course of the variable temperature analyses. Water losses such as those observed here would undoubtedly have some effect on the proton dynamics which were the aim of this study, and so lower temperatures and MAS rates are recommended for further studies. Low-humidity ^1H NMR of composite membranes shows less severe water loss as a result of high temperature MAS, but indicates that dopants with acidic groups are more able to retain water for their parent ionomer matrices than those without, perhaps indicating that a stronger hydrogen bonding network is present in acidic dopant samples.

Chapter 6 reports the as-yet unpublished results of a ssNMR natural abundance analysis of various samples of nitrogen doped carbon black. The samples were synthesized by pyrolyzing mixtures of commercial carbon black (two forms: Black Pearls and Denka Black) with nitrogen-rich precursors (melamine or ethylmethyylimidazolium dicyanamide, an ionic liquid), for a total of four unique nitrogen-doped carbon blacks. Without ^{15}N , the NMR analysis was based on homonuclear ^1H correlations mediated by the dipolar coupling interaction, and ^{13}C CPMG spectra which are highly sensitive to electrical conductivity and defect presence via T_2 and T_2^* relaxation times. Double quantum filtered ^1H Back-to-Back spectroscopy revealed that the few structural protons found in carbon black starting materials were well isolated from one another, likely lo-

cated on the edges of graphitic sheets or at defect sites. By comparison, Back-to-Back spectra of doped samples showed much stronger dipolar coupling between structural protons, indicating that the the doping process had introduced a significant number of clustered protons. This may be due to the introduction of defect sites decorated with structural protons, perhaps even bonded to dopant nitrogen atoms, or to the breaking of graphitic sheets into smaller pieces, resulting in more edge-based protons. Direct ^{13}C spectra were also collected. The CPMG pulse sequence was used in an effort to increase the signal to noise ratio of the spectra in order to collect them in a reasonable amount of time. The position and shape of these spectra were essentially uniform across all samples, doped or not, however the same experimental parameters did not produce a similar amount of signal from each sample. The optimal parameters for the undoped samples, for instance, seemed to indicate that the T_2 and T_2^* relaxation processes in these materials were extremely slow: signal magnetization was observable in these experiments for entire seconds after perturbation. This may indicate that the carbon precursors used here were highly pure and relatively free of defects, which was particularly true in the case of Black Pearls. The signals of the doped samples relaxed much more quickly, providing further evidence of the introduction of defect sites, potentially caused by the introduction of dopant nitrogen atoms. While a remarkable amount of information can be obtained through ^1H and ^{13}C , the conclusions drawn here are somewhat ambiguous. Ideally, these results would serve as verification and supplementary evidence for ^{15}N studies of isotopically labelled samples, coupled with XPS and imaging studies.

7.2 Outlook & Future Work

The chief lesson of this work is that, despite the challenges, significant information about graphene, CNTs, and other conductive carbon based materials can be obtained through ssNMR, and that these studies can be industrially relevant. The focus of this thesis has been on ionomer and catalyst layers in hydrogen fuel cells, however these materials are featured in a broad array of applications; other energy storage devices like supercapacitors and batteries, analytical sensors, surface chemistry, electronics and many, many others. Suggestions for future work expanding upon the results detailed in this thesis follow.

7.2.1 A Library of Functionalized Graphenes

At the outset of the functionalized graphene portion of this thesis the potential library of samples was limited. The most successful methodology for acid group attachment involved the ring opening of 5, or 6-membered sultone rings, and so acid group linkers were limited to short alkyl chains.¹ Some success was had using a trimethoxy silane linker as well, but the precise nature of the bond between graphene sheet and acid group was ambiguous.² As a result, the effect of the nature of the acid linker group (e.g. steric properties, rigidity, etc.) could not be properly explored.

A new method of functionalization based on the *in-situ* formation of a diazonium salt has recently shown significant promise.³ Further testing with respect to functionalization level and sheet attachment are necessary, but if this method proves to be as robust as sultone ring opening, the door opens to a much more diverse set of acid group linkers. The diazonium method requires only that a potential linker group has a primary amine group, and so an enormous library of functionalized graphene samples is easily imagined.

Bifunctional linker groups would be an excellent starting point for a new project along this research path. A linker with the dual properties of acidity and high steric hinderance (for improved sheet delamination) could be used to explore the effect of sheet stacking on ssNMR and electrochemical properties of functionalized graphenes and composite ionomer membranes. Rigid linker groups with multiple primary amine anchor points could bridge two graphitic sheets together. This expanded graphene could find use as an electrode material for lithium or sodium ion batteries.^{4, 5} Investigation of the surface chemistry of graphene oxide in this manner could lead to remarkable progress in materials chemistry and energy storage, and so it would be wise to explore this area further.

7.2.2 ssNMR and 2D Materials

The results in this thesis prove that ssNMR is a useful and underutilized tool for the analysis of heterogeneous and noncrystalline materials. As a result, it would be advantageous to apply the methods shown here to the ssNMR study of the wide array of traditionally unfavourable samples. Especially in the case where dopant nuclei are NMR-receptive or where isotopic labelling is possible, an enormous amount of structural information regarding heteroatomically doped graphene, CNTs, core-shell particles, lamellar materials, and other examples may become accessible. Considering the importance of these materials to electronics, catalysis, energy storage, and numerous other fields, a broadened understanding of their structure will certainly lead to an improved ability to fine-tune and apply these materials to greater applications.

An obvious course of action after the results reported in **Chapter 4** would be to produce a sample of PNCNTs with ^{15}N labelled nitrogen dopants. Using ^{15}N labelled imidazole as a nitrogen source would produce a sample where ^{31}P - ^{15}N correlation exper-

iments are possible on a reasonable time scale. A clearer picture of the nature of dopant sites within PNCNTs, theorized to be clusters of nitrogen atoms surrounding a phosphorus atom to relieve bond angle strain, could conceivably be drawn from these results. Boron nitride and carbon nitride materials are also prime targets for ssNMR analysis where isotopic labelling is feasible, and would potentially be simpler targets than the doped samples studied here considering the repeating nature of their 2D structure.^{6, 7}

7.2.3 Proton Dynamics in Ionomer Membranes

¹H ssNMR done at operational conditions has continued to prove itself as an important methodology for the study of the performance of ionomer membranes on a molecular level. In this thesis, as well as in previous work from the Goward group, it has been shown that ¹H spectroscopy can be used to describe and rationalize proton conductivity in PEMs. The results shown in **Chapter 5** can easily be expanded upon by exploring different ionomer - dopant combinations. SPEEK was used as the base ionomer for the studies in this thesis due to its availability and the ease with which the level of sulfonation, and therefore acidity, can be controlled. SPEEK is, however, not the highest performing or most thermally stable of the common PEM ionomers. It would be a natural next step to expand the ¹H ssNMR and electrochemical impedance spectroscopy study to new materials; SPEEK membranes of different degrees of sulfonation as well as other successful ionomers (NafionTM, sulfonated polysulfones, polyphenylenes, and polyimides, etc.), in addition to dopants from an expanded library of functionalized graphenes.

One of the greatest challenges faced during the proton dynamics portion of this thesis was the positive assignment of proton signals. This comes from the fact that SPEEK has a large number of structural protons which dominate most spectra, meaning the more

interesting acidic protons (which can shift and change shape as a response to relative humidity and temperature) are difficult to model. The simplest (if not the least expensive) way to alleviate this challenge would be to employ selective deuteration in order to make signal identification less complicated. By selectively deuterating the acidic protons in the ionomer matrices, for example, it is possible that acidic exchange with protons in solution or mobility within the ionomer layer could be easier to characterize through ^2H NMR. Conversely, using a perdeuterated ionomer and exchanging its acidic deuterons for protons, the quality and clarity of ^1H spectra could be materially improved.

Finally, progress has been made recently toward the development of specialized NMR hardware which can perform *in-situ* experiments on membrane materials.^{8, 9} The current iteration of this technology has the transmitter coil embedded within the membrane itself so as to avoid debilitating background signals and RF penetration issues. These extremely complicated probes have been used to image the water within an ionomer membrane as it conducts ions, as it would while in operation within a fuel cell. This concept is still new, but progress towards its improvement would almost certainly lead to important breakthroughs in fuel cell characterization on a short time frame.

References

- [1] Wang, Y.; Yang, D.; Zheng, X.; Jiang, Z.; Li, J. *J. Power Sourc.* **2008**, *183*(2), 454–463.
- [2] MacIntosh, A. R.; Harris, K. J.; Goward, G. R. *Chem. Mater.* **2015**, *28*(1), 360–367.
- [3] Lomeda, J. R.; Doyle, C. D.; Kosynkin, D. V.; Hwang, W.-F.; Tour, J. M. *J. Am. Chem. Soc.* **2008**, *130*(48), 16201–16206.
- [4] Sun, J.; Lee, H.-W.; Pasta, M.; Yuan, H.; Zheng, G.; Sun, Y.; Li, Y.; Cui, Y. *Nature Nanotech.* **2015**, *10*(11), 980–985.
- [5] Wen, Y.; He, K.; Zhu, Y.; Han, F.; Xu, Y.; Matsuda, I.; Ishii, Y.; Cumings, J.; Wang, C. *Nature Comm.* **2014**, *5*, 4033.
- [6] Hu, Y.; Shim, Y.; Oh, J.; Park, S.; Park, S.; Ishii, Y. *Chem. Mater.* **2017**, *12*(29), 5080–5089.
- [7] Gervais, C.; Babonneau, F. *J. Organomet. Chem.* **2002**, *657*(1), 75–82.
- [8] Ogawa, K.; Haishi, T.; Aoki, M.; Hasegawa, H.; Morisaka, S.; Hashimoto, S. *Rev. Sci. Inst.* **2017**, *88*(1), 014701.
- [9] Ogawa, K.; Yokouchi, Y.; Haishi, T.; Ito, K. *J. Magn. Res.* **2013**, *234*, 147–153.